eman ta zabal zazu

Universidad del País Vasco

Euskal Herriko Unibertsitatea

DOCTORAL THESIS

# Suitability of magnetotactic bacteria as biomedical agents

Lucía Gandarias Albaina

Supervisors:
Prof. Alicia Muela Blázquez
Dr. Ana García Prieto

2022

# Acknowledgments

Me gustaría empezar este documento agradeciendo a todas las personas que con su amistad, su compañía o su ayuda profesional me han ayudado durante el proceso de la tesis doctoral. No me es posible nombrar a todas las que me han acompañado en el camino pero me gustaría destacar a las que han sido imprescindibles en él.

Gracias a mis directoras de tesis Alicia Muela Blázquez y Ana García-Prieto por su ayuda y su generosidad. Gracias Alicia por animarme a volver al grupo y acogerme, por compartir tu sabiduría y tu experiencia conmigo, por tus consejos, por siempre estar dispuesta para resolver mis dudas y por mantenerme con los pies en la tierra. Ha sido una suerte haber llegado a tiempo para poder trabajar contigo.

Gracias Ana por tu paciencia y por descolgar el teléfono incluso antes del tono para ayudarme y resolver mis dudas. Por tu empeño en intentar siempre entender cada pequeño detalle de cada experimento. Gracias por introducirme en el mundo del sincrotrón y explicarme lo que estábamos haciendo de forma tan clara y detallada.

Gracias a Malú Fernández-Gubieda por tu calidad científica y humana. Por preocuparte siempre del bienestar de los integrantes del grupo de investigación y por haberme dado la gran oportunidad de formar parte de él.

Gracias al Grupo de Magnetismo y Materiales Magnéticos por acogerme y darme la oportunidad de trabajar con gente de distintas especialidades. Ha sido una experiencia muy enriquecedora. En especial gracias a David Gandia por haber compartido esta experiencia conmigo. Gracias también a nuestros queridos vecinos de la Universidad de Cantabria Luis Fernández Barquín y Javi Alonso por dejarme usar vuestro SQUID en momentos de máxima necesidad y acogerme siempre tan bien.

Je voudrais aussi remercier tous les MEMbers pour avoir fait de mon stage de trois mois dans votre laboratoire une expérience aussi agréable. En particulier je voudrais remercier Sandra Prévéral and Damien Faivre pour me donner l'opportunité de visiter votre laboratoire et de travailler avec vous. Ça a été vraiment une aventure impeccable !

Me gustaría continuar agradeciendo a mis compañeros de laboratorio y del Departamento de Microbiología por el compañerismo, la ayuda prestada y el buen ambiente. En especial me gustaría agradecer a David Muñoz por enseñarme a trabajar en el laboratorio y ayudarme a empezar con mis experimentos. A Sergio por haber hecho este proceso mucho más fácil y por estar siempre dispuesto a ayudar. A Kaan por devolver la alegría y el buen humor al laboratorio. Gracias a Alicia, Arkaitz, Ander, Eli, Leire A., Leire M., Xabi, Uxue, Idoia, Maialen, Aitziber, Zuriñe y a todos los que habéis estado por allí todo este tiempo. Gracias también a Óscar del Departamento de Electricidad y Electrónica por tu ayuda y por amenizar los descansos del café.

Gracias a mis queridas Magterbias las doctoras Lourdes Marcano Prieto y Elizabeth M. Jefremovas. Más allá del aporte científico que habéis dado a mi tesis, Lur, gracias por tus consejos y tu ayuda como hermana mayor científica; Eli, gracias por tu optimismo y tu bendita intensidad. Ha sido un placer trabajar con vosotras y espero que sigamos haciéndolo por muchos años.

Me gustaría agradecer también al Ministerio de Ciencia e Innovación por financiar este proyecto del que he tenido el placer de formar parte. También a la Universidad del País Vasco (UPV/EHU) por dejarme un espacio donde llevar a cabo mis experimentos.

Gracias a los Servicios Generales de Investigación (SGIker) por vuestra profesionalidad y accesibilidad. En especial me gustaría agradecer a Alejandro Diez y Ricardo Andrade por ayudarme a ilustrar mi tesis con bonitas imágenes y a Iñaki Orue por ayudarme a hacer medidas magnéticas de muestras con tan poca señal. Gracias también a Juan Carlos Raposo y a Patricia Navarro.

Thank you to the beamline scientists of BL22 - CLÆSS beamline in ALBA synchrotron, of XAFS beamline in Elettra synchrotron and of BM23 beamline in ESRF synchrotron for allowing me to work with you and for your help during the experiments.

Gracias a mis padres, mi hermana y mis abuelos por el cariño, la paciencia y el apoyo incondicional. Gracias por recordarme de vez en cuando qué es lo realmente importante.

Gracias a mis amigas de siempre Amaia y Paula por hacer que la distancia no sea un problema y mantener nuestra relación impasible al paso de los años. Gracias Belén por tu compañía en los momentos difíciles.

Finally, I would like to give a special mention to my "colocs" in the process of writing this thesis: Dr. Dan Chevrier and Mr. Saul Gato for your patience, your kindness, and your valuable advice. Thank you for welcoming me into your house and for giving me a place to write my thesis, for revising the manuscript, and for always being ready to discuss science or to teach me how to play guitar.

# Contents

# Resumen

Las bacterias magnetotácticas son microorganismos acuáticos capaces de sintetizar una o varias cadenas de orgánulos magnéticos intracelulares denominados magnetosomas. Debido a su disposición en cadenas dispuestas a lo largo del eje longitudinal de las bacterias, los magnetosomas funcionan como una brújula permitiendo a estos microorganismos alinearse con el campo magnético terrestre. La justificación más aceptada para explicar el comportamiento magnético de las bacterias magnetotácticas es la denominada "hipótesis magnetoaerotáctica". Según esta hipótesis, las bacterias magnetotácticas sintetizan magnetosomas para buscar de manera más eficaz la zona de la columna de agua donde las condiciones son más adecuadas para su proliferación. Así, su alineamiento con el campo magnético terrestre fijaría las bacterias en una dirección, reduciendo su movimiento de tres dimensiones a dos.

Las bacterias magnetotácticas fueron observadas por primera vez en los años 60 por Salvatore Bellini, quien observó un gran número de bacterias nadando en dirección norte y especuló que ello era debido a que en su interior contenían una "brújula magnética". Esta hipótesis fue confirmada posteriormente por Richard P. Blakemore que de manera independiente redescubrió las bacterias magnetotácticas en 1974 y fue el primero en observar los magnetosomas en el interior de estos microorganismos.

Desde que se descubrieron, tanto las bacterias magnetotácticas como los magnetosomas han suscitado creciente interés en la comunidad científica. Los magnetosomas se componen de un núcleo mineral magnético de alta pureza química compuesto de magnetita ($Fe_3O_4$) o greigita ($Fe_3S_4$), envuelto por una membrana proteolipídica. La composición, la forma y el tamaño de los magnetosomas están sujetos a un control genético y, por lo tanto, dependen de cada especie bacteriana. A pesar de la variedad de formas, el núcleo cristalino

de los magnetosomas se ajusta principalmente a cuatro patrones morfológicos diferentes: cuboctaédrico, prismático, en forma de bala y en forma de diente. Asimismo, su tamaño oscila entre los 35 y los 120 nm, rango dentro del cual cada magnetosoma conforma un monodominio magnético estable a temperatura ambiente. Dentro de cada especie bacteriana los magnetosomas presentan una morfología uniforme y su distribución de tamaños es estrecha, debido al estricto control genético del proceso de biomineralización. Por lo tanto, se trata de nanopartículas altamente reproducibles. Además, la membrana proteolipídica que envuelve al núcleo mineral confiere biocompatibilidad y estabilidad coloidal a los magnetosomas.

Por todo ello, los magnetosomas son candidatos ideales para una serie de aplicaciones biomédicas relacionadas con el tratamiento y el diagnóstico del cáncer. Por ejemplo, gracias a sus propiedades magnéticas los magnetosomas presentan una gran capacidad de producir calor bajo la aplicación de un campo magnético alterno, por lo que pueden utilizarse como agentes en tratamientos de hipertermia magnética. Por otro lado, su membrana de composición proteolipídica constituye una matriz para la funcionalización de los magnetosomas con diversas biomoléculas. Así, éstos pueden utilizarse como vehículos para transportar medicamentos hacia zonas de interés hasta las que son guiados con campos magnéticos externos. Además, pueden utilizarse en técnicas de diagnóstico como agentes de contraste en imagen de resonancia magnética.

Sin embargo, existen varias limitaciones asociadas al uso de los magnetosomas en biomedicina. La principal desventaja es la dificultad y el bajo rendimiento del procedimiento necesario para extraer y purificar los magnetosomas. Además, al igual que otras nanopartículas magnéticas, los magnetosomas presentan una limitada penetración a través de las barreras biológicas y su distribución en el tejido tumoral es desigual.

Con el fin de sobrepasar estas limitaciones, se ha propuesto el uso de las bacterias magnetotácticas como agentes biomédicos. Las bacterias magnetotácticas reúnen las ventajas intrínsecas de los magnetosomas más la capacidad de movimiento y quimiotaxia y la posibilidad de ser genéticamente modificadas. Además, las bacterias magnetotácticas tienen preferencia por los entornos microaerófilos o anaerobios, como las zonas tumorales, con lo que, en principio, podrían penetrar los tumores de manera más efectiva que los magnetosomas aislados.

En este contexto, esta tesis pretende abordar distintos aspectos del uso de las bacterias magnetotácticas como agentes biomédicos. La tesis está organizada en cinco capítulos precedidos de una breve introducción.

En el *Capítulo 1* se analiza la interacción de las bacterias magnetotácticas y los magnetosomas con células cancerosas. En la primera parte de este capítulo se verifica mediante técnicas de magnetometría y de microscopía que tanto las bacterias magnetotácticas como los magnetosomas son capaces de ser internalizados por las células cancerosas, un hecho que es fundamental para la mayor parte de aplicaciones biomédicas propuestas hasta el momento. En la segunda parte del capítulo se pretende profundizar en esta interacción, estudiando las rutas de endocitosis específicas que las células utilizan para internalizar ambos agentes. Estas rutas vienen determinadas por algunas de las propiedades físicas y químicas de los agentes a endocitar, como el tamaño, la forma, la carga superficial y la composición. En los resultados expuestos en este capítulo se determina que el mecanismo que las células utilizan para endocitar las bacterias magnetotácticas y los magnetosomas es diferente: mientras que las primeras son endocitadas principalmente mediante endocitosis dependiente de receptores, los segundos son endocitados preferentemente mediante micropinocitosis o fagocitosis.

El objetivo del *Capítulo 2* es estudiar la eficacia de las bacterias magnetotácticas en hipertermia magnética. Para ello, se lleva a cabo un experimento *in vitro* en el cual se aplica un campo magnético alterno a células cancerosas que previamente han internalizado bacterias magnetotácticas. En primer lugar, se determina que las bacterias magnetotácticas no causan citotoxicidad en las células ya que no afectan ni a su viabilidad ni a su capacidad de proliferación. En segundo lugar, se estudia el efecto del tratamiento de hipertermia magnética sobre las células. En este caso, se observa que tanto la viabilidad como la capacidad de proliferación de las células cancerosas expuestas al tratamiento de hipertermia se ven afectadas de manera significativa. Con todo esto se concluye que las bacterias magnetotácticas son candidatas prometedoras para ser utilizadas como agentes en hipertermia magnética para tratar el cáncer.

En el *Capítulo 3* se estudia el devenir intracelular de los magnetosomas a largo plazo. Con ello se pretende determinar el tiempo en el cual los magnetosomas siguen manteniendo su integridad tras la internalización en las células y, por tanto, permanecen útiles para tratamientos biomédicos reiterativos. Dicho

de otro modo, el objetivo es estudiar la capacidad de las células para "deshacerse" de los magnetosomas. Para ello el estudio se realiza en dos tipos celulares: células cancerosas de la misma línea que en los dos capítulos anteriores, y macrófagos. Las células cancerosas se utilizan dado que son el objetivo de los tratamientos biomédicos propuestos y, por lo tanto, es importante entender lo que ocurre con los magnetosomas tras su internalización. Los macrófagos se eligen también para este estudio por ser células del sistema inmune responsables de interiorizar y deshacerse de los agentes externos que entran en el cuerpo, como los patógenos o las nanopartículas. Además, tienen un papel fundamental en la homeostasis del hierro.

En este estudio se cultivan los dos tipos celulares mencionados con magnetosomas y se mantienen hasta 20 días en el caso de las células cancerosas y hasta 13 días en los macrófagos. Cada cierto tiempo se hacen diferentes medidas que permiten dilucidar que el destino intracelular de los magnetosomas depende de tres factores. Por un lado, los magnetosomas se reparten entre las células hijas a medida que prolifera la población celular y por tanto, la cantidad de magnetosomas por célula se va reduciendo con el tiempo. En segundo lugar, las células expulsan hierro al medio externo, bien en forma de magnetosomas o en otras especies de hierro resultantes de una posible degradación de éstos. Por último, los magnetosomas se degradan dentro de los lisosomas resultando en otras fases de hierro: maghemita, ferrihidrita y goethita. La aparición de ferrihidrita y goethita sugiere que las células utilizan los productos de degradación de los magnetosomas para cargar ferritina y hemosiderina, respectivamente. Asimismo se concluye que la permanencia de los magnetosomas dentro de las células depende del tipo celular: la eficiencia en su eliminación es menor en células cancerosas de pulmón que en macrófagos.

En el *Capítulo 4* se presenta un estudio en el cual el objetivo es tunear las características de las bacterias magnetotácticas mediante la incorporación de elementos químicos, en este caso, terbio y gadolinio. Para ello, se cultivan las bacterias magnetotácticas en un medio suplementado con los elementos mencionados y se estudia su incorporación mediante diversas técnicas. Asimismo, se analizan las propiedades magnéticas, estructurales y morfológicas de las bacterias modificadas. De estos estudios se concluye que el cultivo de bacterias magnetotácticas en medio suplementado con terbio y gadolinio promueve la incorporación de estos elementos en la estructura del magnetosoma y en otros compartimentos bacterianos. Dicha incorporación modifica las propiedades magnéticas tanto de los magnetosomas como de las bacterias sin que se ob-

serven cambios significativos en sus características morfológicas. Además, las bacterias magnetotácticas y los magnetosomas que han incorporado terbio presentan propiedades fotoluminiscentes. Por último, se verifica que la incorporación de terbio y gadolinio no cambia el potencial citotóxico de las bacterias magnetotácticas ya que, al igual que las bacterias cultivadas en condiciones estándar, no afectan a la viabilidad ni al potencial de crecimiento de las células cancerosas.

Por último, el objetivo del *Capítulo 5* es abrir el camino a nuevas líneas de estudio en el grupo de investigación. Además de las bacterias magnetotácticas de la especie *Magnetospirillum gryphiswaldense* MSR-1 utilizadas en los capítulos anteriores, se han establecido las condiciones de cultivo adaptadas a nuestras instalaciones de otras tres especies con las que el grupo de investigación no tenía experiencia previa. En este capítulo se recogen estas estrategias de cultivo, así como las principales características morfológicas, magnéticas y estructurales de dichas especies. En la segunda parte del capítulo se explica una técnica de ingeniería genética utilizada para la modificación de las características de los magnetosomas. Con ella se obtienen magnetosomas fluorescentes gracias a la expresión de la proteína Venus en la membrana de los magnetosomas. Además, también se expresa un péptido pegado a la proteína Venus, el péptido RGD. Este péptido se une con gran afinidad a los receptores de integrinas, los cuales aparecen sobreexpresados en la superficie de las células cancerosas, promoviendo por lo tanto la internalización de los magnetosomas.

# Introduction

Magnetotactic bacteria (MTB) are aquatic microorganisms able to passively align parallel to the Earth's magnetic field lines while swimming actively. This behavior known as magnetotaxis, is due to the presence of intracellular magnetic organelles called magnetosomes [1–4]. Magnetosomes are intracellular inclusions composed by a core of magnetic iron mineral, typically magnetite ($Fe_3O_4$) or greigite ($Fe_3S_4$), enclosed by a proteolipidic membrane.

MTB were first discovered in 1963 by Salvatore Bellini who observed a group of bacteria swimming northward in drops of samples collected from freshwater environments near Pavia (Italy) [5, 6]. He called these organisms "batteri magnetosensibili" or magnetosensitive bacteria and postulated that their behavior was caused by an internal "magnetic compass", a fact that he did not prove. However, this discovery went unnoticed for many years as his papers were published in his university journal and in Italian. In 2009 they were translated to English and republished [7, 8]. Richard P. Blakemore rediscovered MTB independently in 1974 [9]. He was the first to observe the internal magnetic compass proposed by Bellini and to suggest the term *magnetosome*.

It is important to notice that the term "magnetotactic bacteria" does not have any taxonomic relevance as it comprises a group of microorganisms phylogenetically very diverse. Most MTB described so far belong to the *Proteobacteria* phylum, especially to four of its subdivisions (*Alpha-*, *Beta-*, *Gamma-* and *Deltaproteobacteria* classes). However, some MTB are also found in the *Nistrospirae* and *Omnitrophica* phyla [10–12].

This wide phylogenetic distribution is reflected in their morphological and physiological diversity. Different morphotypes of MTB have been found such

as spirilla, cocci, rod-shaped, vibrios, and even multicellular bacteria [3, 13] (Figure 1A-D). Moreover, MTB have developed different metabolic strategies. In terms of their relationship with oxygen, obligate microaerophiles, anaerobes, or both, are known. There are some that obtain energy from organic or inorganic compounds and that can use organic compounds, carbon dioxide or both as a carbon source. Furthermore, some MTB are able to fix environmental nitrogen [3]. Such metabolic diversity has allowed MTB to colonize different ecological niches, even in extreme conditions of pH, salinity, or temperature [13–15].

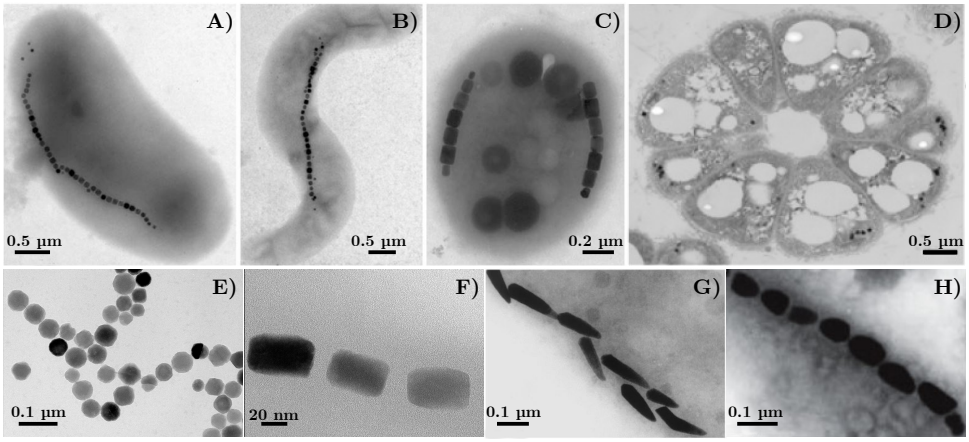


Figure 1: TEM images of magnetotactic bacteria and magnetosomes. Top: Diversity of bacterial shape: A) rod-shaped, strain BW-2; B) spirillum, strain CB-1; C) ovoid shape of an uncultured MTB; D) multicellular, *Candidatus* Magnetoglobus multicellularis. Bottom: crystal morphologies of magnetosomes: E) cuboctahedral; F) elongated prismatic; G) bullet-shaped; H) tooth-shaped. Adapted from Bazylinski *et al.* [3] (A-C), Araujo *et al.* [16] (D), Schüler *et al.* [17] (G) and Uebe *et al.* [18] (H).

The most widely accepted justification for the magnetic behavior of these microorganisms is the one proposed by the so-called magnetoaerotactic hypothesis [19–21]. According to this model, the production of magnetosomes responds to the need of MTB to find optimal zones of oxygen and nutrients, in the oxic/anoxic transition zone (OATZ). Bacteria living in the OATZ are continually searching the optimal position in the stratified water column in order to satisfy their optimal nutritional requirements. Under these circumstances, magnetotaxis is thought to be a great advantage by increasing the efficiency of chemotaxis. The geomagnetic field lines act as a vertical pathway in a

stratified environment so that the aligned MTB reduce a three dimensional search to a single dimension, swimming up and down in the water column (Figure 2). Other possible roles have been suggested for magnetosomes as detoxifying agents scavenging metal ions or eliminating intracellular reactive oxygen species [22, 23].

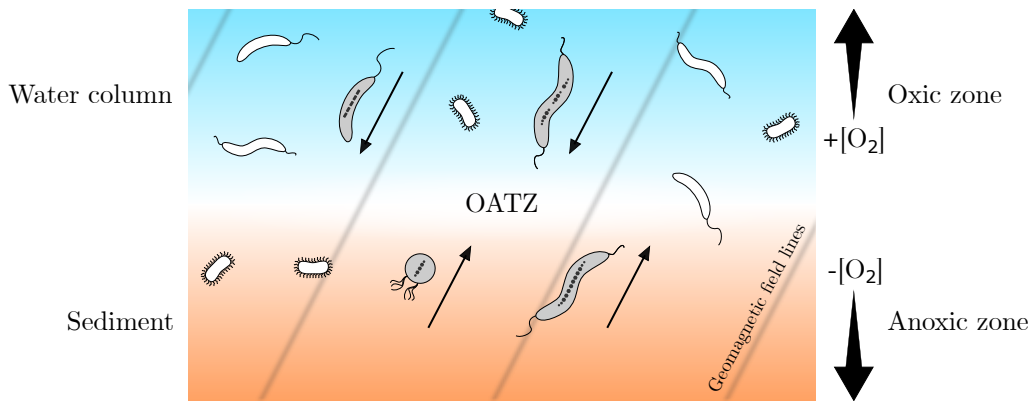


Figure 2: Schematic model of magnetotaxis in the oxic/anoxic transition zone (OATZ).

Magnetosome characteristics differ among MTB species, but are consistent within a single species. This reflects that magnetosome synthesis is under fine genetic control. The crystal morphologies fit to four main patterns: cuboctahedral, elongated prismatic, bullet-shaped, and tooth-shaped [18] (Figure 1E-H). The size of the magnetic crystals also varies among species, ranging from around 35 to 120 nm. Nevertheless, each species synthesizes magnetosomes with a characteristic morphology and a narrow size distribution. Interestingly, the size of magnetosomes always remains within the range of the room-temperature stable single-magnetic domain particles [1, 3, 24]. Magnetosomes comprise two components: the mineral core and the organic envelope. The mineral core presents high chemical purity, being magnetite $Fe_3O_4$ or greigite $Fe_3S_4$. The magnetic core is surrounded by a proteolipidic membrane that controls de biomineralization process [25–27]. Magnetosome membrane is originated by invagination of the cytoplasmic membrane and can be observed within the cell, as empty vesicles, before the formation of the mineral phase [27, 28]. As expected, the lipid composition of the magnetosome membrane is similar to that of the cytoplasmic membrane. However, the inserted proteins are special functional proteins involved in the synthesis of the mineral core [18, 25]. Magnetosomes are mainly arranged in one or more chains

positioned within the long axis of the cell. This arrangement causes the sum of the moments of the individual magnetosomes and turn the cell into a single magnetic dipole that functions as a magnetic needle enabling the bacteria to passively align with magnetic fields [24, 29]. The chain formation is guided by specific cytoskeletal elements, which anchor the chain in a certain position within the cell [27,30,31]. The underlying genetic control is the reason why the size, shape, chemical composition, and intracellular arrangement vary among species but remain nearly invariant in each one.

In this thesis the experiments have been performed with the MTB species *Magnetospirillum gryphiswaldense* MSR-1 taking advantage of the research group's previous experience with this strain. *M. gryphiswaldense* was isolated by Schüler *et al.* [32] from the mud of the river Ryck near Greifswald (Germany). As observed in Figure 3 MSR-1 have a spirillum or helical shape with a length ranging from 3 to 10 µm depending on their growing stage. These bacteria are motile thanks to two polar flagella that they use to swim. MSR-1 synthesize one chain of around 25 magnetosomes along the longitudinal axis of the bacteria. Magnetosomes of MSR-1 are formed of magnetite crystal and present a cuboctahedral shape with a mean diameter of 42 ± 10 nm. The research group has studied different aspects of *M. gryphiswaldense* such as the process of biomineralization [33,34], the configuration of the magnetosome chain [31], the tunability of the magnetosomes [22, 35, 36], or the use of the magnetosomes in magnetic hyperthermia [37].

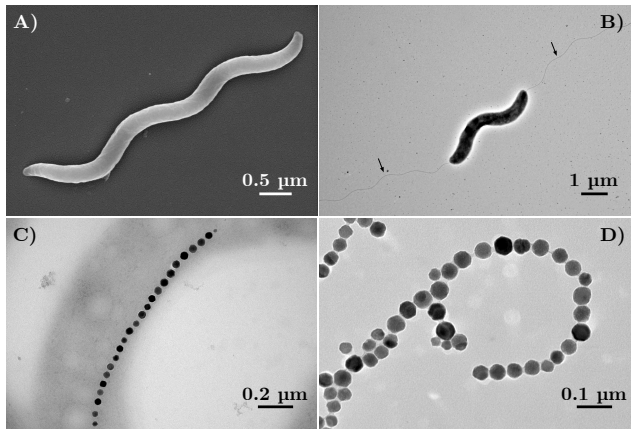


Figure 3: Electron microscopy images of *Magnetospirillum gryphiswaldense* MSR-1. A) SEM image showing the helicoidal shape of MSR-1; B) TEM image where bacterial flagella can be observed (indicated with black arrows); C) TEM image showing the magnetosome chain in detail; D) TEM image of isolated magnetosomes.

# Biomedical applications of magnetosomes and MTB

On top of their uniform size and shape, chemical purity, and easy reproducibility, magnetosomes display a high magnetic moment and are monodomain and magnetically stable at room temperature. Moreover, they are surrounded by a proteolipidic membrane that confers them stability avoiding aggregation of extracted magnetosomes, easy functionalizability, and biocompatibility. These outstanding properties make magnetosomes ideal candidates for a number of biomedical applications related to cancer treatment and diagnosis, such as magnetic hyperthermia, magnetic resonance imaging, and drug delivery [38–41].

Magnetic hyperthermia is a therapy that aims at debilitating cancer cells by delivering heat to them [42]. In magnetic hyperthermia magnetic nanoparticles are attached to or internalized into tumor cells and an alternating magnetic field (AMF) is applied. Under the action of the AMF magnetic nanoparticles dissipate energy that leads to a temperature increase of the tumor up to 40 - 45 °C causing the death and/or debilitation of cancer cells without affecting the surrounding healthy tissue [43]. Magnetosomes exhibit high heating efficiency under AMFs within the clinical limits, constituting ideal candidates for magnetic hyperthermia [37, 44–47]. Magnetosome-mediated magnetic hyperthermia has been successfully tested causing cell death and inhibiting cell growth *in vitro* [37] and inhibiting tumor growth [48] or eliminating tumors [49] *in vivo*.

Magnetosomes also offer great potential as diagnosis tools. As other magnetic nanoparticles, they can be used as magnetic resonance imaging (MRI) contrast agents as they shorten the $T_2$ relaxation time [50]. Based on *in vitro* relaxometry measurements, magnetosomes show an improved MRI contrasting performance than commercially available iron oxide magnetic nanoparticles leading to a significant gain in MRI sensitivity [51]. The potential of magnetosomes as MRI contrast agents has been demonstrated *in vivo* [44, 51–54]. Moreover, magnetosomes have proven successful as tracer materials in another diagnostic imaging technique: magnetic particle imaging (MPI) where they have shown an improved resolution than the currently used commercial tracer Resovist® [55].

Alternatively, magnetosomes are also investigated for targeted drug delivery purposes. The main goal is to properly functionalize the surface of magnetosomes with a specific drug and, through the application of a magnetic field gradient, to transport the magnetosomes towards the tumor where the drug will act [56]. Functionalization can be achieved by chemical modification of the isolated particles or by genetic engineering by fusing the genes codifying enzymes or proteins of interest to those codifying magnetosome membrane proteins. Chemical surface modification has been used to functionalize magnetosomes with anticancer drugs such as cytosine arabinoside (Ara-C) [57] and doxorubicin (DOX) [58]. Chemical reactions have also been used to link gold nanoparticles to the surface of magnetosomes. These Au-magnetosomes have shown a good performance in photoacustic imaging, MRI, magnetic hyperthermia and photothermia [59]. Genetic engineering has been used to functionalize magnetosomes with fluorescent proteins which make easier the tracking [52, 60–62], and other peptides and proteins that bind specifically to receptors overexpressed in tumor cells [52, 61, 63].

Magnetosomes have also proven successful in other anticancer treatments. For instance, they have shown high heating efficiency in photothermia resulting in a decrease of cell viability *in vitro* and a complete inhibition of tumor growth *in vivo* [61]. Recently, magnetosomes have been successfully tested as radioenhancers in radiotherapy promoting the damaging action of X-rays *in vitro* and *in vivo* [60].

Unfortunately, there are several intrinsic limitations associated to the use of magnetosomes. The main disadvantage is the difficulty and low yield of magnetosome extraction and purification procedure. Moreover, such as other magnetic nanoparticles, magnetosomes have limited penetration through biological barriers and uneven distribution in the tumor tissue. In order to bypass these difficulties the use of whole magnetotactic bacteria has been proposed. Magnetotactic bacteria combine the guidance, control and therapeutic capabilities of isolated magnetosomes with motility, chemical specificity and the capacity of being genetically modified of bacteria. Moreover, MTB are non-pathogenic but could be modified to deliver and/or express certain cytotoxic molecules. Another inherent advantage of MTB is their preference for microaerophilic environments, such as tumor zones.

Recently, the heating efficiency in magnetic hyperthermia of *M. gryphiswaldense* [64,65] and *Magnetospirillum magneticum* [66] has been studied with

promising results. *Magnetococcus massalia*-mediated magnetic hyperthermia has been successfully tested to kill *Staphylococcus aureus* (a pathogen that causes skin and soft tissue infections) [67]. MTB have also been proposed as drug delivery carriers. It has been shown that *M. magneticum* can navigate in capillaries and target mouse tumor xenografts [68] and that *Magnetococcus marinus* carrying drug-loaded nanoliposomes can be magnetically guided toward hypoxic regions of colorectal xenografts [56].

In view of these studies, MTB are promising candidates in bacterial cancer therapy. It should be noted that the use of bacteria in cancer treatments is not far-fetched. The first bacteria-mediated cancer treatment dates back to the end of the XIX century [69–72]. Despite initial skepticism, bacterial-mediated cancer therapy progressed. Nowadays, Bacillus Calmette-Guerin (BCG) is used for the treatment of superficial, non-muscle invasive bladder cancer [73] and several bacterial-mediated cancer treatments have been approved for clinical trials by the Food and Drug Administration (FDA) [74].

## Thesis structure

The present work addresses several aspects of the use of MTB in biomedical applications. The thesis has been structured in five chapters.

Most of the proposed biomedical applications for MTB need them to be internalized by targeted cells. Thus, *Chapter 1* intends to elucidate the interaction of MTB and magnetosomes with cells. The endocytic route that cancer cells use to internalize MTB and magnetosomes is also examined.

In *Chapter 2* the therapeutic potential of whole MTB as magnetic hyperthermia agents is presented. The results of a MTB mediated magnetic hyperthermia *in vitro* study are displayed examining the cytotoxicity of MTB and the efficiency for this treatment.

Once MTB enter the cells, following their fate is essential to determine the time in which their magnetosomes are still effective for biomedical applications and to understand the later intracellular degradability and clearance. *Chapter 3* aims to study the long-term fate of magnetosomes inside cells. The magnetic and structural changes that they undergo in the long-term is examined and

the iron species that arise over time are determined.

Aiming to improve the intrinsic characteristics of MTB, in *Chapter 4* the intention is to tune their magnetic response by culturing them in presence of two rare earth elements: terbium and gadolinium. The optimal culture conditions are established and the incorporation of the rare earth elements into the bacteria are verified. The magnetic, structural and morphological properties of the modified MTB are studied.

*Chapter 5* provides an outlook for new opportunities in the research group. The culture strategies and the morphological and magnetic characteristics of other species of MTB besides *M. gryphiswaldense* are presented. Last, a genetic engineering technique to modify magnetosome characteristics is presented.

Finally, the document includes the methodology and bibliography used throughout the thesis, as well as the resulting publications.

# Chapter 1

# Interaction of magnetotactic bacteria and magnetosomes with cancer cells

Even if there are many barriers that MTB and magnetosomes have to overcome when entering the body, the ultimate factor determining the efficiency of the biomedical application to be used is their ability to interact with the target cells by adhering to or entering them. Therefore, knowledge of this process is essential to improve the efficiency of the biomedical applications to be used.

Another reason for the importance of understanding the route that MTB and magnetosomes use to enter cells is that it can define their fate inside them which can determine their suitability in certain treatments. One of the main problems of the use of nanoparticles in biomedical applications is that they are often rapidly detected by the mononuclear phagocytic system (MPS) cells [75], the first line of defence of the organism against foreign agents, and delivered for expulsion from the body to the liver and spleen, where they tend to accumulate. This not only provokes a decline in the treatment efficiency but also can cause toxic side effects. Therefore, it is of major importance to avoid the clearance by MPS cells and this can be exploited by understanding the uptake process in the cell type that wants to be targeted.

The plasma membrane is the cell structure responsible for the separation

of the cytoplasm and the extracellular environment and it therefore regulates the molecule and particle exchange between these two compartments. There are two main mechanisms of entry into cells: direct fusion with the plasma membrane, a passive route used by some encapsulated viruses, or endocytosis, an active mechanism that is the main route for bigger cargoes such as nanoparticles or microorganisms [76]. Endocytosis includes several mechanisms that consist of the engulfment of the cargo in plasma membrane invaginations that form endosomes or phagosomes that then deliver the cargo to specialized vesicular structures in the cell [77].

The aim of this chapter is to study the interaction of magnetotactic bacteria and magnetosomes with cancer cells. For this, whole bacteria and isolated magnetosomes from *Magnetospirillum gryhiswaldense* MSR-1 were put in contact with A549 human lung carcinoma cells. First, a quantitative and qualitative analysis of the interaction was performed by means of magnetic measurements and several microscopy techniques. Finally, the specific endocytic pathway that MSR-1 and magnetosomes use to enter A549 cells was determined by using chemical inhibitors.

## 1.1 Study of the interaction by magnetometry and microscopy

To verify the internalization of MSR-1 and their isolated magnetosomes, both a quantitative analysis through magnetic measurements as well as a qualitative analysis by means of several microscopic techniques were performed. The scheme of the experimental design is represented in Figure 1.1. A549 cells were co-incubated with MSR-1 or isolated magnetosomes for 2 h and, after washing, cells were further incubated overnight to promote the internalization. Then, magnetic and microscopic analyses were performed.

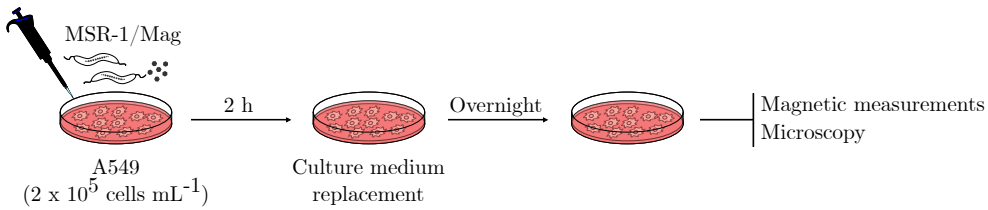


Figure 1.1: Scheme of the experiment carried out to verify the internalization of MSR-1 and magnetosomes in A549 cells.

The optimal magnetosome concentration to add to the cells was set in 30 µg $mL^{-1}$ according to previous studies [37]. However, the optimal bacterial concentration was not yet established and, therefore, several MSR-1 concentrations were tested. The amount of magnetite caught by A549 cells was calculated from the saturation values of the hysteresis loops of the cells measured by VSM magnetometry (see Materials and Methods). The results are displayed in Figure 1.2. When cells were co-cultured with $10^9$ bacteria $mL^{-1}$ they were able to accumulate 0.3 pg magnetite, which corresponds to approximately 33 bacteria per cell assuming that one bacterium contains 7 fg of magnetite (estimated from VSM measurements). However, when the concentration of MSR-1 was of $5 \times 10^9$ bacteria $mL^{-1}$, cells took up to 3.5 pg of magnetite per cell, which corresponds to 450 bacteria. As this concentration is the one for which cells are able to internalize more magnetite, it was established to be used in further experiments. When cells were incubated with 30 µg $mL^{-1}$ of magnetosomes they were able to take up to 25 pg of magnetite per cell.

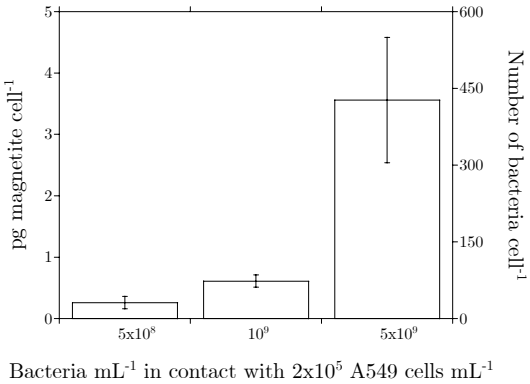


Figure 1.2: Amount of magnetite and number of MSR-1 accumulated by A549 cells. Data represent the mean ± standard deviation, n = 3.

Magnetic measurements allow the quantification of the mass of magnetite that cells are able to uptake. However, it is not possible to determine whether this magnetite is inside the cells or attached to their surface. In order to prove the internalization of MSR-1 and magnetosomes, several microscopy techniques were used. First, cells were observed under a bright field and fluorescence microscope. For this, A549 cells were stained with Hoechst 33342 that binds to the DNA, conferring blue fluorescence to cell nuclei. MSR-1 were stained with rhodamine 123, which makes them fluoresce green. In the case of magnetosomes, they already have good contrast under bright field due to

their high density that does not allow the light to pass through. In Figure 1.3, examples of these images are shown. For A549 cells loaded with MSR-1, composite images of blue/green fluorescence channels are displayed. In the case of magnetosome-loaded cells, the images shown are composite images of bright field and blue fluorescence channel.

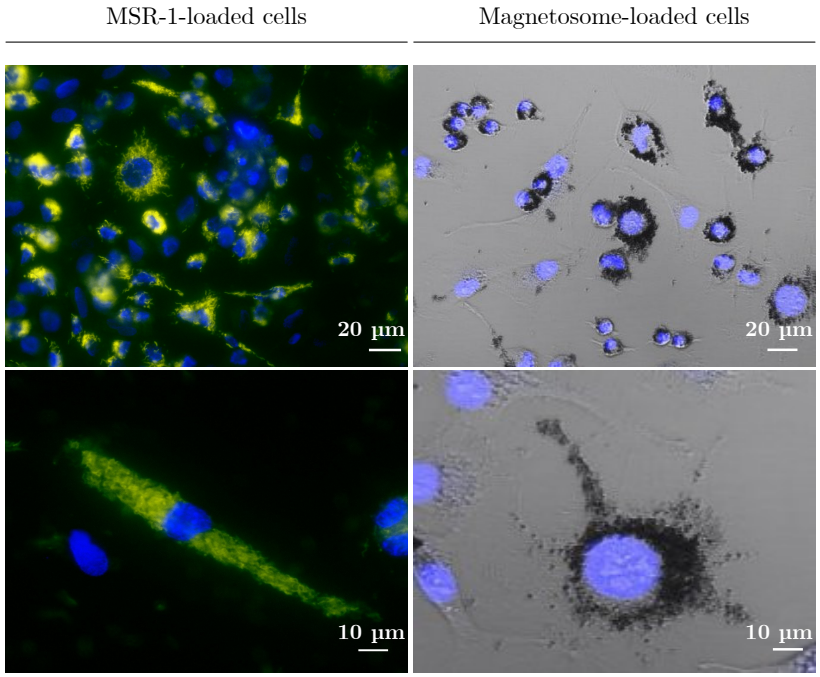


Figure 1.3: Composite microscopy images of A549 cells loaded with MSR-1 (blue/green fluorescence) and isolated magnetosomes (bright field/blue fluorescence). Cell nuclei are shown in blue as they are stained with Hoechst 33342, MSR-1 are displayed in green since they are stained with rhodamine 123 and magnetosomes are seen as dark spots.

From these images it can be inferred that A549 cells interact with both MSR-1 and magnetosomes. Moreover, the fact that they appear only in the cell cytoplasm but not in their nuclei may indicate that MSR-1 and magnetosomes are inside cells. If MSR-1 or magnetosomes were attached to the surface, an overlap of green fluorescence or dark particles would be observed on the nuclei.

To more closely examine MSR-1/magnetosome-cell interactions, electron microscopy was used. Some examples of the obtained images are presented in Figure 1.4. Scanning electron microscopy (SEM) images were colored using

GIMP software to better distinguish both MSR-1 (yellow) and isolated magnetosomes (pink) from cellular surface structures. MSR-1 and magnetosomes can be seen adhered to the surface of A549 cells, both isolated and forming aggregates that are more obvious in the case of magnetosomes. Finally, ultra-thin sections were analyzed by transmission electron microscopy (TEM). With this technique both MSR-1 and magnetosomes can be observed inside cells directly, where magnetite nanocrystals in endosome-like vesicles are visible. MSR-1 can be distinguished inside cells thanks to their magnetosomes. It can be observed that cells are able to uptake less magnetic material when they are co-cultured with MSR-1 than in the case of magnetosomes, which is in agreement with magnetometry results.

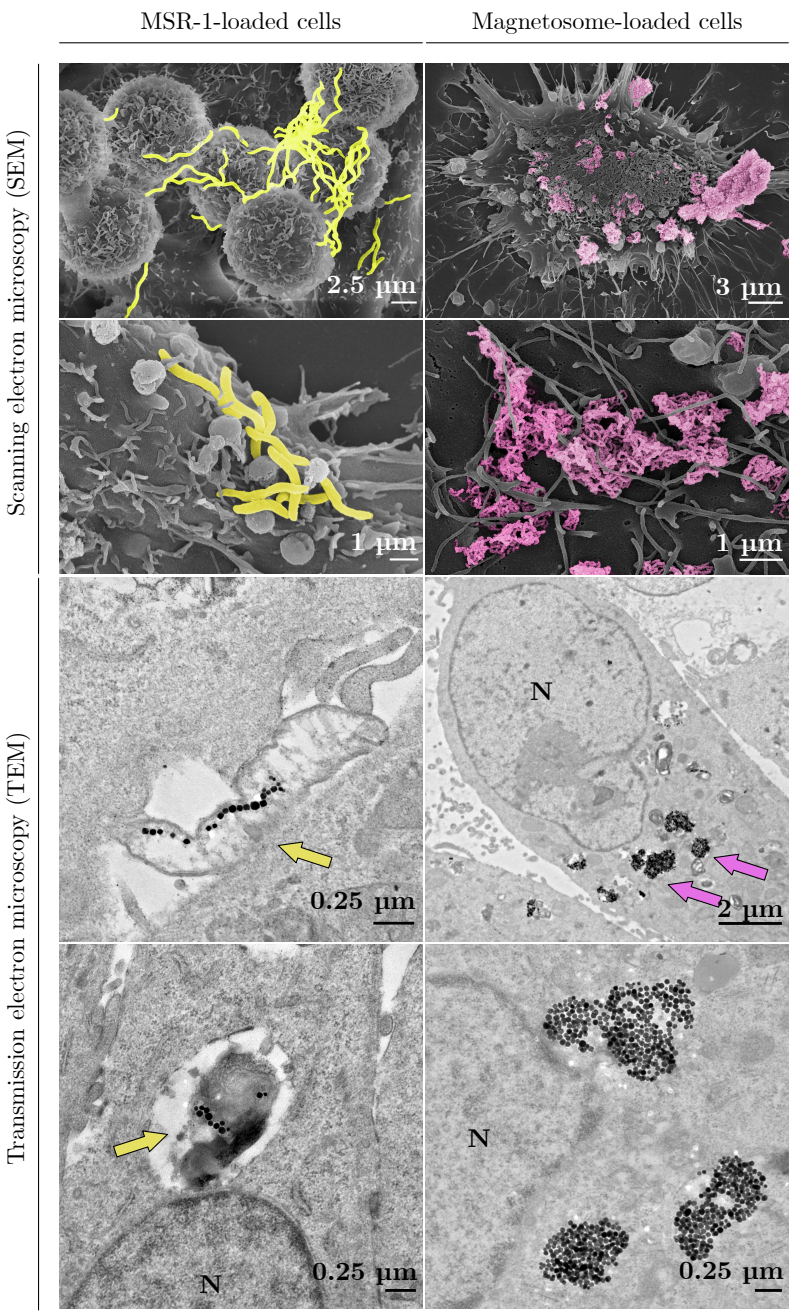


Figure 1.4: SEM and TEM images of MSR-1-loaded cells and magnetosome-loaded cells. MSR-1 and magnetosomes were colored in SEM images to better distinguish them from cellular structures. In the case of TEM images, MSR-1 and magnetosomes in cell slides are indicated with arrows and the nuclei of cells are marked N.

## 1.2 Internalization pathways

The fact that MSR-1 and their magnetosomes are observed inside cells in endosome-like vesicles suggests that their uptake process is performed by endocytosis. This process can be classified into two main routes that coexist in cells and that are used depending on the physical and chemical properties of the cargo that has to be internalized: phagocytosis and pinocytosis (Figure 1.5).

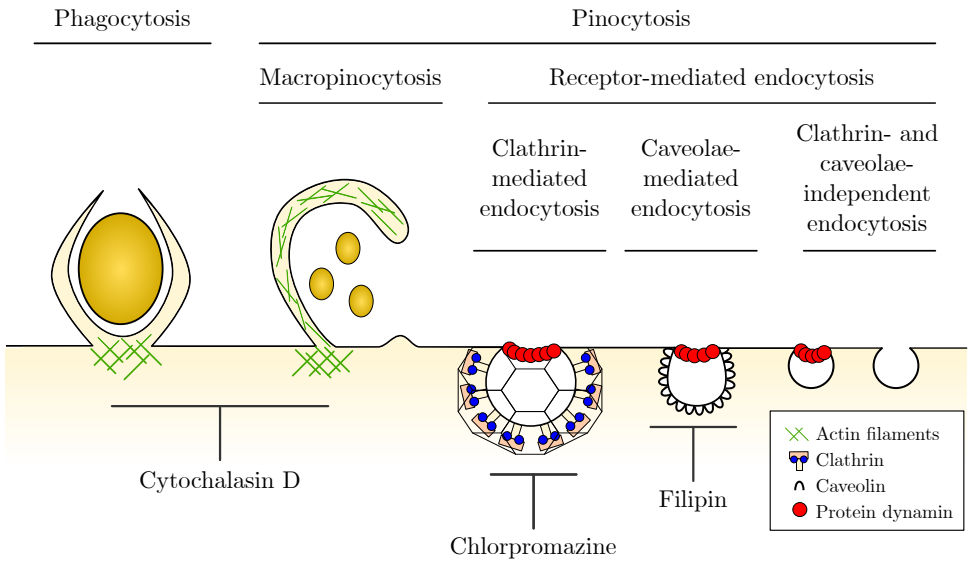


Figure 1.5: Classification of endocytic pathways and chemical inhibitors used in this work to block specific endocytosis routes.

Phagocytosis is primarily considered to be involved in the uptake of particles over 0.5 µm in diameter though the lower size limit is unclear, meaning it could be involved in the endocytosis of nanoparticles as well [76]. Although it is most frequently used by professional phagocytes (macrophagues, neutrophils, or dendritic cells) phagocytosis can also take place in non-professional phagocytes [78].

Pinocytosis is used by cells for the internalization of fluids containing solutes and particles by forming vesicles smaller than those formed in phagocytosis [79]. Depending on whether the pinocytosis mechanism is selective or not, it can be further classified into receptor-mediated endocytosis or macropinocytosis. Based on the proteins involved in the endocytic process, receptor-mediated

endocytosis can be classified into three main mechanisms: clathrin-mediated endocytosis, caveolae-mediated endocytosis and clathrin- and caveolae-independent endocytosis [80].

Several methods have been proposed for determining the endocytic route responsible for a specific cargo internalization. Among the most used ones are the colocalization of nanomaterials with specific endocytosis markers and structures and the exclusion of endocytic pathways by using specific chemical inhibitors or cell mutants [76, 77].

In this study, three selective chemical inhibitors were tested (see Figure 1.5) to identify the route A549 cells use to internalize MSR-1 and isolated magnetosomes: cytochalasin D which inhibits actin polymerization and, therefore, endocytosis through phagocytosis and macropinocytosis [81, 82]; chlorpromazine that inhibits clathrin-coated pit formation thus inhibiting clathrin-mediated endocytosis [83]; and filipin which disrupts the caveolae distribution within the cell membrane by binding to sterols such as cholesterol and by disorganizing caveolin inhibiting caveolae-mediated endocytosis [84].

To determine the optimal concentration, a previous experiment to check the effect of the chemical inhibitors on cell viability was performed. Cell viability was determined by propidium iodide staining and flow cytometry (see Materials and Methods). The results obtained are presented in Figure 1.6 where the viability values are normalized to those of control cells (cultured without inhibitor).

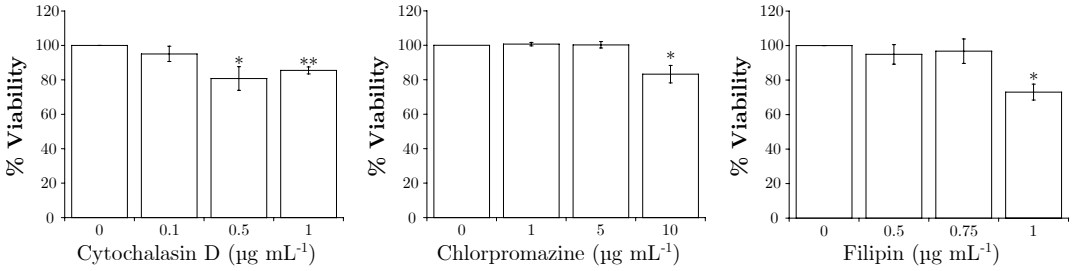


Figure 1.6: Viability of A549 cells after 2.5 hours in contact with increasing concentration of endocytosis inhibitors. The percentages are normalized to control cells cultured without inhibitor. Data represent the mean ± standard deviation, n = 3. *, $P < 0.05$; **, $P < 0.01$.

For cytochalasin D with a concentration of 0.1 µg $mL^{-1}$ the viability remained around 95 ± 4.5%. However, it decreased significantly when the concentration was increased to 0.5 µg $mL^{-1}$ with a viability of 81 ± 7%.

In the case of chlorpromazine, with a concentration up to 5 µg $mL^{-1}$, viability was not significantly affected and it remained above 95% in all replicates. Nonetheless, when the concentration increased to 10 µg $mL^{-1}$ it was significantly reduced to 83 ± 5%.

With filipin the viability was not affected with a concentration up to 0.75 µg $mL^{-1}$. However, it sharply decreased to 73 ± 4.5% with 1 µg $mL^{-1}$ of filipin.

Therefore, to avoid any side effects, the inhibitor concentrations shown in Table 1.1 were chosen for the internalization experiments.

| Selective inhibitor | µg $mL^{-1}$ | Endocytic route inhibited |
|---|---|---|
| Cytochalasin D | 0.1 | Phagocytosis and Macropinocytosis |
| Chlorpromazine | 5 | Clathrin-mediated endocytosis |
| Filipin | 0.75 | Caveolae-mediated endocytosis |

Table 1.1: Concentrations of endocytosis inhibitors used in the internalization experiments. The values were chosen as the maximum concentration for which cell viability was not significantly reduced.

The planning of the experiment performed to determine the endocytic routes cells use to internalize MSR-1/magnetosomes is shown in Figure 1.7. A549 cells were cultured in four different conditions: A) cells co-incubated with MSR-1/magnetosomes at 37 °C; B) cells co-incubated with MSR-1/magnetosomes at sub-optimal metabolic temperatures (4 °C); C) cells co-incubated with MSR-1/magnetosomes and with chemical inhibitors specific to certain endocytosis routes; and D) control cells without load nor inhibitors.

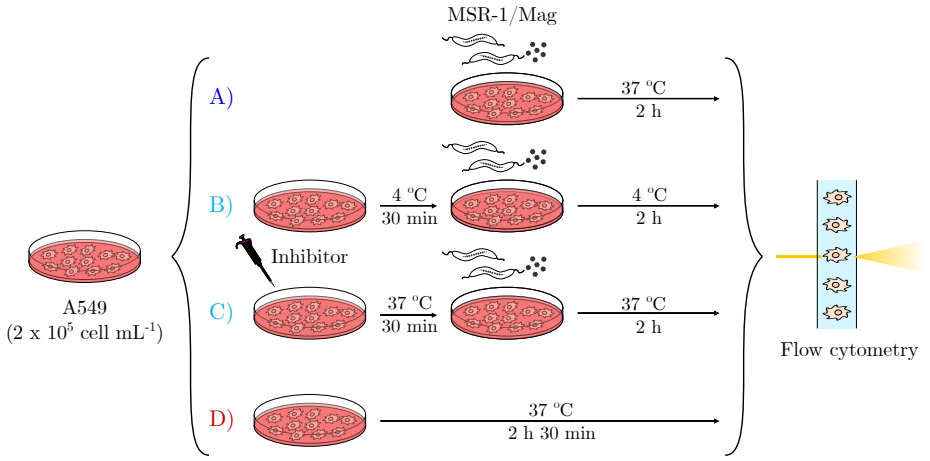


Figure 1.7: Scheme of the experiment performed to determine the endocytic routes used by A549 cells to internalize MSR-1/magnetosomes. Four sets of cells were cultured: A) MSR-1/magnetosome-loaded cells; B) MSR-1/magnetosome-loaded cells incubated at sub-optimal temperature (4 °C); C) MSR-1/magnetosome-loaded cells incubated with an inhibitory compound; and D) control cells.

The presence of MSR-1 and magnetosomes in contact with or inside cells was determined by flow cytometry (see Figure 1.8). It has been proven that nanoparticle-loaded cells have a higher value in side scattered light, probably as a result of the increased cellular complexity [85]. Therefore, side scatter values were used to estimate the magnetosome uptake by cells. However, the same effect cannot be observed in MSR-1-loaded cells probably due to their lower magnetosome amount. Consequently, for bacterial internalization analysis, MSR-1 stained with rhodamine 123 were used. As a result, MSR-1-loaded cells presented green fluorescence which was the factor used in this case for the internalization estimation. The endocytosis inhibition percentage was calculated using Equation 1.1.

$$\% \text{ Endocytosis inhibition} = \left(1 - \frac{\text{ID}}{\text{CD}}\right) \times 100 \tag{1.1}$$

where:

CD = difference between the mean values of green fluorescence/side scatter of loaded cells and control cells
ID = difference between the mean values of green fluorescence/side scatter of loaded cells with inhibitor (or 4 °C) and control cells

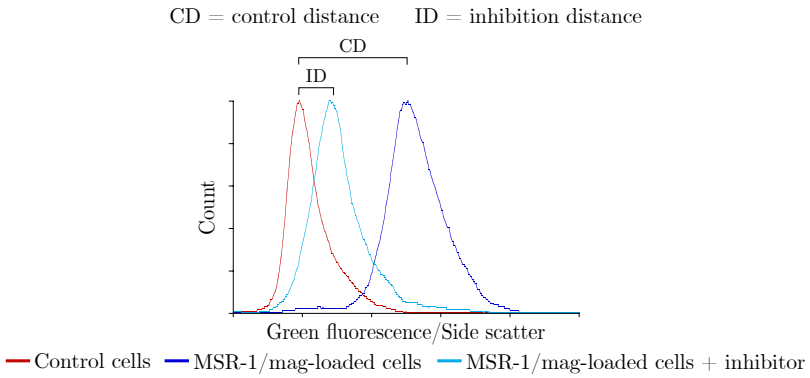


Figure 1.8: Green fluorescence/side scatter histogram of cells. The shifts of loaded-cells (CD) and loaded-cells + inhibitor (ID) with respect to control cells are indicated.

Endocytosis is an active mechanism meaning that is energy-dependent and, therefore, slows down at sub-optimal temperatures for cell metabolism. Then, to determine if A549 cells internalize MSR-1 and magnetosomes actively or not, cells were incubated at 4 °C along with MSR-1/magnetosomes (Figure 1.7B). The results are displayed in Figure 1.9. Although 4 °C is not the optimal temperature for cells, their viability was not affected. The uptake, on the contrary, was significantly reduced in the case of both MSR-1 and magnetosomes due to the decreased metabolic activity. There is a difference between the fluorescence intensity of cells incubated with MSR-1 at 37 °C and at 4 °C where it is more similar in position to the peak of control cells (Figure 1.9A). This means that cells have internalized less MSR-1 than when incubated at the optimal temperature of 37 °C. This effect was observed in the three experiments performed under these conditions with 85 ± 4% inhibition. For magnetosome uptake the side scattering peak is closer to the control cells when cells were incubated at 4 °C (Figure 1.9B). In this case the endocytic process was inhibited with a mean value of 54 ± 10%.

The fact that the inhibition percentage did not reach 100% for both MSR-1 and magnetosomes may indicate that they are also able to enter cells passively by fusing with the plasma membrane. In the case of magnetosomes, this fusion may be of greater importance as suggested by the lower inhibition percentage at 4 °C which may be explained by their higher ability to fuse with plasma membrane due to the phospholipidic composition of the magnetosome membrane, which is similar to that of the cells. Another reason that could possibly

explain the inhibition not being complete is that MSR-1 and magnetosomes can also remain attached to cell surface (Figure 1.4) which would be equally detected by flow cytometry.

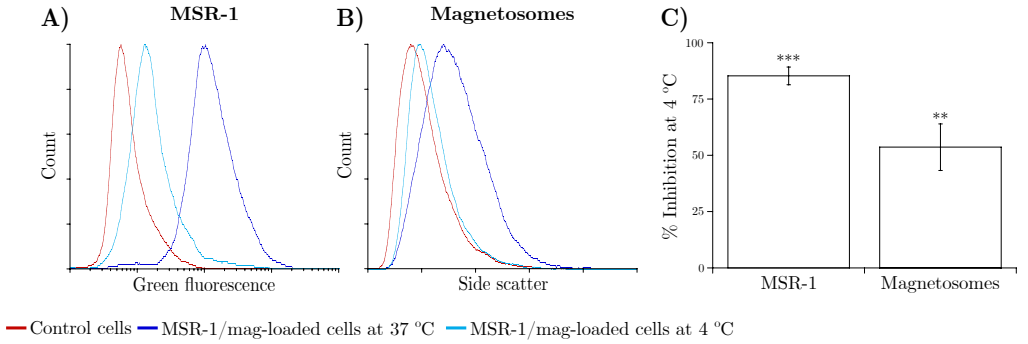


Figure 1.9: Inhibition of endocytosis provoked by incubation at sub-optimal temperatures (4 °C). Examples of A) green fluorescence and B) side scatter histograms used to calculate the inhibition percentages shown in C) are displayed. Data represent the mean ± standard deviation, n = 3. **, $P < 0.01$; ***, $P < 0.001$.

The specific endocytic route that microorganisms and nanoparticles use to enter cells is determined by some of their physical and chemical properties such as size, shape, surface charge and composition [86]. Therefore, once verified that MSR-1 and magnetosomes could enter cells by endocytosis, the specific pathways were determined by using chemical inhibitors (Figure 1.7C). The results are shown in Figure 1.10.

Due to the size of MSR-1 (around 0.5 × 5 µm) it would be intuitive to think that the preferred endocytic route for cells to carry out their uptake would be phagocytosis. However, cytochalasin D caused an almost negligible inhibition of MSR-1 internalization with a mean value of 3 ± 2% meaning that the main route used by A549 cells for bacterial internalization is neither phagocytosis nor macropinocytosis. Chlorpromazine and filipin, on the other hand, inhibited significantly MSR-1 internalization to some extent with mean values of 34 ± 9% and 37.5 ± 5.5%, respectively, meaning that A549 cells use receptor-mediated endocytosis to internalize MSR-1. This may be due to the presence of possible ligands on the bacterial surface that may be recognized by, and interact with cell receptors triggering both clathrin-mediated endocytosis and caveolae-mediated endocytosis.

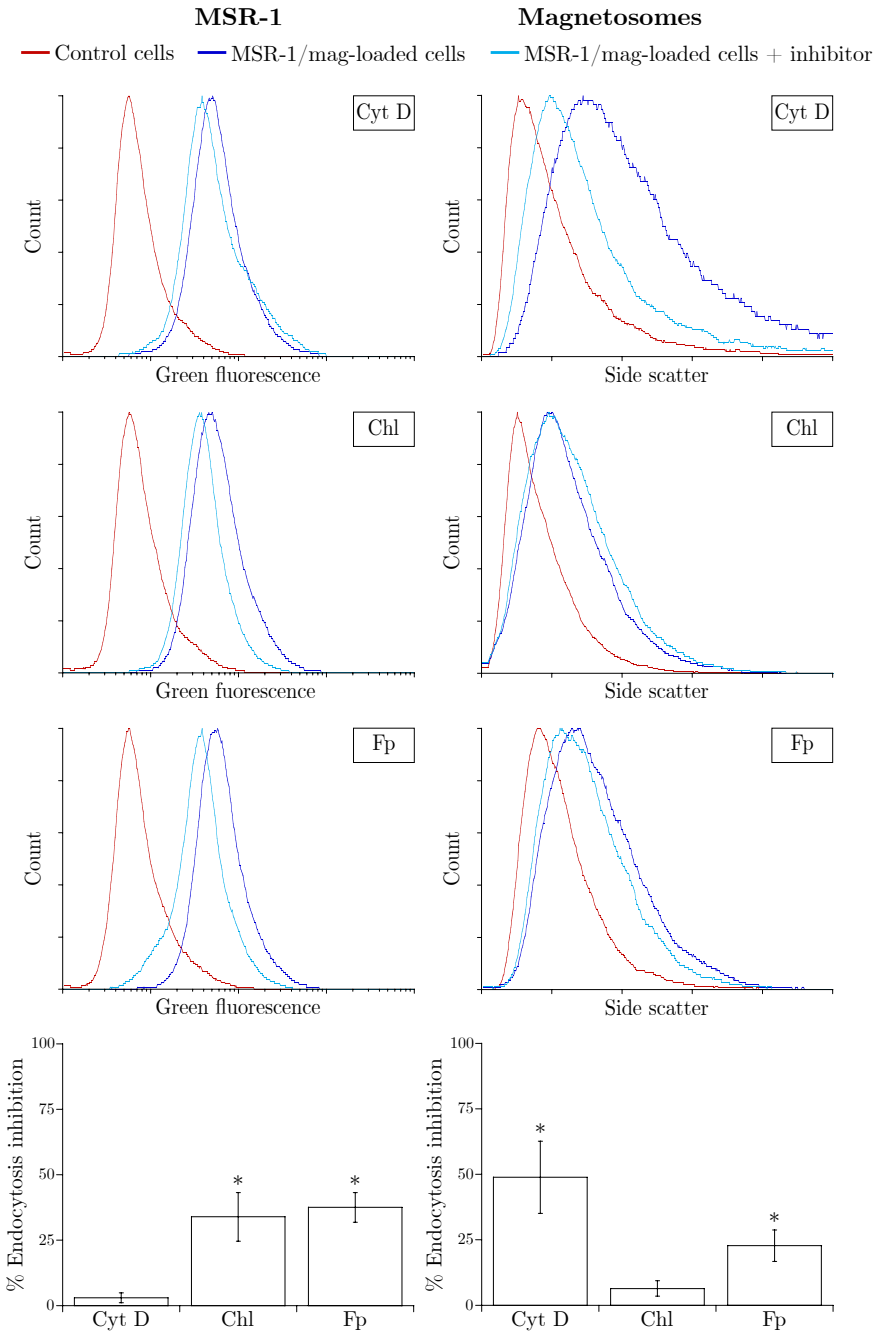


Figure 1.10: Inhibition of MSR-1/magnetosome endocytosis provoked by specific chemical inhibitors: cytochalasin D (CytD), chlorpromazine (Chl) and filipin (Fp). Examples of histograms showing the fluorescence intensity (left) and side scatter (right) used to calculate the inhibition percentage (bottom) are shown. Data represent the mean ± standard deviation, n = 3. *, $P < 0.05$.

On the contrary, magnetosome uptake was inhibited in the presence of cytochalasin D with a mean value of 49 ± 14% meaning that A549 cells can use phagocytosis or macropinocytosis to internalize magnetosomes. The nanoscopic size of isolated magnetosomes (around 40 nm) does not suggest this mechanism as the main one, but as they tend to aggregate in clusters as shown previously in SEM images (Figure 1.4), phagocytosis and macropinocytosis could enable their internalization. The fact that these two routes do not depend on specific protein receptors may suggest that magnetosomes do not have as many specific ligands on their surfaces to target as MSR-1 do. In fact, they are intracellular structures that remain inside bacteria without any contact with the outer environment. Additionally, magnetosomes may be able to be internalized by caveolae-mediated endocytosis since there was an inhibition of 23 ± 6% when blocked by filipin. Clathrin-mediated endocytosis may not be involved in magnetosome internalization as chlorpromazine caused only 6 ± 3% inhibition.

In a paper by Wang *et al.* [87], where magnetosomes from *Magnetospirillum magneticum* AMB-1 were tested in HepG2 cells, a reduction of magnetosome uptake was reported when phagocytosis, macropinocytosis and clathrin-mediated endocytic routes were inhibited, but not when the caveolae-mediated endocytosis was blocked. One reason to explain the difference between Wang *et al.* and the current study may be the use of different eukaryotic cells. Caveolae are present in many cell types, in some of which are of high density such as adipocytes, endothelial and muscle cells, where they can account for more than 50% of the plasma membrane. However, there is a very low concentration of caveolae in some tissues such as the liver and absent in others such as the kidney proximal tubule [88]. This could explain why the study from Wang *et al.* did not report any reduction in magnetosome uptake when caveolae-endocytic route was inhibited as the tested cells were from the liver, whereas the cells used for the present study are endothelial cells with higher density in caveolae. Another main difference between the study performed by Wang *et al.* and this work is the method used for measuring the internalization process. They used microscopy to qualitatively determine if cells treated with endocytosis inhibitors internalized magnetosomes or not. This technique is not very representative of the samples as the images only show a small amount of cells present in the sample, therefore they may not represent the whole population. On the contrary, using flow cytometry allows for the analysis of many more cells in one sample (10,000 in the case of this study) giving statistically more reliable results.

In addition, the fact that the sum of inhibition percentages caused by endocytosis inhibitors does not reach 100% may suggest that apart from passive internalization and/or attachment to cell surfaces, MSR-1 and magnetosomes may enter A549 cells by clathrin- and caveolae-independent endocytosis.

## 1.3 Conclusions

From the results displayed in this chapter it can be concluded that:

- Magnetotactic bacteria and magnetosomes interact with cancer cells and can be internalized into the cell cytoplasm by endocytosis.
- Magnetotactic bacteria and magnetosomes enter cancer cells by different endocytic pathways. Bacteria are internalized mainly by receptor-mediated endocytosis and magnetosomes by phagocytosis or macropinocytosis.

# Chapter 2

# Magnetotactic bacteria as magnetic hyperthermia agents

Magnetic hyperthermia (MHT) is a cancer treatment based on the conversion of magnetic energy to heat. Magnetic nanoparticles (MNPs) injected intratumoraly can work as agents for heat generation as a response to an alternating magnetic field (AMF) [89, 90]. The local temperature increases to a "therapeutic window" typically between 42 and 44 °C causing death or damage to cancer cells without affecting healthy tissue. This is possible because cancer cells have shown to be more susceptible to heating than healthy ones [42]. If the temperature is increased to values higher than 45 °C, which is known as thermal ablation, the obtained effect is more violent and can cause side-effects affecting healthy cells. Therefore, a careful control of the temperature increase during MHT is of major importance [89].

Magnetic hyperthermia was first proposed in 1957 by Gilchrist *et al.* [91] for the treatment of lymphatic metastases. However, it was not until the early 2000s that first Phase I clinical trials were performed for the treatment of prostate cancer [92] and glioblastoma multiforme [93]. These studies showed the feasibility, tolerance and efficacy of MHT, and due to the successful results, Phase II clinical trials were performed combining MHT with adjunct radiotherapy in patients with recurrent glioblastoma multiforme [94]. Currently, NanoTherm® therapy from the MagForce® company has the European approval for treatment of brain tumors. In 2018 they were awarded the Inves-

tigational Device Exemption by the Food and Drug Administration (FDA) to start a pivotal clinical study for patients with prostate cancer in the USA [95].

Compared to conventional chemotherapy and radiotherapy, MHT has the advantage of being a localized treatment and therefore having fewer side-effects. However, MHT is mostly used as an adjunct therapy with other conventional cancer therapies because it triggers several biological processes that can be taken advantage of to increase their efficacy [89]. Some of the better studied biological effects that hyperthermia causes in cancer cells are: an increase in reactive oxygen species that cause cytoxicity [96], alterations in the plasma and subcellular organelle membranes [97], sensitization of cells to DNA damaging agents through hampered DNA repair [98], and an increase in the surface molecular marker expression that can be recognized by immune cells for their elimination [42].

The heating efficiency as well as the *in vitro* and *in vivo* MHT performance of magnetosomes extracted from MTB has been thoroughly studied with favorable results [37, 49, 99]. However, the main advantage of working with whole bacteria is bypassing the magnetosome extraction process. Several studies measuring the heating efficiency of whole MTB have demonstrated promising results [64, 65, 100, 101]. Despite the heating efficiency of MTB being studied from a physical point of view, there are few works on the therapeutic effect that they may cause [66, 67].

The aim of this chapter is to test the suitability an efficiency of MTB in magnetic hyperthermia treatment against cancer cells. For this an *in vitro* experiment to study the hyperthermic response of *Magnetospirillum gryphiswaldense* MSR-1 in the presence of A549 lung carcinoma cells was performed. The cytotoxicity of MSR-1 was also assessed.

## 2.1 Magnetic hyperthermia with MSR-1: an *in vitro* study

In order to optimize the magnetic field parameters to be applied for the *in vitro* study, the heating efficiency of MSR-1 was characterized previously by our group [64]. The heat generation is expressed in terms of the specific absorption rate (SAR [W $g^{-1}$]) and depends on the amplitude, $H$, and frequency, $f$, of the applied AMF. Figure 2.1 shows the SAR values of MSR-1 as a function of the applied field amplitude for a fixed frequency of 149 kHz, similar to the frequency of the hyperthermia apparatus to be used later in this work (150 kHz). It must be remarked that the SAR values obtained for MSR-1 compared very well with some of the highest SAR values reported in the literature for iron oxide based nanoparticles [102].

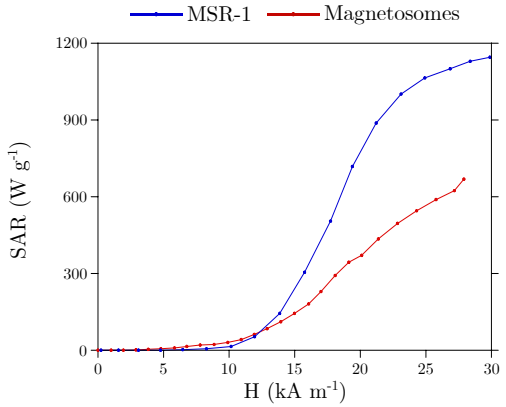


Figure 2.1: SAR as a function of the applied magnetic field amplitude for MSR-1 and isolated magnetosomes dispersed in water. Measurements were performed at a frequency of 149 kHz. Data are taken from Gandia, Gandarias *et al.* [64] and Muela *et al.* [37].

From these results and taking into account that the product of the amplitude × the frequency should be below a certain safety limit ($H \times f \leq 5 \times 10^9$ A $m^{-1}$ $s^{-1}$) [103] for medical applications, a field amplitude of 31.8 kA $m^{-1}$ (400 Oe) was chosen for this study.

For the sake of comparison, Figure 2.1 also shows the SAR values of isolated magnetosomes dispersed in water. The SAR of isolated magnetosomes is clearly lower than that of whole bacteria, which presumes that bacteria are more efficient for heating in MHT. This difference has been attributed to the spatial configuration of the nanoparticles that are aggregated in the case of isolated magnetosomes and maintain the chain configuration when whole bacteria are used, which has been proven as an important feature for heating efficiency [64, 65, 101].

Despite these promising results, in order to use MTB for cancer treatment their cytotoxicity and performance in hyperthermia treatment with cancer cells has to be tested. For this purpose, in this work an *in vitro* experiment in which MSR-1 were put in contact with A549 lung carcinoma cells is presented. A scheme of the experiment performed is shown in Figure 2.2.

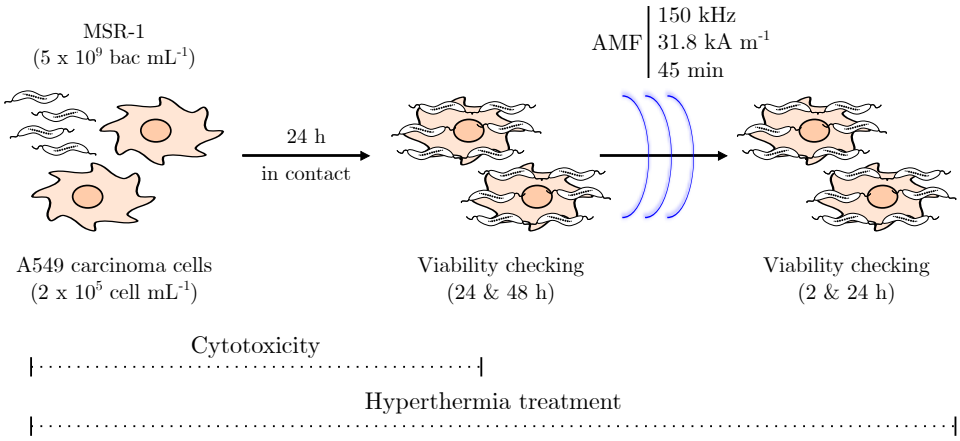


Figure 2.2: Scheme of *in vitro* assay carried out to determine the potential cytotoxicity of MTB and the effect of magnetic hyperthermia in cancer cells.

MSR-1 were fixed with glutaraldehyde before put in contact with A549 cells, which provided them with green fluorescence [104]. Therefore, this could be used as a tool to verify by flow cytometry that cells had indeed loaded MSR-1. As it is shown in Figure 2.3, the green fluorescence intensity in MSR-1-loaded cells is higher than in control cells. This shift is due to the presence of MSR-1 inside or adhered to cells.

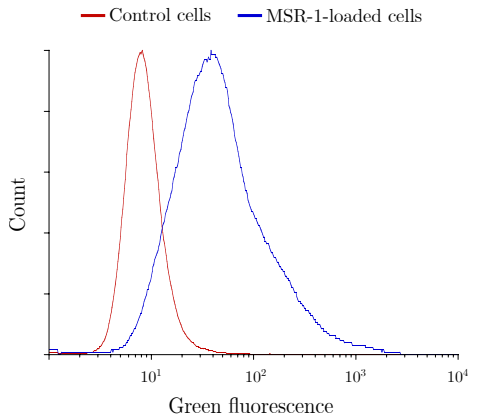


Figure 2.3: Fluorescence histogram obtained by flow cytometry showing the profile of control cells and MSR-1-loaded cells. The shift can be used to verify the loading of cells as they show fluorescence due to the presence of fluorescent MSR-1.

The MSR-1 uptake was also confirmed by magnetic measurements. The hysteresis loops of MSR-1-loaded cells along with those of individual bacteria, allowed a quantitative estimation of magnetite incorporated into A549 cells (see Materials and Methods). The actual mass of magnetite incorporated into the cells after 24 h of incubation was of around 8 - 10 pg per cell, which is $\sim$5% of what was initially added to the cell culture.

### 2.1.1 Cytotoxicity

To determine the potential cytotoxic effects that MSR-1 may cause in cancer cells, viability was checked after 24 and 48 h of MSR-1 uptake (Figure 2.2). Cell viability was measured by flow cytometry and Hoechst 33342/propidium iodide staining to discriminate between living and dead cells. Hoechst is a blue fluorescent membrane-permeable dye that links to DNA staining cell nuclei and allowing the differentiation of cells from other possible artifacts. Propidium iodide (PI) is a red fluorescent stain that also links to DNA but only when the cell membrane is damaged indicating that those cells are no longer alive. The viability percentage was calculated as the ratio between the number of living cells and the total number of cells. The results of a representative experiment after 24 h of incubation are shown in Figure 2.4. The percentage of dead cells in both control cells and MSR-1-loaded cells was similar, suggesting that

MSR-1 did not cause cytotoxicity in A549 cells.

Combining the results of three different experiments, it is observed that cell viability is not affected by MSR-1 as it remains above 88% 48 h after bacterial uptake, similar to that of control cells (Table 2.1).

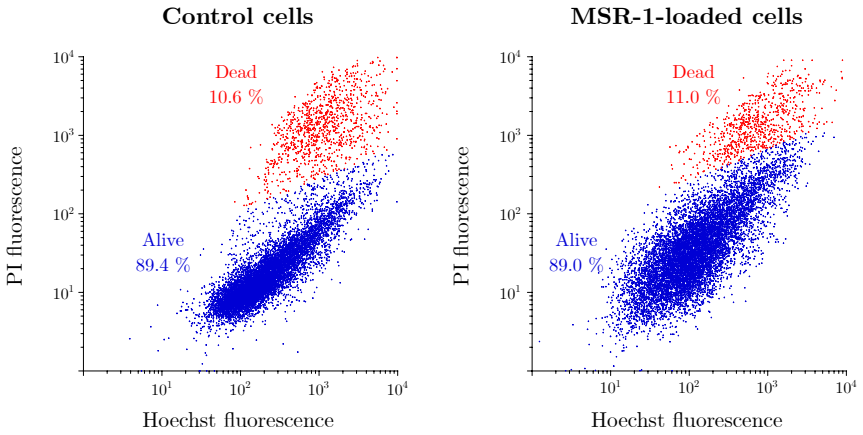


Figure 2.4: Fluorescence dot plots of Hoechst/propidium iodide (PI) stained cells obtained by flow cytometry in a representative experiment. Control cells and MSR-1-loaded cells after 24 h of incubation are displayed.

| **Viability** | | |
|---|---|---|
| | Control cells | MSR-1-loaded cells |
| 24 h | 88.3 ± 1.1% | 88.7 ± 0.2% |
| 48 h | 88.9 ± 1.0% | 90.6 ± 1.5% |

Table 2.1: Viability percentages after 24 and 48 h of culturing MSR-1-loaded cells and control cells. The results represent the mean ± standard deviation values, n = 3.

Moreover, the presence of MSR-1 within cancer cells did not affect their ability to grow. The evolution of living cells over time is observed in Figure 2.5. Both cell cultures, with and without bacterial load, show the same pattern and no significant differences are found in the number of living cells after 48 h of MSR-1 uptake.

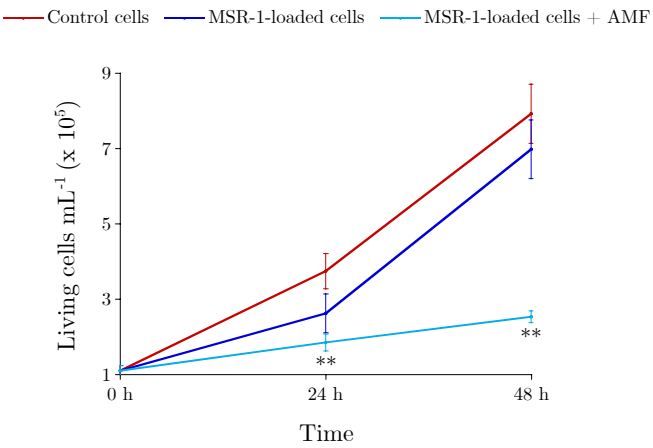


Figure 2.5: Time evolution of the number of living A549 cells. Data represent the mean ± standard deviation, n = 3. **, $P < 0.01$.

Different results were reported in previous experiments performed with isolated magnetosomes from MSR-1, which caused cytotoxicity to cells affecting both their viability and proliferation [37]. The magnetite amount caught by cells was similar in both studies (around 5 - 7 pg per cell in the case of magnetosomes and 8 - 10 pg per cell for MSR-1) but different cell types were used. Therefore, the different results could be explained as the cellular model used in the previous study, ANA-1 murin macrophages, may present higher sensibility than A549 cells to the byproducts generated in magnetosome metabolism. However, it may also be due to the fact that when using whole bacteria, magnetosomes are embedded in a thick organic envelope (the bacterial body), which could prevent the formation of big magnetosome clusters avoiding cytotoxicity.

### 2.1.2 Magnetic hyperthermia

For the hyperthermia treatment, MSR-1-loaded cells were exposed to an AMF of 31.8 kA $m^{-1}$ and a frequency 150 kHz for 45 minutes (Figure 2.2). A deleterious effect is observed immediately after AMF application. The results of a representative experiment are shown in Figure 2.6, which displays the propidium iodide fluorescence histograms of MSR-1-loaded cells before and after AMF application. Before AMF application more than 92% of cells showed low red fluorescence intensity, corresponding to the cells that exclude propidium

iodide or living cells. However, after AMF application the red fluorescence histograms showed a bimodal distribution with a second peak in the region of high propidium iodide fluorescence level or dead cells.

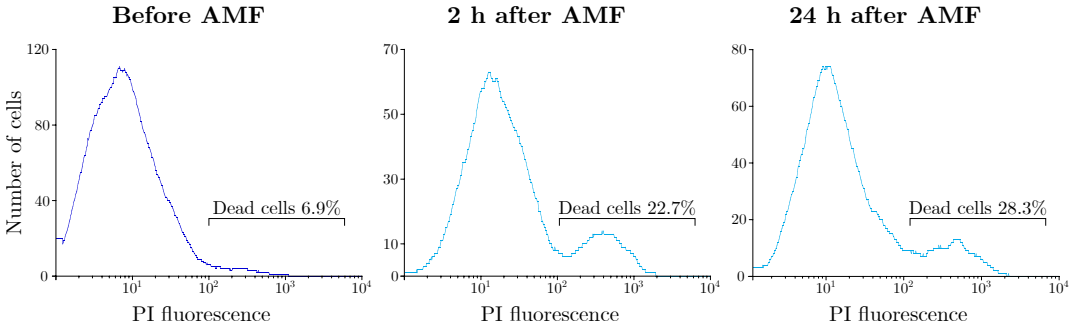


Figure 2.6: Fluorescence histograms of A549 cells stained with propidium iodide (PI) obtained by flow cytometry. The displayed results represent MSR-1-loaded cells before, after 2 h and after 24 h of AMF application.

Considering the results of three different experiments, cell viability after 24 h exposure to the AMF in MSR-1-loaded cells decreased ∼25% (Table 2.2). On the contrary, the AMF did not cause any decrease in the viability of control cells as it remained above 89% (Table 2.2), which is critical if this treatment is to be used *in vivo*.

| **Viability** | | |
|---|---|---|
| | Control cells | MSR-1-loaded cells |
| Before AMF | 92.7 ± 1.5% | 91.4 ± 0.7% |
| 2 h after AMF | 90.1 ± 2.2% | 73.7 ± 3.2% |
| 24 h after AMF | 89.4 ± 4.7% | 76.1 ± 5.3% |

Table 2.2: Viability percentages of A549 cells before and after AMF application. The results displayed represent the mean ± standard deviation values, n = 3.

Cell proliferation was also strongly affected for MSR-1-loaded cells after AMF application (Figure 2.5). The growth of the cultures undergoing hyperthermia slowed down and at the end of the experiment, the number of living A549 cells was three times lower than the control.

Other studies have been carried out to test the efficiency of MTB in hyperthermia treatment. Chen *et al.* [100] showed the effective inhibition of neurob-

lastoma in mice after magnetic hyperthermia mediated by *Magnetospirillum magneticum* AMB-1. They applied an AMF of 16 kA $m^{-1}$ and 518 kHz for 30 minutes. Alphandéry *et al.* [66] also tested AMB-1 in MHT to treat breast cancer in mice. For this, they injected $10^8$ bacteria intratumoraly and applied an AMF of 31.8 kA $m^{-1}$ and 183 kHz for 20 minutes three times. However, they reported no antitumor activity. These results were attributed to the low temperature increase reached due to the low density of magnetic material injected that did not yield sufficient heating efficiency with the tested parameters. In another study, Chen *et al.* [67] proved the efficacy of MHT with *Magnetococcus massalia* MO-1 to kill *Staphylococcus aureus* (a pathogen that causes skin and soft tissue infections). They applied an AMF of 6.9 kA $m^{-1}$ and 80 kHz for 1 h to both cultures of *S. aureus* and to mice with wounds infected with *S. aureus*. They reported that MO-1 mediated MHT was able to kill ∼50% of *S. aureus* (*in vitro*) and that it immensely promoted wound healing (*in vivo*).

The results of the present study along with the aforementioned performed by other authors, show a promising future for the use of whole magnetotactic bacteria as an alternative to magnetosomes for magnetic hyperthermia treatments. Not only whole magnetotactic bacteria are more efficient as MHT agents than isolated magnetosomes, but they have another main advantage that is bypassing the tedious and costly process of magnetosome extraction and purification.

## 2.2 Conclusions

From the results discussed in this chapter it can be concluded that:

- *Magnetospirillum gryphiswaldense* does not cause cytotoxicity on cancer cells in terms of viability and proliferation.
- *M. gryphiswaldense* bacteria are promising agents in magnetic hyperthermia as the treatment significantly affects viability and proliferation ability of cancer cells.

# Chapter 3

# Long-term tracking of magnetosomes in eukaryotic cells

If magnetic nanoparticles are to be used in biomedicine, it is essential to understand their long-term fate inside the body. On the one hand, this is important to establish the time after injection when they are still intact and, therefore, can perform their function efficiently. On the other hand, it is crucial to understand their degradability and clearance mechanisms to detect if the products formed in consequence provoke any sort of cytotoxicity.

Several studies mostly performed in mice have evidenced the *in vivo* accumulation and fate of magnetic nanoparticles. After injection, nanoparticles are predominantly accumulated in tissue-resident macrophages of liver, spleen, and kidney where they are stored in phagosomes that fuse with lysosomes for degradation [105–108]. For instance, Nan *et al.* [54] performed an *in vivo* MRI-based study where they examined the distribution and clearance of magnetosomes injected intravenously into mice. They reported that magnetosomes accumulated mostly in the liver and spleen and that their clearance rate was dose dependent. The disappearance of MRI signal took up to 4 months for the liver and 3 months for the spleen when the injected dosage was of 32 mg of magnetosomes per kg.

Despite the clinical relevance of *in vivo* studies, they do not provide information about the intracellular fate of nanoparticles. It has been proposed that independent of the endocytic pathway cells use to internalize nanoparticles, they end up being stored in early endosomes [76]. Here, the cargo may be sent back to cell surface and excreted to the surrounding environment or found in late endosomes that fuse with lysosomes [76]. Due to the low pH environment of lysosomes and the presence of hydrolytic enzymes and other biomolecules, iron oxide nanoparticles like magnetosomes may degrade resulting in the release of free iron [109]. It has been suggested that the iron released from magnetite degradation loads ferritin [110–112], a protein that stores iron in the mineral form of ferrihydrite protecting cells from the potential toxic effects of free iron [113, 114].

The aim of this chapter is to follow the long-term intracellular fate of magnetosomes. For this, two cell models have been tested: A549 human lung carcinoma cells and RAW 264.7 murine macrophages. Understanding the degradation process in cancer cells is essential to know for how long magnetosomes will be effective in future treatments, for instance, in magnetic hyperthermia. Macrophages were selected because they are innate immune system cells responsible for the uptake and degradation of foreign agents, such as nanoparticles. Moreover, they play a key role in iron homeostasis [115, 116]. Finally, the results of cellular experiments were compared with magnetosome degradation in an *ex cellulo* model that mimics the acidic pH environment of lysosomes.

## 3.1 Experimental design

Figure 3.1 shows the experimental design used to study the fate of magnetosomes inside cells. A549 and RAW 264.7 cells were put in contact with magnetosomes for 2 hours after which the culture medium was replaced for fresh medium in order to remove magnetosomes that were not attached to or inside cells. Cell cultures were maintained up to 20 days for A549 and up to 13 days for RAW 264.7 cells. This difference in the incubation time was due to the faster growing rate of RAW 264.7 cells as will be shown next. In order to maintain the whole cell population in healthy and growth promoting conditions, before confluence was achieved in the culture recipient, cells were detached and transferred to larger culture flasks with up to 500 $cm^2$ surface.

At certain time points cells were fixed and the supernatant removed to perform several measurements. Flow cytometry was used to determine cell growth and to visualize changes in the side scatter profile of cells. Inductively coupled plasma (ICP) analysis was performed to measure the changes in the total amount of intracellular iron. TEM images were taken to see the variations in the size and morphology of magnetosome clusters inside cellular endosomes. SQUID magnetometry measurements were performed to check the progression of magnetization. Lastly, X-ray absorption near edge spectroscopy (XANES) measurements at the Fe K-edge were carried out to observe the structural and electronic changes of Fe atoms and identify the Fe species that occur in a degradation process.

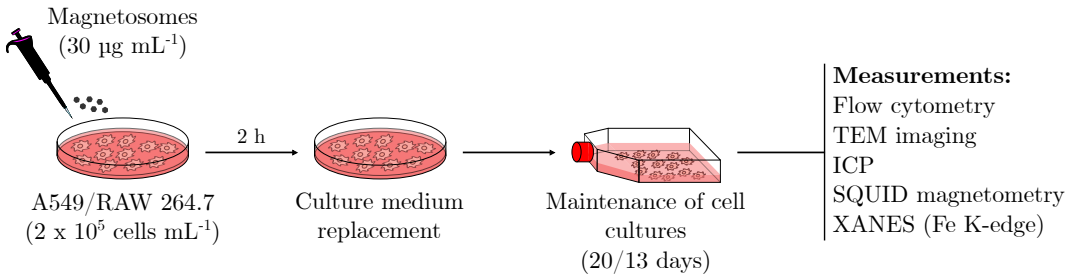


Figure 3.1: Scheme of the experiment carried out to determine the long-term fate of magnetosomes in A549 and RAW 264.7 cells.

## 3.2 First approaches to elucidate intracellular magnetosome fate

Intracellular magnetosome fate was first analyzed by looking into cells side scattered light evolution along time, measured by flow cytometry. Magnetosome-loaded cells show higher side scatter values than unloaded cells, as explained in *Chapter 1*. Figure 3.2 shows the progression of side scatter in A549 and RAW 264.7 cells, together with unloaded cells. In both cases the side scatter shows a maximum after 2 hours of magnetosome uptake and decreases towards values similar to that of unloaded cells with time. The decrease in side scatter could be due to three reasons. Firstly, if cell population grows over time, the magnetosome content may divide into daughter cells, meaning that each cell may have a smaller magnetosome content. Secondly, cells may be excreting

magnetosomes to the surrounding environment. Thirdly, if magnetosomes are degrading, their individual and cluster size may decrease.

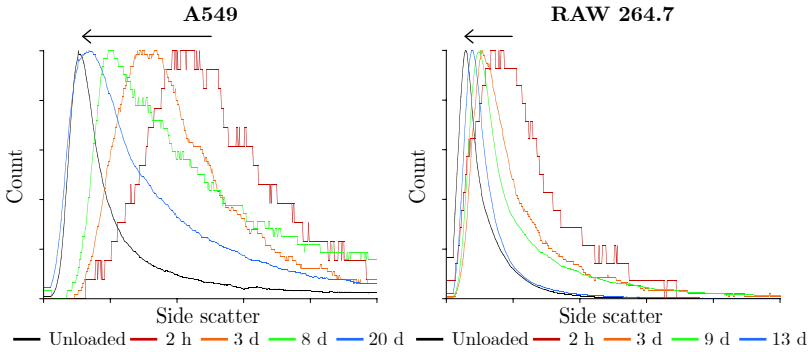


Figure 3.2: Histograms representing the side scatter progression as a function of time in A549 and RAW 264.7 cells.

In order to visualize magnetosomes inside cells during the experiment, TEM images of cell slides were taken at different time points. RAW 264.7 cells were taken as a model for this experiment. Figure 3.3 shows an example of images of RAW 264.7 macrophages obtained 2 h, 8 days and 13 days after magnetosome uptake. It can be observed that after 2 h magnetosomes are both attached to the cell surface and in the interior forming clusters. This was previously seen in *Chapter 1* for A549 cells. Magnetosome clusters decrease in size and number over time but 13 days after internalization some magnetosomes are still seen clustered in endosome-like vesicles. This confirms the decrease of magnetosome content per cell because either magnetosomes are being split into daughter cells, excreted and/or degraded.

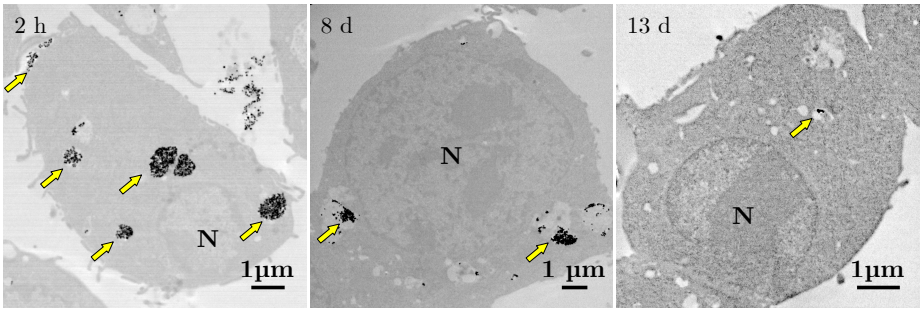


Figure 3.3: TEM images of RAW 264.7 cells 2 h, 8 days, and 13 days after magnetosome uptake. Pink arrows point magnetosome clusters and cellular nuclei are marked N.

Cell population growth was monitored by flow cytometry. It was confirmed to be exponential during the experiment for both cell types (Figure 3.4). Cell population growth rate was faster in RAW 264.7 than in A549 cells; the duplication time was estimated as 1.25 days for RAW 264.7 versus 3 days for A549 cells. These results support that magnetosomes could split into daughter cells as they proliferate.

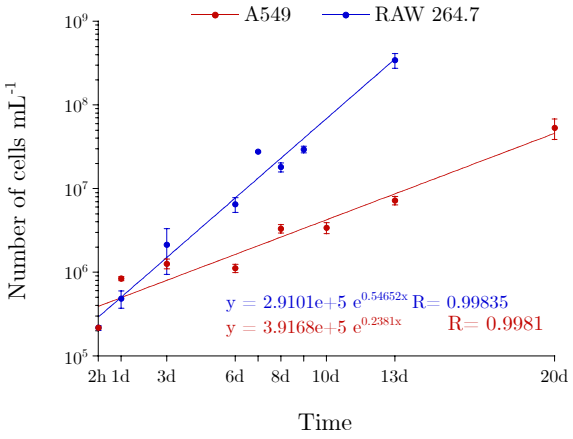


Figure 3.4: Progression of the number of cells as a function of time for A549 and RAW 264.7 cells. Data represent the mean ± standard deviation, n = 3. The line is an exponential fit to the data.

ICP analysis was performed to determine the progression of the total iron mass of the cell populations. As observed in Figure 3.5, the total iron mass decreases in both cell types, ∼50% in A549 cells after 20 days and ∼80% in RAW 264.7 cells after 13 days of magnetosome uptake. These results indicate that iron is being excreted from cells to the surrounding environment. Nonetheless, it is not possible to determine whether the released iron is in the form of intact magnetosomes or forming other iron species resulting from a possible magnetosome degradation.

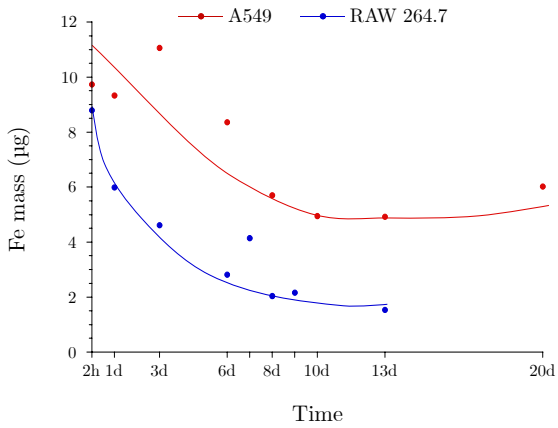


Figure 3.5: Total iron mass measured by ICP of the whole cell population of A549 and RAW 264.7 along time after magnetosome uptake. The lines represent a guide for the eye.

## 3.3 Progression of magnetic response

The magnetic properties of the whole cell population were measured over time by SQUID magnetometry. Figure 3.6 shows the hysteresis loops of the two cell types as a function of time. Assuming that at 2 h the magnetosomes are still intact, and that the saturation magnetic moment, $m_s$, should derive entirely from magnetite (92 A $m^2$ $kg^{-1}$), the initial mass of magnetite per cell was of 64 ± 15 pg in A549 and of 55 ± 12 pg in RAW 264.7 cells. Over time, $m_s$ decreases indicating that there is less magnetite in the sample because either magnetosomes are being transformed into a less or non magnetic product, and/or because they (or the resulting products) are being excreted from the cells.

Figure 3.7 shows the ratio between the saturation magnetic moment at a certain time point, $m_s(t)$, and after 2 h from magnetosome uptake by cells, $m_s(2h)$. The decrease in $m_s$ was faster in RAW 264.7 macrophages as after 3 days of magnetosome uptake there was a decrease of 40% compared with the 15% in A549 cells. Moreover, after 13 days, $m_s$ of RAW 264.7 cells decreased by 80% in comparison with the 70% decrease observed in A549 cells after 20 days. This suggests that magnetosomes are more easily degraded and/or excreted in RAW 264.7 than in A549 cells.

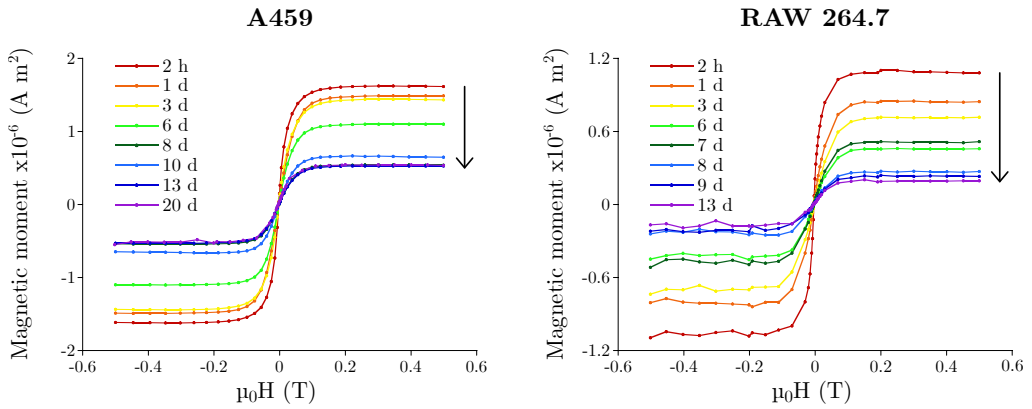


Figure 3.6: Hysteresis loops of A549 and RAW 264.7 cell populations along time.

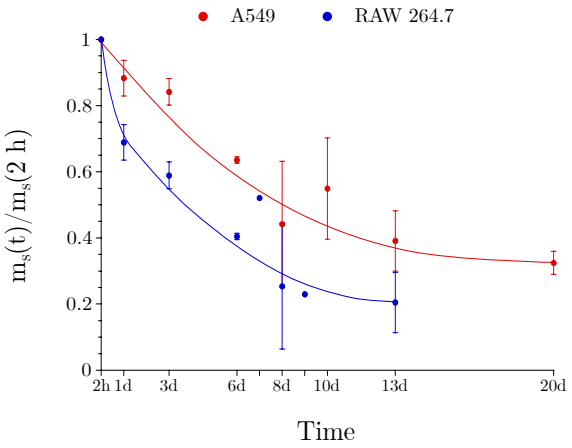


Figure 3.7: Ratio between the saturation magnetic moment values at a certain time point, $m_s(t)$, and after 2 h of magnetosome uptake, $m_s(2\ h)$. Data represent the mean ± standard deviation, n = 3. The line represents a guide for the eye.

Curcio *et al.* [117] reported a similar trend when working with magnetosomes extracted from *Magnetospirillum magneticum* AMB-1 and human endothelial cells (HUVECs). The $m_s$ of cells decreased 62% after 9 days of cell culture, which is similar to the result observed in the present work after 13 days of magnetosome uptake in A549 cells and between 7 and 8 days after magnetosome uptake for RAW 264.7 cells.

However, in the same study by Curcio *et al.* [117] they observed a different result when working with mesenchymal stem cells. Although they reported a decrease of $m_s$ after 3 days of culture, from day 3 until day 21 they observed an increase of $m_s$ to initial values, a phenomenon that they termed "remagnetization". A similar trend was reported by the same group in a previous paper by Van de Walle *et al.* [118] working with mesenchymal stem cells and chemically synthesized iron oxide nanoparticles of 8 nm diameter. They attributed this phenomenon to the synthesis of magnetic nanoparticles by cells using the free iron released from the initial magnetosome degradation. They suggested that the fact that no remagnetization was observed when working with HUVEC cells could be due to this phenomenon being stem cell specific.

## 3.4 Identification of the iron species involved in magnetosome degradation

Aiming to identify the products of a possible magnetosome degradation, X-ray absorption spectroscopy at the Fe K-edge (7112 eV) was used. This technique allows for the specific analysis of a particular element in the sample by adjusting the energy range around its characteristic absorption threshold. The X-ray absorption near-edge structure (XANES) region of the spectrum was analyzed, which goes from 15 - 20 eV below the edge up to 100 - 150 eV above the edge. The XANES region provides electronic and structural information around the absorbing element, Fe in this case [119].

Figure 3.8 shows the XANES spectra of A549 and RAW 264.7 cells at several time points after magnetosome uptake. Three regions of interest can be distinguished in the XANES spectra:

- The pre-edge peak appears 15 - 20 eV before the main (K-edge) absorbing edge and it is usually related to the symmetry of the absorbing element. As shown in the inset of Figure 3.8, no significant changes are observed in this region.

- The edge position is a fingerprint of the oxidation state of the absorbing atom. As shown in Figure 3.8, the edge position shifts towards higher

energies over time, indicating that there is a change in the oxidation state of Fe.

- The post-edge region gives information of the medium-range order around the absorbing atom. As observed in Figure 3.8, there are changes at the white line (the maximum absorption just after the edge, at ∼7130 eV) and the shoulder at ∼7138 eV indicating that the surroundings of the Fe atoms change over time.

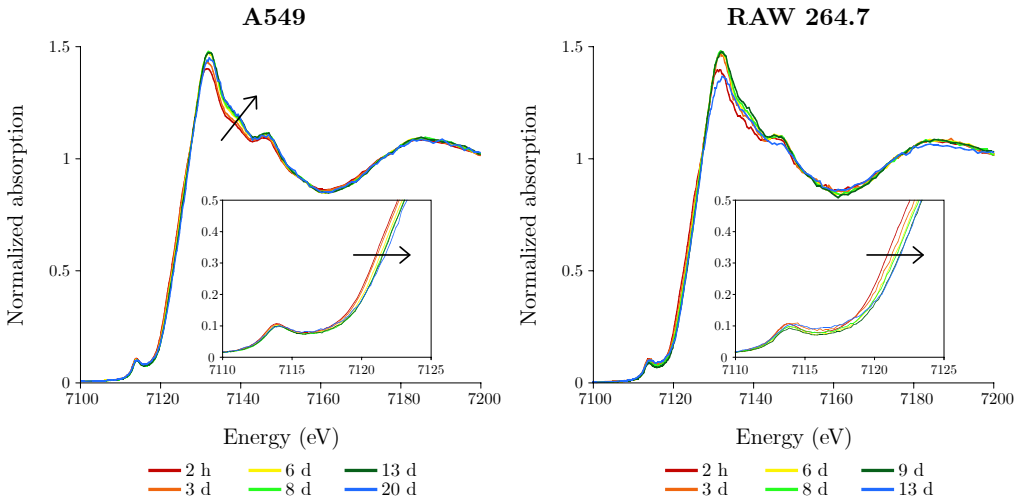


Figure 3.8: Fe K-edge XANES spectra of A549 and RAW 264.7 cells measured at different time points after magnetosome uptake.

The changes observed in the XANES spectra suggest an intracellular degradation process of magnetosomes. As a preliminary analysis of this process, the spectra of the initial and final time points measured in this study (2 h and 20 days for A549 and 9 days after magnetosome uptake for RAW 264.7 cells) are compared with reference spectra in Figure 3.9. Note that although the final time point measured for RAW 264.7 cells was after 13 days of magnetosome uptake, this spectrum deviates from the general trend and will be further explained later. For the reference spectra two iron compounds with different oxidation state are represented: inorganic magnetite ($Fe_3O_4$) and ferrihydrite, the ferric oxy-hydroxide mineral in the core of ferritin, the protein involved in the storage of iron in cells [114]. In this case, horse spleen ferritin (HoSF) is used as the ferrihydrite reference. The spectrum of isolated magnetosomes is also included for comparison.

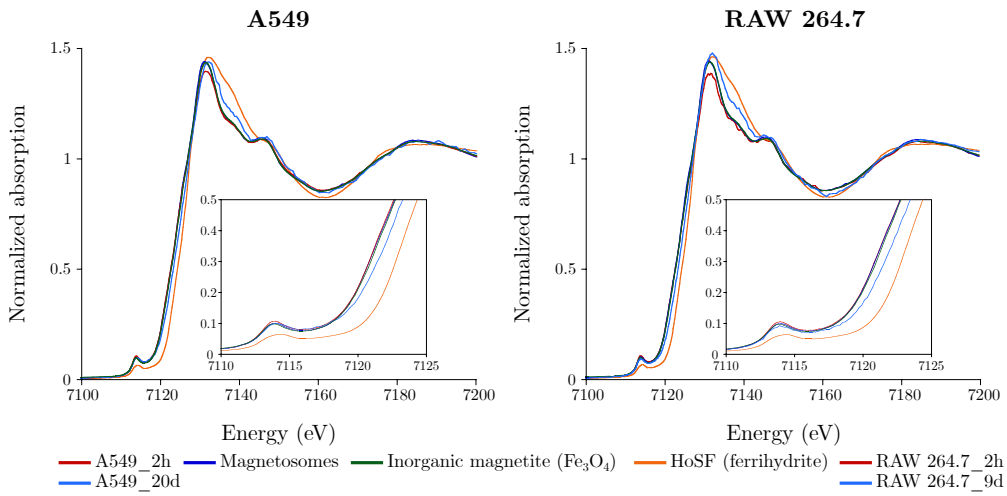


Figure 3.9: Fe K-edge XANES spectra of magnetosomes, inorganic magnetite ($Fe_3O_4$) and ferrihydrite from HoSF with A549 2 h and 20 days after magnetosome uptake and RAW 264.7 2 h and 9 days after magnetosome uptake.

The XANES spectra of A549 and RAW 264.7 2 h after magnetosome uptake are similar to the XANES spectra of magnetosomes and inorganic magnetite, which are coincident. The edge position of these spectra corresponds to a mixed oxidation state of Fe with a $Fe^{2+}$:$Fe^{3+}$ ratio of 1:2, as in magnetite. These results confirm that magnetosomes are formed of magnetite crystals and that they remain mostly intact after 2 h of interaction with cells. The edge position of the final spectra, 20 days for A549 and 9 days after magnetosome uptake for RAW 264.7 cells, are displaced towards ferrihydrite but are not coincident with it. The edge position of ferrihydrite, a pure $Fe^{3+}$ compound, is shifted +1.58 eV with respect to magnetite. This shift is larger than the one observed in cell samples (+0.55 eV for A549 and +0.92 eV for RAW 264.7 cells). This indicates that magnetosomes are not yet fully oxidized at the last time point examined. The larger shift observed for RAW 264.7 compared to A549 cells, even in a shorter time period, could imply that they are more effective at oxidizing magnetosomes.

To identify the iron phases occurring during the degradation process, a linear combination fitting of XANES spectra by using reference compounds was performed at each time point after magnetosome uptake. In addition to the spectrum for magnetosomes (magnetite), which indicates the starting point, and HoSF (ferrihydrite), other references were tested: maghemite ($\gamma$-$Fe_2O_3$),

goethite ($\alpha$-FeO(OH)), and hematite ($\alpha$-$Fe_2O_3$). However, after several trials three references were needed for the best fitting: magnetosomes (magnetite), maghemite, and HoSF (ferrihydrite) or goethite. An example of a linear combination fitting of A549 and RAW 264.7 cells 8 days after magnetosome uptake is observed in Figure 3.10 (top). The linear combination fittings of all measured spectra are also represented along with the experimental data (Figure 3.10, bottom).

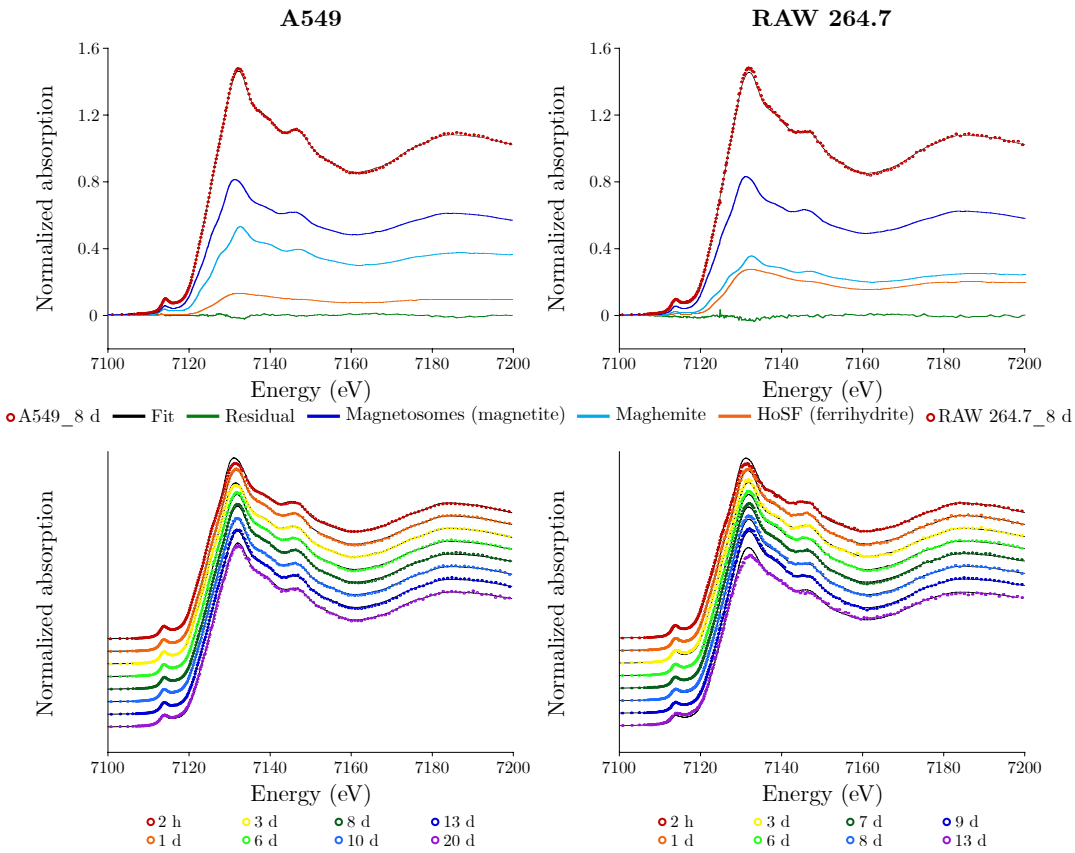


Figure 3.10: Top: example of the linear combination fitting of A549 and RAW 264.7 cells XANES spectra 8 days after magnetosome uptake along with the references used for the fitting. Bottom: linear combination fits of all the time points measured.

The weight of each reference compound in the linear combination fitting represents the atomic fraction of iron in each phase. This is shown in Figure 3.11. The degradation process follows a similar trend in both cell types. During the first 3 days, there is an oxidation of magnetite to maghemite. Once

a certain atomic fraction of iron in maghemite is reached, ferrihydrite starts to appear on day 6.

The appearance of ferrihydrite supports previous works that suggest that iron released from degrading magnetite nanoparticles could be locally transferred to endogenous ferritins through a process regulated by iron homeostasis [120]. Ferritin has a protective role, as it appears to temporarily chelate labile iron that is redox-active, reducing its concentration and therefore the sensitivity of lysosomes and cells to oxidative stress [121, 122].

There is a main difference in the efficiency of both cell types in degrading magnetosomes. RAW 264.7 are more efficient than A549 cells as after 9 days of culture only 45% of the iron remains in the form of magnetite, compared to the 62% remaining in A549 after 10 days. Furthermore, RAW 264.7 are also more efficient in transforming the iron into ferrihydrite as after 9 days they contain 30% of the iron in this form, compared to A549 cells that only contain 4% of the iron in ferrihydrite form after 10 days and 15% after 20 days. The difference in iron degradation between the two cell types can be explained as RAW 264.7 cells are macrophages meaning that their function inside the body is to capture and degrade foreign debris whereas A549 cells are endothelial cells with no specific function of degradation. Moreover, macrophages play a key role in iron metabolism as they are involved in iron scavenging, recycling and storage in the body [115, 116]. They are involved in the recycling of senescent red blood cells and, under infection, they sequester extracellular iron, an action that can limit the growth and pathogenicity of invading microbes [123].

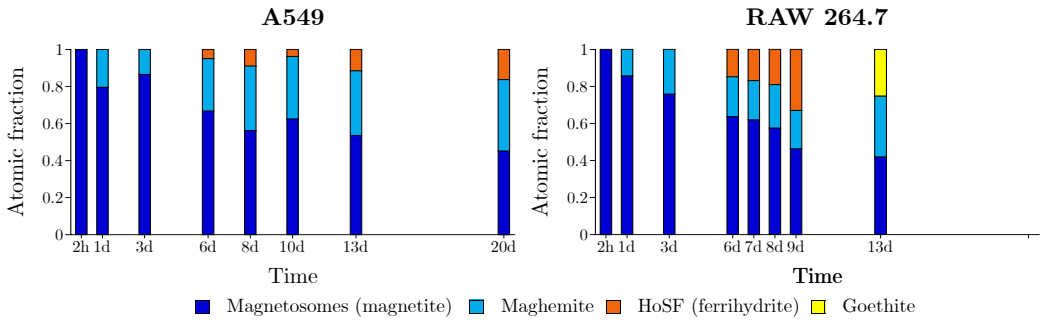


Figure 3.11: Atomic fraction of Fe in the four phases (magnetosomes (magnetite), maghemite, HoSF (ferrihydrite), and goethite) obtained from the linear combination fits of Fe K-edge XANES spectra of A549 and RAW 264.7 cells as a function of time after magnetosome uptake.

As mentioned previously, the spectrum of RAW 264.7 after 13 days of magnetosome uptake does not follow the pattern of other time points measured. For this sample the best fit was achieved with magnetosomes, maghemite and goethite (Figure 3.10, bottom, right). Goethite is an iron oxy-hydroxyde ($\alpha$-FeO(OH)) similar to the iron mineral phase of hemosiderin [124, 125]. Hemosiderin is the lysosomal degradation product of ferritin that appears under conditions of iron overload [126]. Therefore, the appearance of goethite after 13 days of magnetosome degradation could be due to the degradation of ferritin to yield hemosiderin as a consequence of an iron excess situation in the cells.

Finally, as a sign of consistency of the results, the total mass of iron obtained from ICP (Figure 3.5) was compared to the values estimated from the combination of the atomic fraction of iron in each phase obtained from XANES and the saturation magnetic moment ($m_s$) of the hysteresis loops (Figures 3.6 and 3.11). This calculation is based on the fact that magnetite and maghemite are ferrimagnetic materials and contribute to $m_s$, whereas ferrihydrite, being antiferromagnetic, does not contribute [127]. The details of the calculation can be found in the Materials and Methods section. The results along with the total mass of iron obtained by ICP are represented in Figure 3.12. Despite some differences in the values obtained by both independent techniques, the similar overall progression of the iron content resulting from both measurements confirms the goodness of the results.

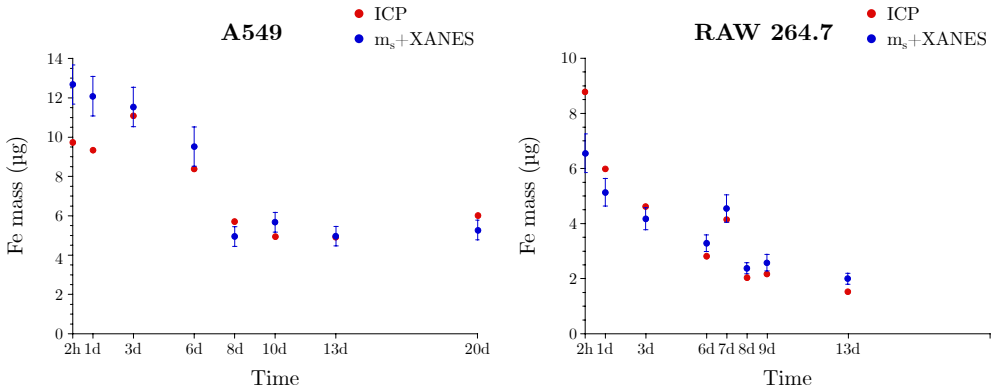


Figure 3.12: Mass of iron obtained by ICP and estimated by the combination of the atomic fraction of Fe in each phase obtained from XANES and the saturation magnetic moment, $m_s$, of the hysteresis loops.

### 3.4.1 Magnetosome degradation *ex cellulo*

As shown in *Chapter 1*, magnetosomes enter cells mainly by phagocytosis or macropinocytosis. Then, magnetosomes are incorporated into endosomes that may fuse with lysosomes starting a degradation process [76]. Lysosomes are cell organelles with acidic pH 4.5 - 5 that contain a mixture of enzymes and other biomolecules responsible for the digestion of external debris [128].

In order to better understand intracellular magnetosome degradation, one of the factors present in the lysosomal environment was simulated *ex cellulo*, acidic pH. For this, 50 µg $mL^{-1}$ magnetosomes were incubated at 37 °C in 20 mM citrate buffer pH 4.5 up to 32 days (see Materials and Methods). Although this medium does not fully represent lysosomal environment because it lacks the enzymes and biomolecules involved in the iron metabolism, it allows to evaluate the role of an important parameter, namely the pH, on the degradation of magnetosomes.

Figure 3.13 shows the Fe K-edge XANES spectra of magnetosomes maintained at pH 4.5 for 32 days. Similarly to what happened in cells, there is a shift of the absorption edge towards higher energies after 32 days indicating that magnetosomes are being oxidized.

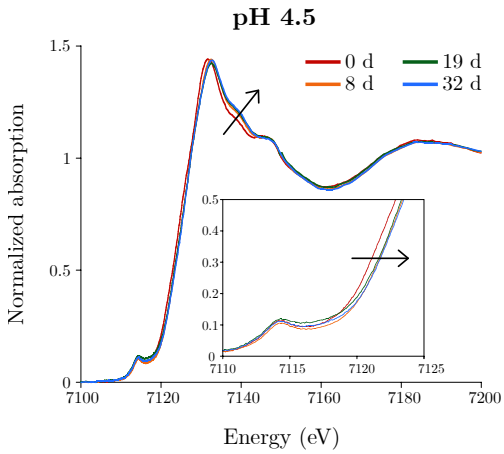


Figure 3.13: Fe K-edge XANES spectra of magnetosomes maintained at pH 4.5 in citrate buffer and 37 °C for different times.

In order to identify the iron phases occurring during the process, linear combination fitting of the spectra was performed. For this, several references were tested: magnetosomes (magnetite), maghemite, HoSF (as a reference for inorganic ferrihydrite, as the local structure of the HoSF core is similar to that of inorganic ferrihydrite [119, 127]), goethite, hematite, and wüstite (FeO). As in the intracellular degradation process, the best fits were obtained with magnetosomes, maghemite, and HoSF. The results of the linear combination fitting along with the experimental data are observed in Figure 3.14.

The atomic fraction of iron in each phase is represented in Figure 3.14. These results confirm that in an acidic pH similar to that of the lysosomes, magnetite is progressively degraded into maghemite and ferrihydrite. However, the degradation rate is slower *ex cellulo* as at pH 4.5 the atomic fraction of iron in magnetite decreased to 41% after 32 days, which was similar to the values obtained in cells after 20 days in A549 and after 13 days in RAW 264.7. Therefore, even though lysosomal acidic environment is sufficient for magnetite degradation, these results further support that it is not the only factor involved and that enzymes and other biomolecules may also play an important role.

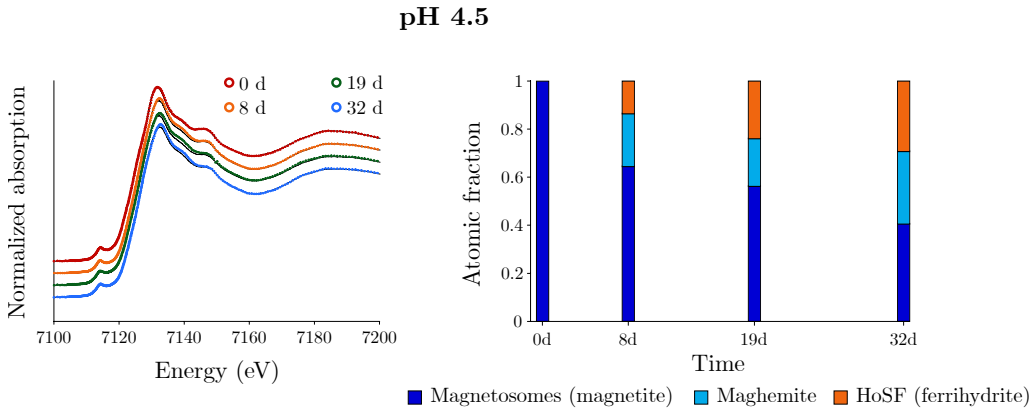


Figure 3.14: Left: linear combination fits of the Fe K-edge XANES spectra shown in Figure 3.13. Right: atomic fraction of Fe in the three phases (magnetite, maghemite, and ferrihydrite) obtained from the linear combination fits of the spectra.

## 3.5 Conclusions

From this chapter several conclusions can be inferred:

- The long-term fate of magnetosomes inside cells depends on three factors: splitting into daughter cells during cell division, excretion of iron to the surrounding environment, and intracellular degradation.
- Magnetosomes undergo intracellular degradation yielding maghemite, ferrihydrite, and goethite. The appearance of ferrihydrite and goethite suggests that cells use the magnetosome degradation products to load ferritin and hemosiderin, respectively.
- The permanence of magnetosomes inside cells is cell-dependent: clearance efficacy of pulmonary epithelial cells is reduced compared to that of macrophages.

# Chapter 4

# Modification of magnetotactic bacteria with rare earth elements

Tuning the characteristics of magnetosomes and MTB can lead to new properties that could be advantageous for biomedical applications. Different approaches to modify magnetosomes and MTB have been proposed such as chemical modification or genetic engineering. One strategy is to modify the composition of magnetosomes by culturing the MTB in media containing specific metallic elements. Since 2008 when Staniland *et al.* [129] published the first controlled doping of magnetosomes *in vivo*, several groups including ours have been able to dope magnetosomes with transition elements [22, 35, 36, 130–134].

Rare earth doping of magnetite nanoparticles has been attracting considerable attention due to their applications in biomedicine, catalysis and solar cells [135, 136]. It has been shown that the substitution of $Fe^{3+}$ ions in magnetite nanoparticles with rare earth ions can improve their magnetic, electrical, and optical properties [135, 137].

Following this line, in the present work, the addition of two rare earth elements to MTB culture medium were tested: terbium (Tb) and gadolinium (Gd). Apart from possibly modifying the magnetic response of magnetosomes, these elements were chosen because they could provide additional properties

to magnetosomes and MTB. Tb has luminiscence properties which could be useful for monitoring magnetosomes and MTB [138,139]. Gd-doped iron oxide nanoparticles have been studied as contrast agents for MRI as they exhibit T1-T2 dual-model MRI contrast [140].

After setting the culture strategy, the magnetic, structural and morphological characteristics of modified MTB were studied. Photoluminiscence properties that Tb may confer to MTB and magnetosomes were also analyzed. Finally, the cytotoxicity of MTB grown in the presence of Tb or Gd was tested *in vitro*.

## 4.1 Setting bacterial growth conditions

In order to promote Tb and Gd incorporation, *M. gryphiswaldense* MSR-1 was grown in culture media supplemented with Tb/Gd, as has been proven successful when doping MTB with transition metals [22,35,36]. To determine the highest Tb/Gd concentration without harmful effects, sensitivity curves of MSR-1 against Tb/Gd concentration were performed. Figure 4.1 shows the sensitivity curves of MSR-1 to Tb(III)-quinate and Gd(III)-quinate. Bacterial growth measured as optical density ($OD_{600nm}$) is represented as a function of the concentration of $Tb^{3+}$/$Gd^{3+}$ added to the culture media.

The sensitivity curves obtained for both elements show a similar pattern: there is a threshold value of 125 µM above which the growth is significantly reduced and no growth is observed from 400 µM on. In the light of these results, to ensure bacterial growth the standard culture medium (FSM) was supplemented with 100 µM Tb(III)-quinate or Gd(III)-quinate. As FSM composition includes 100 µM Fe(III)-citrate, the ratio $Tb^{3+}$:$Fe^{3+}$ and $Gd^{3+}$:$Fe^{3+}$ was 1:1. No additional modifications in the growth conditions were made with respect to the standard ones for MSR-1. For writing purposes from now on MSR-1 cultured in presence of Tb(III)-quinate or Gd(III)-quinate will be named as Tb-MSR-1 and Gd-MSR-1, respectively. MSR-1 will refer to bacteria grown in standard conditions.

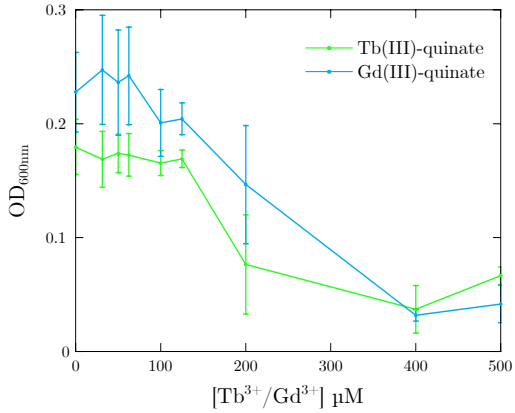


Figure 4.1: Sensitivity curves of MSR-1 to Tb(III)-quinate and Gd(III)-quinate. The results represent the mean ± standard deviation values, n = 8.

To verify the incorporation of Tb/Gd in MSR-1, ICP measurements were performed. The results indicate that both elements were present in the bacteria. The atomic percentages of Tb and Gd relative to the sum of Fe and each rare earth element were 6.7% and 8.5%, respectively. This confirms that the method chosen for Tb/Gd bacterial incorporation was successful.

## 4.2 Magnetic and structural characterization

### 4.2.1 Magnetic characterization

The magnetization of MSR-1 as a function of temperature was measured by means of zero field cooling/field cooling (ZFC/FC) magnetization curves (see Materials and Methods). From the ZFC/FC curves, the Verwey transition temperature, *Tv*, can be estimated, a structural transition characteristic of magnetite that is very sensitive to stoichiometric deviations [141–143]. *Tv* occurs at ∼120 K in bulk magnetite [144] and at a slightly lower temperature for magnetosomes [34, 145].

In Figure 4.2 the ZFC/FC curves of MSR-1, Tb-MSR-1 and Gd-MSR-1 are displayed and the *Tv* is marked with an arrow. MSR-1 has a *Tv* of 108 K. However, both Tb-MSR-1 and Gd-MSR-1 have a slightly lower *Tv*

(105 K). This decrease in *Tv* for Tb-MSR-1 and Gd-MSR-1 is more evident in the derivative of the ZFC curve shown in the inset of Figure 4.2. The peak of the derivative indicates the onset of the transition, which occurs at the same temperature for Tb-MSR-1/Gd-MSR-1. The Verwey transition is very sensitive to the stoichiometry and the fact that it shifts towards lower temperatures in Tb-MSR-1 and Gd-MSR-1 suggests that Tb and Gd have entered the magnetite structure. A similar decrease in *Tv* was previously observed in magnetosomes doped with manganese [35] and cobalt [36]. In addition, the incorporation of Tb and Gd change substantially the magnetic properties of the bacteria as detailed in Jefremovas *et al.* [146].

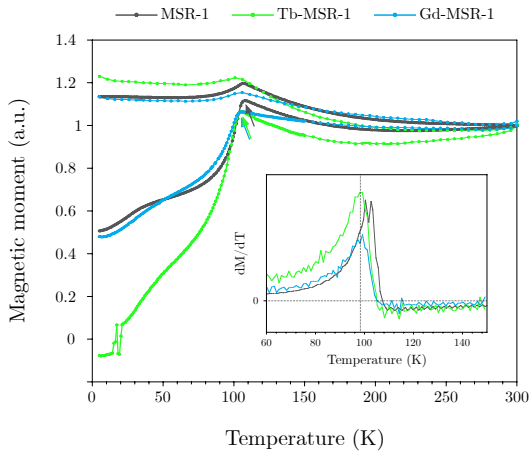


Figure 4.2: ZFC/FC curves measured at 5 mT for MSR-1, Tb-MSR-1 and Gd-MSR-1. The arrows point the Verwey transition temperature, *Tv*. Inset: derivative of ZFC for the three samples.

### 4.2.2 Structural characterization

XANES spectroscopy was used to further study the incorporation of Tb and Gd. Measurements were performed at the Fe K-edge and at the Tb/Gd-$L_3$ edges on both bacteria and the corresponding isolated magnetosomes. This allowed to verify if Tb/Gd were incorporated by MSR-1, and in that case, if they entered magnetosomes.

Figure 4.3 shows Tb/Gd-$L_3$ XANES spectra of Tb-MSR-1 and Gd-MSR-1 and corresponding isolated magnetosomes (Tb-mag and Gd-mag). The Tb/Gd

ions are in the +3 oxidation state both in the isolated magnetosomes and in the bacteria, as evidenced from the comparison of the edge energy with that of the $Tb^{3+}$ and $Gd^{3+}$ standards. However, the shape of the XANES signal is different between bacteria and isolated magnetosomes. Indeed, both for Tb and Gd the white line is more intense in the magnetosomes than in the bacteria, and the XANES oscillations after the white line do also differ between isolated magnetosomes and bacteria. This suggests that Tb and Gd atoms incorporated by the bacteria are not only in magnetosomes but can be also found in additional cellular compartments. Unfortunately, it has not been possible to identify the compounds they are forming by means of a combination fit to known standards.

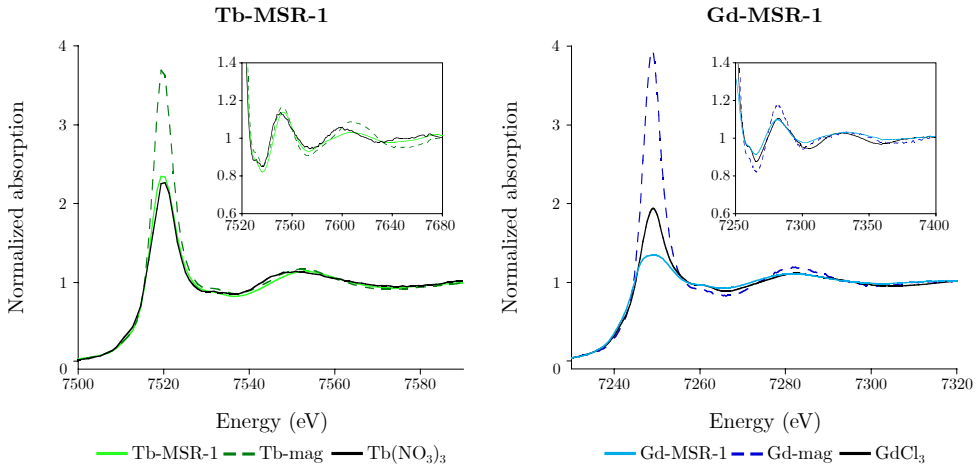


Figure 4.3: Tb $L_3$-edge (left) and Gd $L_3$-edge (right) XANES spectra of Tb-MSR-1 and Gd-MSR-1 and corresponding isolated magnetosomes (Tb-mag and Gd-mag). Spectra of corresponding standards for $Tb^{3+}$ ($Tb(NO_3)_3$) and $Gd^{3+}$ ($GdCl_3$) are displayed.

Figure 4.4 shows the Fe K-edge XANES spectra of isolated magnetosomes, Tb-mag and Gd-mag. The spectra are compared to isolated magnetosomes of MSR-1. The Fe K-edge spectra for both Tb-mag and Gd-mag are similar, and they qualitatively reproduce the spectrum of the magnetosomes isolated from MSR-1. However, there is a slight displacement of around -0.6 eV towards lower energies of the absorption edge of the Tb-mag and Gd-mag with respect to natural magnetosomes, that indicates that the average valence state of Fe is being reduced with respect to that of magnetite, where Fe holds a mixed valence $Fe^{2+}$:$Fe^{3+}$ of 1:2. Assuming that there is a linear relationship between

the displacement of the absorption edge and the oxidation state of the absorbing atom [119], this shift suggests that there is a substitution of approximately 3% of $Fe^{3+}$ ions by $Tb^{3+}$ or $Gd^{3+}$. These results support the incorporation of Tb and Gd into the magnetite structure of the magnetosomes, as suggested from the ZFC/FC measurements.

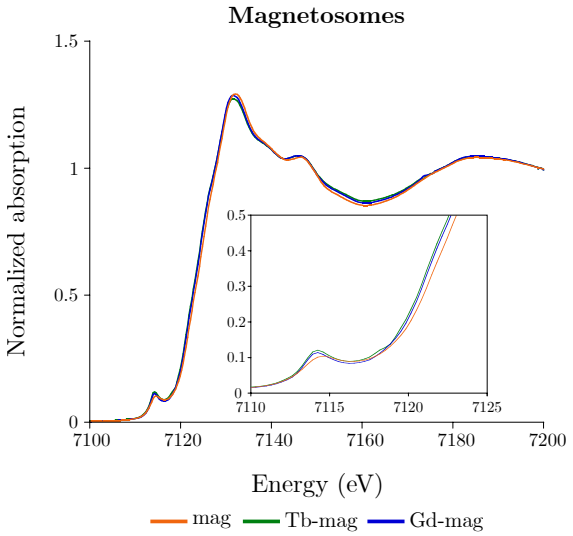


Figure 4.4: Fe K-edge XANES spectra of magnetosomes isolated from MSR-1 (mag), Tb-MSR-1 (Tb-mag) and Gd-MSR-1 (Gd-mag).

Figure 4.5 (A) shows Fe K-edge XANES spectra of MSR-1, Tb-MSR-1 and Gd-MSR-1 together with inorganic magnetite ($Fe_3O_4$) as a reference. In the case of MSR-1, as observed in previous works [22, 33], the spectrum is coincident to that of magnetite, because most of the Fe contained in the bacteria is in the magnetite of magnetosomes. However, this is not the case for Tb-MSR-1 and Gd-MSR-1. In the latter cases, the edge energy of the spectra is shifted to higher energies, meaning that the average oxidation state of the Fe atoms is higher than the one corresponding to magnetite. The structure of the curve just above the white line (7130 - 7145 eV) is also different to that of magnetite, indicating that not only the oxidation state but also the local structural environment of the Fe atoms is different to magnetite. As shown previously, this cannot be attributed to the Tb-mag and Gd-mag, as in that case the incorporation of Tb and Gd resulted in a slight reduction of the average valence of the Fe atoms (shift of the edge energy to lower energies) with essentially no structural changes with respect to control magnetosomes.

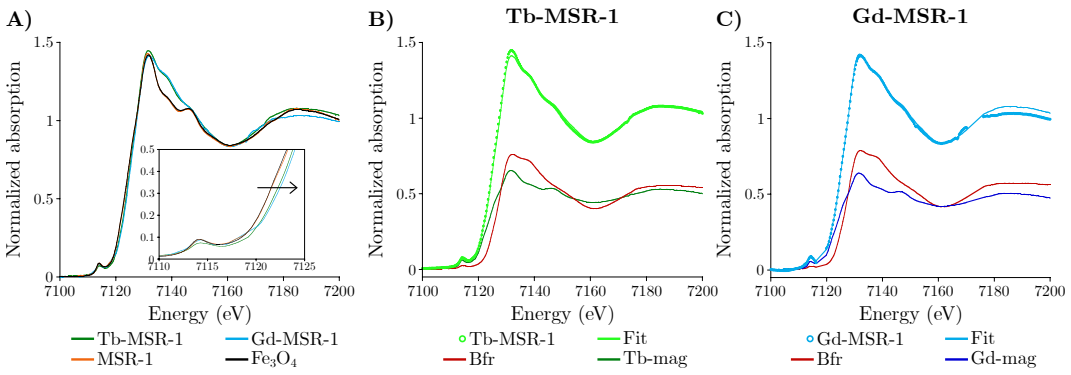


Figure 4.5: A) Fe K-edge XANES spectra of MSR-1, Tb-MSR-1 and Gd-MSR-1 with inorganic magnetite ($Fe_3O_4$) as a reference. B,C) Linear combination fits of Tb-MSR-1 and Gd-MSR-1 with their corresponding isolated magnetosomes (Tb-mag and Gd-mag) and ferrihydrite from bacterioferritin (Bfr).

Aiming to identify the Fe species contributing to the XANES spectra of Tb-MSR-1 and Gd-MSR-1, a linear combination fit of the spectra to standard Fe compounds was performed (Figure 4.5B,C). The results suggest that the spectra can be reproduced by considering a combination of the isolated magnetosomes (Tb-mag and Gd-mag) and ferrihydrite from bacterioferritin (Bfr). Bfr is the protein where bacteria store Fe in a phosphorus-rich ferrihydrite-like mineral phase [127], which is the Fe source for magnetosome biomineralization [33]. In both Tb-MSR-1 and Gd-MSR-1, the results of the fit return a similar atomic fraction, namely 49% of the Fe is in the magnetosomes and 51% in Bfr for Tb-MSR-1 and 47% of the Fe is in the magnetosomes and 53% in Bfr for Gd-MSR-1.

## 4.3 Morphological characterization

A subsequent TEM analysis was performed for the purpose of determining if the presence of $Tb^{3+}/Gd^{3+}$ in the culture media and the incorporation of these elements into MSR-1 induced changes on the bacterial morphology. A representative image of each condition is represented in Figure 4.6. No appreciable changes in cell morphology, magnetosome shape, and their arrangement in chains are observed in Tb-MSR-1 and Gd-MSR-1 compared to MSR-1.

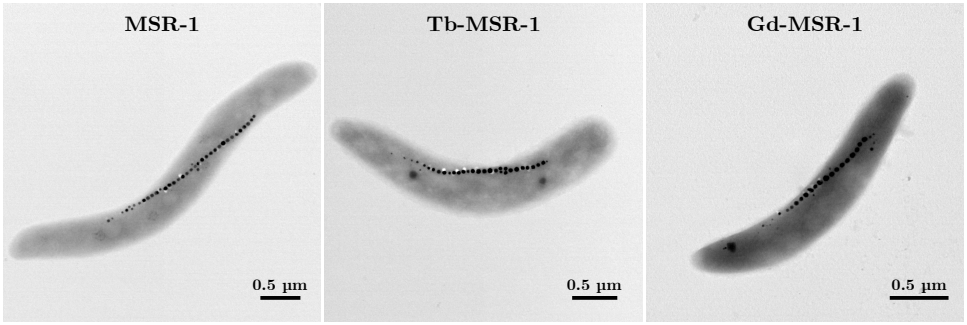


Figure 4.6: Representative TEM images of MSR-1, Tb-MSR-1 and Gd-MSR-1.

The number of magnetosomes per chain and the magnetosome size are expressed in Figure 4.7. The length of each box represents the central range covering 50% of the distribution, the horizontal line represents the mean value, and the ends of the bars represent the maximum and minimum values of each distribution. The length of the chains is similar in the three cases with a mean value of 24 magnetosomes per chain in the case of MSR-1 and Gd-MSR-1 and 22 magnetosomes per chain in Tb-MSR-1. Regarding magnetosome size, there are small differences as Tb-mag are slightly larger (46 ± 10 nm) than MSR-1 magnetosomes (42 ± 10 nm). On the contrary, Gd-mag are smaller (38 ± 12 nm).

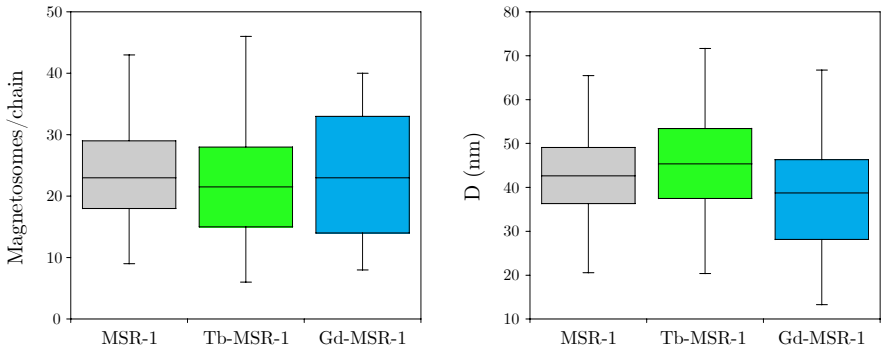


Figure 4.7: Left: distribution of number of magnetosomes per chain. Right: magnetosome size distribution.

### 4.3.1 Fluorescence in Tb-MSR-1

Such as other rare earth elements, Tb emits photoluminescence even when it is incorporated only as a trace element in different materials. It is known that $Tb^{3+}$ can replace $Ca^{2+}$ in biological systems as they have a similar ionic radius (0.92 Å for $Tb^{3+}$ and 0.99 Å for $Ca^{2+}$) [147]. As a result, Tb can form stable complexes with polypeptides replacing $Ca^{2+}$, and confers photoluminescence under UV excitation in the range of maximum protein absorption ($\lambda_{ex}$ = 285 nm) [148] with a maximum emission peak around 545 nm [149].

Under this premise, the photoluminiscence of Tb-MSR-1 and Tb-mag was tested with fluorimetry measurements and fluorescence microscopy. In the fluorimeter, samples were excited with a $\lambda_{ex}$ = 285 nm and the fluorescence spectrum was recorded in a range of 520 - 570 nm. The results are shown in Figure 4.8. A Tb-specific fluorescence peak is observed at 545 nm. No fluorescence is observed neither in MSR-1 nor in their magnetosomes. The fluorescence intensity is higher in Tb-MSR-1 than in Tb-mag stating, as suggested previously in XANES measurements, that Tb is found in other bacterial compartments apart from magnetosomes. The fluorescence emission in Tb-mag when excited with the maximum protein absorption wavelength indicates that Tb is linked to the proteins of the magnetosome membrane, and not only in their mineral core as observed from XANES measurements.

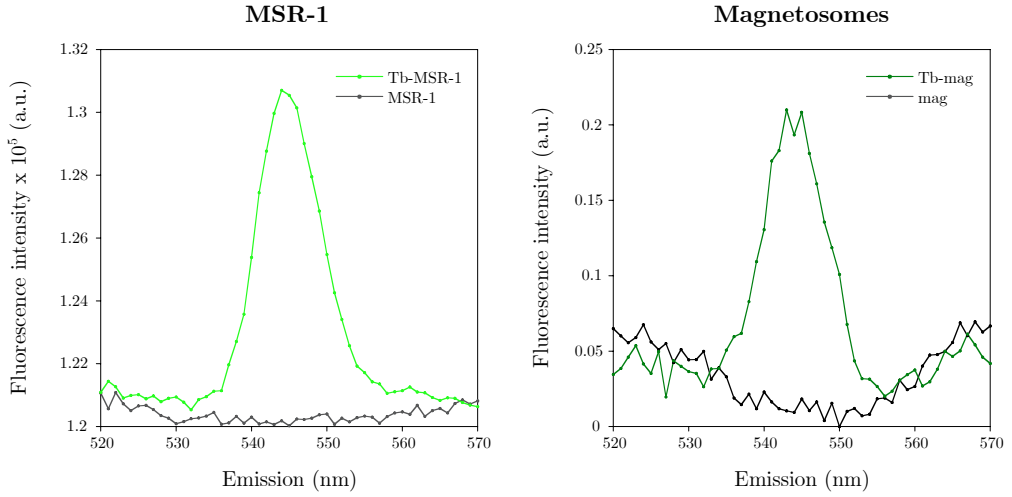


Figure 4.8: Photoluminiscence of Tb-MSR-1 and MSR-1 and their isolated magnetosomes (Tb-mag and mag) excited at $\lambda_{ex}$ = 285 nm.

Photoluminiscence of Tb-MSR-1 was also observed by fluorescence microscopy. Due to technical limitations, the samples were not excited at the optimum wavelength of 285 nm. The best results were observed when exciting Tb-MSR-1 with UV light using a band-pass filter (350/50) and the emission was collected with a cut-off filter from 500 nm. Figure 4.9 shows images of bright field and fluorescence microscopy of Tb-MSR-1. Even though the settings of the microscope were not optimal, fluorescent "objects" are observed in fluorescence mode that coincide with bacterial bodies in the bright field image.

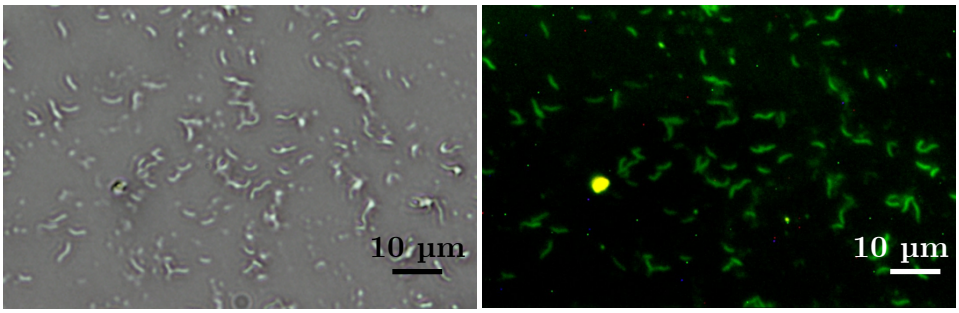


Figure 4.9: Microscopy images of Tb-MSR-1. Bright field (left) and fluorescence (right) ($\lambda_{ex}$ = 350/50 nm, $\lambda_{em}$ ≥500 nm)

## 4.4 Cytotoxicity of Tb-MSR-1 and Gd-MSR-1

In *Chapter 2* it was verified that MSR-1 do not cause cytotoxicity in A549 lung carcinoma cells as they do not affect their viability nor their growing ability. In this chapter the aim is to verify if Tb/Gd incorporation causes any change in MSR-1 cytotoxic potential. Cytotoxicity of Tb-MSR-1 and Gd-MSR-1 was assessed, following the same experimental setup as in *Chapter 2*. The obtained results were compared to the ones obtained with MSR-1.

As bacteria were fixed with glutaraldehyde before being put in contact with A549 cells, they showed green fluorescence [104]. Therefore, bacterial incorporation by cells could be verified by fluorescence measurements in a flow cytometer (Figure 4.10). The shift to higher fluorescence intensity was used to verify the loading of cells as they show fluorescence due to the presence of fluorescent bacteria.

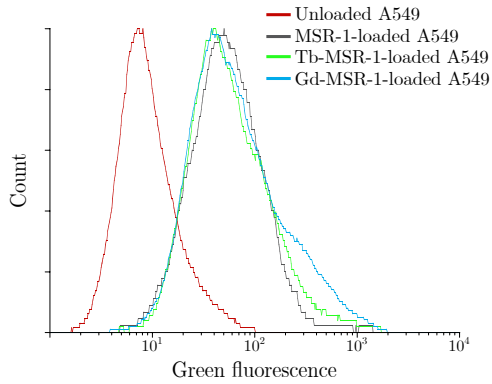


Figure 4.10: Fluorescence histogram obtained by flow cytometry showing the profile of unloaded and MSR-1/Tb-MSR-1/Gd-MSR-1-loaded A549 cells.

Cell viability was checked by flow cytometry and propidium iodide stain to differentiate dead from living cells. The red fluorescence histograms of one representative experiment are observed in Figure 4.11. The percentage of dead cells (cells showing high red fluorescence intensity) of that particular experiment is displayed.

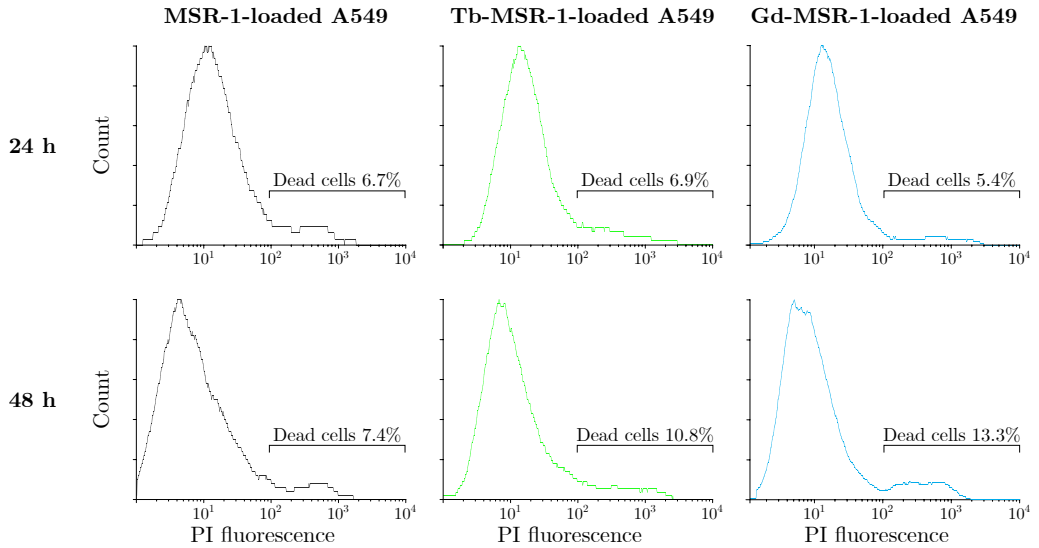


Figure 4.11: Fluorescence histograms of A549 stained with propidium iodide (PI) obtained by flow cytometry. The results correspond to MSR-1/Tb-MSR-1/ Gd-MSR-1-loaded cells after 24 h and 48 h of incubation.

Viability percentages of cell populations were calculated as the ratio between living and total cells (Table 4.1). Considering the results of three different experiments, there are no significant differences in cell viability in MSR-1-loaded cells without and with Tb or Gd. In every case the mean value of viability ranged between 87% and 91% after 48 h.

| **Viability** | | |
|---|---|---|
| | 24 h | 48 h |
| MSR-1-loaded A549 | 95.1 ± 3.4% | 90.1 ± 4.1% |
| Tb-MSR-1-loaded A549 | 92.1 ± 1.4% | 91.4 ± 2.4% |
| Gd-MSR-1-loaded A549 | 94.0 ± 1.1% | 87.1 ± 1.7% |

Table 4.1: Viability percentages after 24 h and 48 h of culturing MSR-1/Tb-MSR-1/Gd-MSR-1-loaded A549 cells. The results represent the mean ± standard deviation values, n = 3.

Figure 4.12 displays cell proliferation. It is observed that the growing ability of Tb-MSR-1/Gd-MSR-1-loaded A549 cells does not change significantly in comparison with MSR-1-loaded cells. After 48 h of culture cell populations increase by 1.5 in MSR-1 and Tb-MSR-1 loaded cells and by 1.3 in the case of Gd-MSR-1-loaded cells. In summary, these results of viability and proliferation indicate that the incorporation of Tb and Gd in MSR-1 do not change their cytotoxic potential.

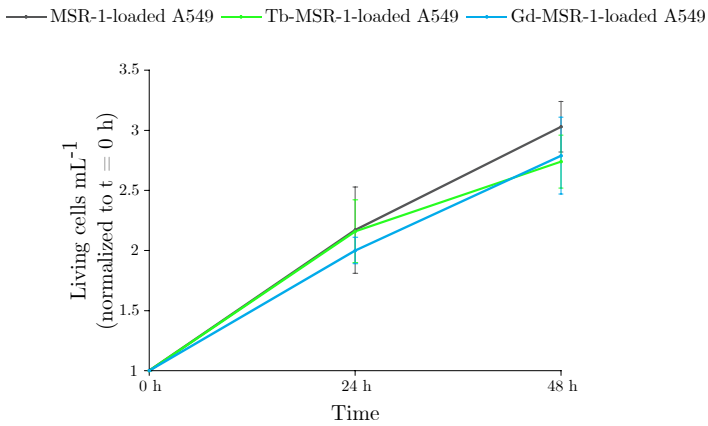


Figure 4.12: Time evolution of the number of living A549 cells normalized to t = 0 h. Data represent the mean ± standard deviation values, n = 3.

## 4.5 Conclusions

From the results discussed in this chapter it can be concluded that:

- The culture of magnetotactic bacteria in Tb and Gd supplemented media promotes the incorporation of these elements into the structure of magnetosomes and other bacterial compartments.
- Magnetotactic bacteria that have incorporated Tb and their isolated magnetosomes show photoluminiscence properties.
- The incorporation of terbium and gadolinium in *Magnetospirillum gryphiswaldense* does not change its cytotoxic potential. The modified bacteria do not affect the viability nor the growing ability of A549 cells.

# Chapter 5

# Outlook for new research lines

In previous chapters the experiments were performed with a single MTB species with which the research group has a long experience: *Magnetospirillum gryphiswaldense* MSR-1. In order to open new future research opportunities in the group, other species of MTB were explored during this thesis: *Magnetospirillum magneticum* AMB-1, *Magnetovibrio blakemorei* MV-1 and *Magnetococcus marinus* MC-1. Moreover, a genetic manipulation process to induce permanent changes in magnetosomes was established.

On the first part of this chapter, the culture strategies adapted to our facilities are presented and the morphological and magnetic characteristics of the aforementioned MTB are described. On the second part of the chapter, a genetic modification experiment to induce a permanent change on magnetosome characteristics of MSR-1 and AMB-1 is presented. This technique opens up many possibilities to modify MTB to express proteins of interest.

## 5.1 MTB characterization

Bacterial and magnetosome morphological description was performed by means of SEM and TEM imaging. Magnetic characterization was achieved by measuring the zero field cooling/field cooling (ZFC/FC) magnetization curves. Finally, X-ray absorption near edge spectroscopy (XANES) measured at the

Fe K-edge was performed in order to determine the Fe phases present in the bacteria.

### 5.1.1 *Magnetospirillum magneticum* AMB-1

*Magnetospirillum magneticum* AMB-1 was isolated by Matsunaga *et al.* [150] from ponds at Koganei in Tokyo (Japan). The strain used in this work (ATCC700264) was purchased from ATCC-American Type Culture Collection.

AMB-1 is spirillum-shaped with a length of 3 - 10 µm depending on its growing stage and it is motile by means of two polar flagella that can be observed in Figure 5.1.

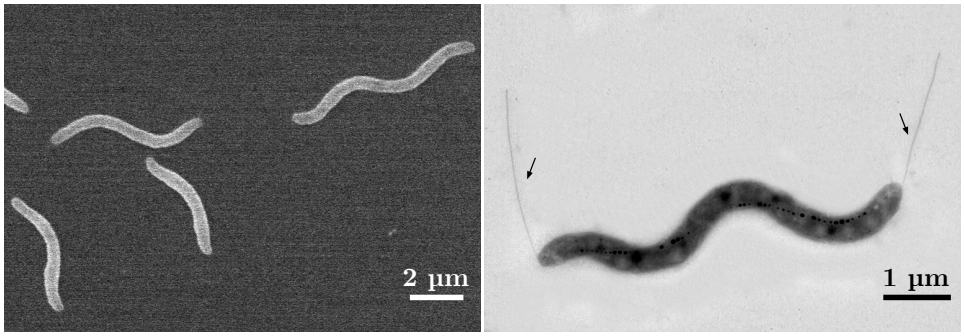


Figure 5.1: SEM (left) and TEM (right) images of AMB-1. The arrows point bacterial flagella.

ATCC suggests to culture AMB-1 in ATCC Medium 1653 (revised magnetic spirillum growth medium, MSGM). However, based on the group's previous experience with the magnetotactic spirillum MSR-1 and aiming to culture both species in the same medium to perform comparative experiments, AMB-1 was successfully cultured in FSM medium (see Materials and Methods for FSM composition). Following the oxygen concentration recommendation by ATCC, the culture vessels were filled with medium and the caps completely closed to achieve the microaerophilic conditions necessary for the successful magnetosome synthesis. The incubation was carried out at 30 °C without shaking.

In the ATCC AMB-1 culturing protocol and in the literature [28], a mixture of different chemical elements known as Wolfe's mineral solution (0.005% (v/v)) is added to the culture medium (see Materials and Methods). Therefore, although the growth of AMB-1 in FSM was satisfactory, Wolfe's mineral solution was also tested trying to upgrade the culture strategy. Bacterial and magnetosome characteristics between both conditions were compared, and for writing purposes will be described as AMB-1 (-W) and AMB-1 (+W) for bacteria grown in absence and presence of Wolfe's mineral solution, respectively.

The growth kinetics of AMB-1 (-W) and AMB-1 (+W) were studied. Figure 5.2 shows the exponential growth phase of both cultures from where the growth rate, $\mu$, and generation time, $g$, were estimated. As shown in Table 5.1, the growth rate of AMB-1 (-W) is slightly slower than the growth rate of AMB-1 (+W).

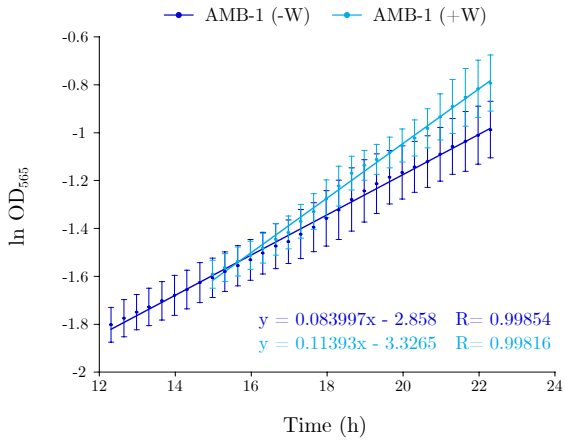


Figure 5.2: Exponential growth phase of AMB-1 (-W) and AMB-1 (+W). Data represent the mean ± standard deviation, n = 5. The line is an linear fit to the data.

| **Bacterial population** | $\mu$ **(h$^{-1}$)** | $g$ **(h)** |
|---|---|---|
| AMB-1 (-W) | 0.08 ± 0.01 | 8.37 ± 0.93 |
| AMB-1 (+W) | 0.11 ± 0.01 | 6.15 ± 0.50 |

Table 5.1: Growing parameters of AMB-1 (-W) and AMB-1 (+W): growth rate, $\mu$, and generation time, $g$. The results represent the mean ± standard deviation values, n = 5.

In Figure 5.3 TEM images of AMB-1 (-W) and AMB-1 (+W) are displayed. In both culture conditions, AMB-1 presents a fragmented magnetosome chain in opposition to MSR-1 that has one unbroken chain per bacteria. Figure 5.3 shows distribution histograms of the number of magnetosomes per chain, which are similar in both culture conditions. The mean values of the number of magnetosomes per chain are 23 ± 6 in AMB-1 (-W) and 22 ± 7 in AMB-1 (+W).

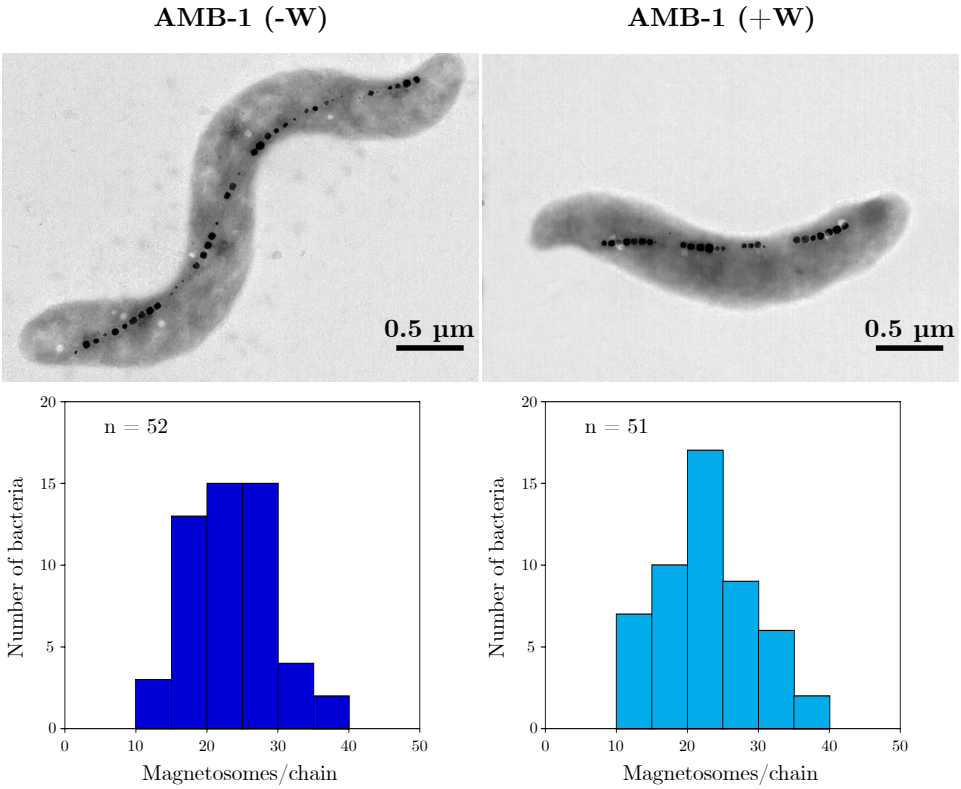


Figure 5.3: Top: TEM images of AMB-1 (-W) and AMB-1 (+W). Bottom: histograms showing the distribution of the number of magnetosomes per chain in AMB-1 (-W) and AMB-1 (+W).

Figure 5.4 shows TEM images of magnetosomes from AMB-1. Similarly to MSR-1, AMB-1 synthesizes cuboctahedral magnetosomes [4]. Nonetheless, their shape is more irregular. There are no significant morphological differences between magnetosomes from AMB-1 grown in both conditions (-W and +W). Magnetosome size distribution (Figure 5.4) and mean diameter are also similar and slightly bigger than in MSR-1: 49 ± 14 nm for AMB-1 (-W), 48 ± 13 nm for AMB-1 (+W) and 42 ± 10 nm for MSR-1.

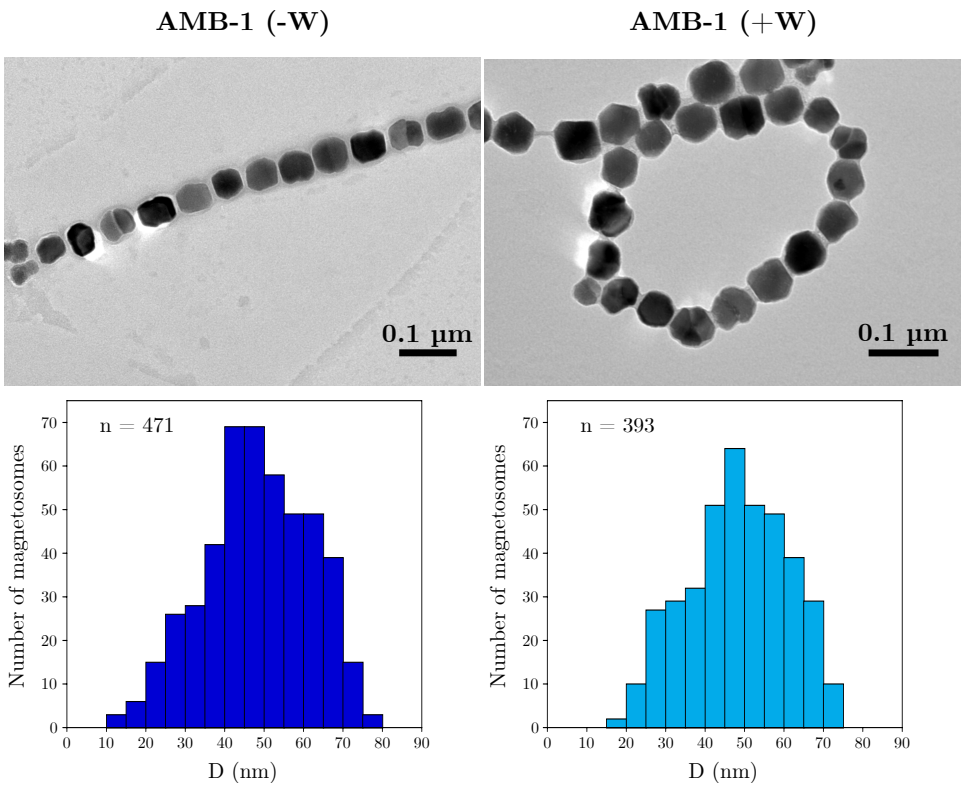


Figure 5.4: Top: TEM images of magnetosomes of AMB-1 (-W) and AMB-1 (+W). Bottom: Histograms showing magnetosome size distribution in AMB-1 (-W) and AMB-1 (+W).

The magnetic characterization of AMB-1 was also performed in the two tested conditions. Figure 5.5 shows the ZFC/FC magnetization curves. When no Wolfe's mineral solution is added to the culture medium, AMB-1 shows a Verwey transition temperature of ∼105 K, which is expected for magnetosomes [34, 145]. Moreover, the obtained curve has a similar shape to that of MSR-1. However, the ZFC-FC curve noticeably changes when Wolfe's mineral solution is added to the culture medium as the Verwey transition is less sharp than in AMB-1 (-W) and displaced towards lower temperatures (∼95 K). This decrease in $Tv$ can also be seen in the derivative of the ZFC represented on the inset of Figure 5.5. The peak of the derivative, which indicates the onset of Verwey transition, is shifted ∼8 K to lower temperatures in AMB-1 (+W) compared to AMB-1(-W). Taking into account that the Verwey transition is very sensitive to stoichiometry, this may suggest that elements from Wolfe's mineral solution may have entered the magnetite structure. A similar effect in

the Verwey transition was observed in *Chapter 4* when MSR-1 incorporated terbium and gadolinium and in previous studies when MSR-1 was doped with cobalt [36] or manganese [35].

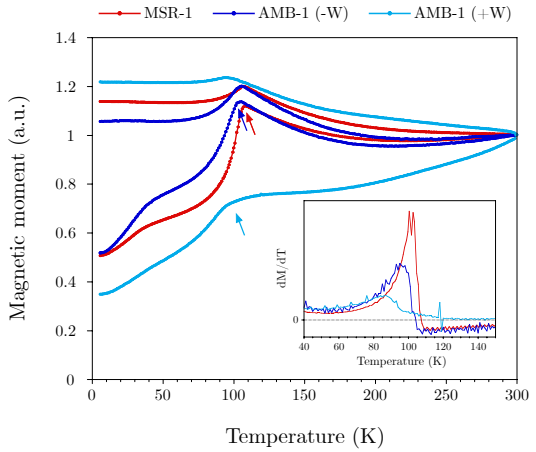


Figure 5.5: ZFC/FC curves measured at 5 mT of AMB-1 (-W) and AMB-1 (+W). ZFC/FC curve of MSR-1 is presented for the sake of comparison. The Verwey transition temperature, *Tv*, is pointed with an arrow corresponding to ∼105 K for AMB-1 (-W), ∼95 K for AMB-1 (+W) and ∼108 K for MSR-1. Inset: derivative of ZFC for the three samples.

To determine if any component from the Wolfe's mineral solution was entering the magnetosomes, ICP measurements of isolated magnetosomes were performed. Apart from iron, five other elements were tested: manganese, cobalt, copper, zinc and molybdenum. The relative percentage between each element and iron is shown in Table 5.2. The addition of Wolfe's mineral solution to the culture medium modifies magnetosome composition, mostly in the case of manganese. There was 6 times more manganese in AMB-1 (+W) magnetosomes than in AMB-1 (-W) magnetosomes. This element may have entered the magnetite structure of magnetosomes substituting Fe atoms, which would justify the change observed in the ZFC/FC curve.

| % Element/Fe | | |
|---|---|---|
| | AMB-1 (-W) | AMB-1 (+W) |
| Mn | 0.013 | 0.073 |
| Co | 0.019 | 0.006 |
| Cu | 0.028 | 0.043 |
| Zn | 0.411 | 0.376 |
| Mo | 0.003 | 0.003 |

Table 5.2: Relative percentage of different elements and iron measured by ICP in isolated magnetosomes of AMB-1 (-W) and AMB-1 (+W).

Regardless the differences observed in the Verwey transition between both samples, the Fe K-edge XANES spectra of AMB-1 (-W) and AMB-1 (+W) show no differences and overlap the XANES spectrum of pure magnetite (Figure 5.6). This suggests that the transition metal elements enter the magnetite structure of AMB-1 (+W) magnetosomes as dopants, hardly disturbing the coordination environment of the Fe atoms, although these minute deviations from the nominal stoichiometry do affect the Verwey transition. Similar results were observed by our group in Co and Mn doped magnetosomes of MSR-1 [22,35,36]. In the latter cases, the magnetic properties of magnetosomes and the Verwey transition were significantly affected by doping percentages as low as 1% (Co) and 2.3% (Mn) although the overall coordination environment of Fe was unaltered.

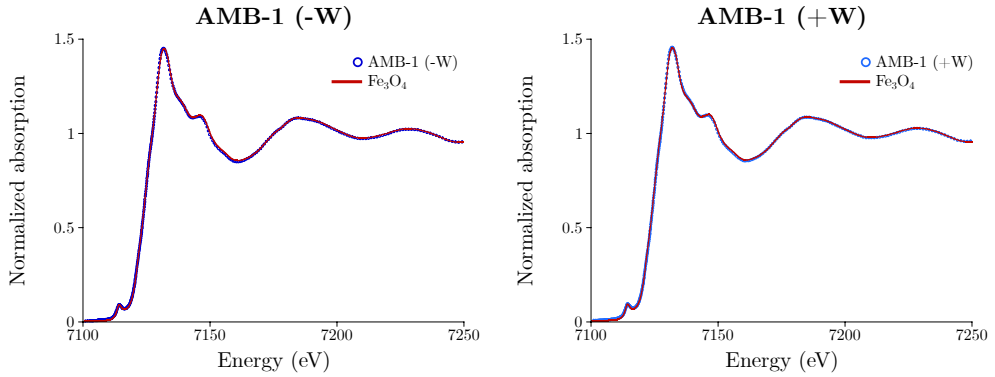


Figure 5.6: Fe K-edge XANES of AMB-1 (-W) and AMB-1 (+W) compared to inorganic magnetite ($Fe_3O_4$).

### 5.1.2 *Magnetovibrio blakemorei* MV-1

*Magnetovibrio blakemorei* MV-1 was isolated by Bazylinski *et al.* [151] from sulfide-rich sediments from a salt marsh pool at the Neponset River estuary near Boston, Massachusetts (USA). The strain used in this work (DSM 18854) was purchased from DSMZ-German Collection of Microorganisms and Cell Cultures GmbH.

MV-1 was cultured following the indications kindly provided by Dr. Pedro Leão from the Department of Marine Science, University of Texas (USA) [152]. In order to promote magnetosome synthesis, MV-1 was cultured anaerobically under $N_2O$ atmosphere. The incubation was performed at 30 °C without shaking. More information on the culture medium can be found in the Materials and Methods section.

Figure 5.7 shows electron microscopy images of MV-1. The bacteria present a vibrioid to helicoid shape with a length of around 2 - 3 µm. They are motile thanks to a single flagellum at one pole (Figure 5.7A).

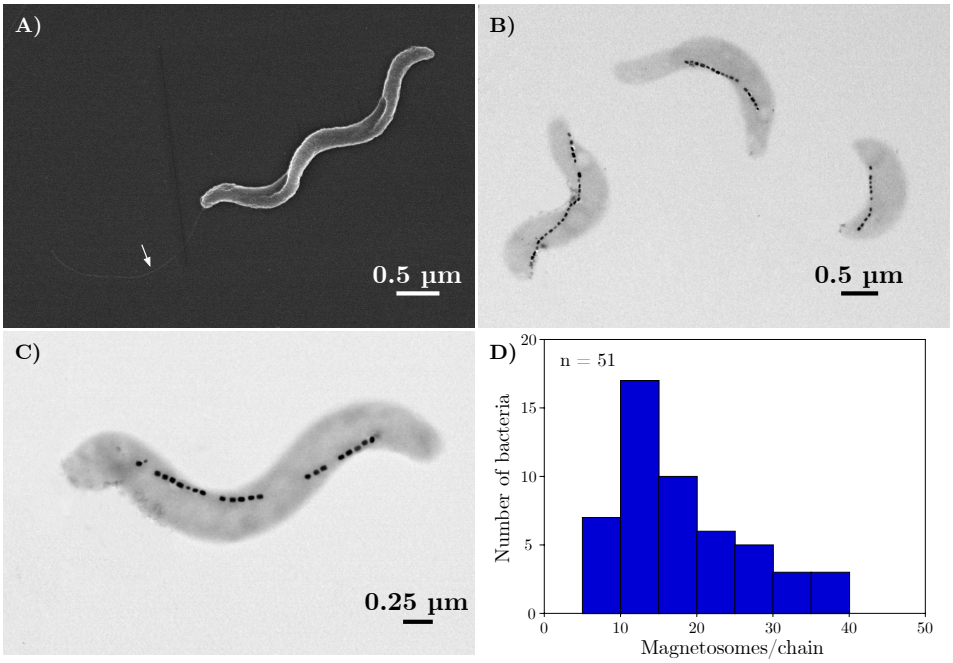


Figure 5.7: A) SEM and B,C) TEM images of MV-1. The arrow points bacterial flagellum. D) Histograms showing the distribution of the number of magnetosomes per chain in MV-1.

MV-1 forms one single chain positioned along the bacterial long axis that sometimes appears fragmented (Figure 5.7B,C). The number of magnetosomes per chain shows a broad distribution although the highest frequency is found between 10 - 20 magnetosomes per chain with a mean value of 18 ± 8 magnetosomes per chain (Figure 5.7D).

As shown in Figure 5.8, MV-1 synthesize elongated magnetosomes whose crystal habit is truncated hexaoctahedral [153, 154]. Magnetosomes present a narrow size distribution with a length of 44 ± 10 nm in the long axis and a width of 31.5 ± 6 nm in the short axis.

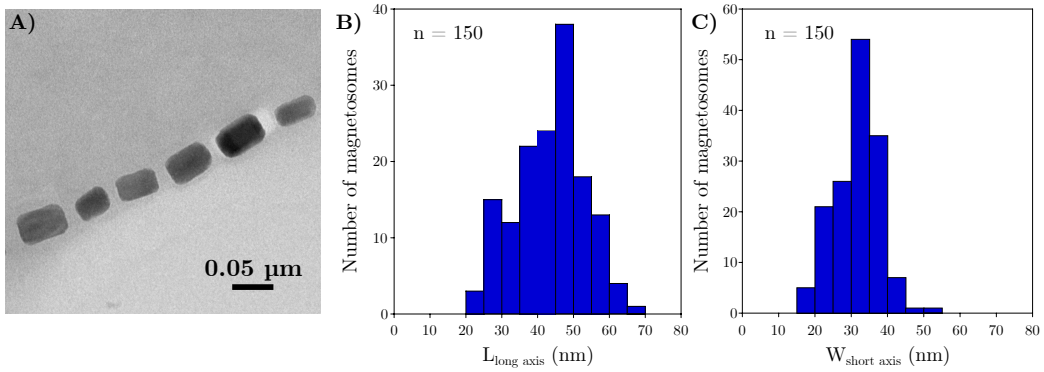


Figure 5.8: A) TEM image showing MV-1 magnetosomes. B,C) MV-1 magnetosome size distribution histograms of the long axis (B) and the short axis (C).

Regarding the magnetic characterization, Figure 5.9 shows the ZFC/FC curve of MV-1. There is no Verwey transition which could indicate that the magnetite deviates from the nominal stoichiometry, as the medium is also enriched with Wolfe's mineral solution. Indeed, the analysis of the magnetic properties of MV-1 suggests that their magnetosomes are doped with cobalt [155]. In addition, there is a paramagnetic contribution appearing at low temperatures in both the ZFC and FC curves that will be discussed later.

The Fe K-edge XANES spectrum of MV-1 is shown in Figure 5.9. Unlike for AMB-1, the spectrum is not coincident with that of magnetite. Aiming to identify the Fe phases present in the measured sample, the spectrum was fitted to a linear combination of reference compounds including magnetite, ferrihydrite from bacterioferritin (Bfr), and iron citrate. The best fit corresponds to 71% Bfr and 29% Fe citrate. The fact that most of the Fe is in the Bfr phase

suggests that the biomineralization process on the measured sample was ongoing and that the magnetosomes were still immature, since it has been proven that bacteria store iron in Bfr before magnetosome formation [33]. Moreover, the presence of Bfr explains the paramagnetic contribution observed at low temperature in the ZFC/FC curve shown in Figure 5.9 [127]. Furthermore, the presence of Fe citrate in the linear combination fit is attributed to the bacterial growth medium being enriched with iron quinate, a molecule of chelated Fe(III) similar to iron citrate.

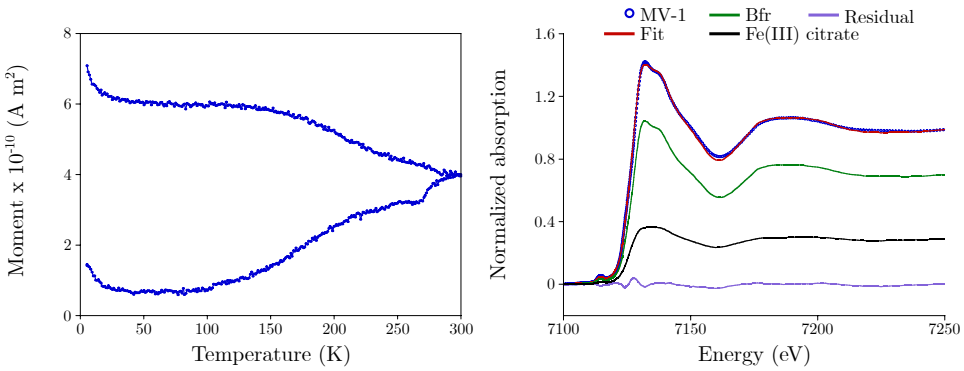


Figure 5.9: Left: MV-1 ZFC/FC magnetization curve measured at 5 mT. Right: MV-1 Fe K-edge XANES spectrum fitted with bacterioferritin (Bfr) and Fe(III) citrate.

### 5.1.3 *Magnetococcus marinus* MC-1

*Magnetococcus marinus* MC-1 was isolated by Meldrum *et al.* [156] from the oxic/anoxic interface of the Pettaquamscutt Estuary in Rhode Island (USA). The strain used in the present work was kindly provided by Dr. Christopher Lefèvre from the Institut de Biosciences et Biotechnologies d'Aix-Marseille (BIAM), CEA Cadarache (France).

MC-1 was grown following the indications of Dr. Lefèvre (Materials and Methods). It is an obligate microaerophile [157] and therefore it was grown in a semi-solid oxygen concentration gradient medium, where the bacteria formed a growth band in the oxic/anoxic interface.

Figure 5.10 shows electron microscopy images of MC-1. It presents a coc-

coid shape of around 1 µm diameter. These bacteria are motile as they contain two bundles of seven flagella located on one side of the cell [157]. Some of these flagella can be observed in the SEM image presented in Figure 5.10.

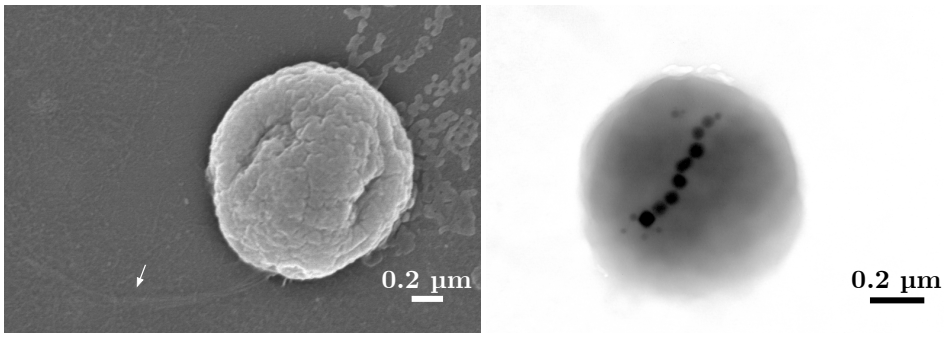


Figure 5.10: SEM (left) and TEM (right) images of MC-1. The arrow points bacterial flagella.

Figure 5.11 shows a TEM image of a dividing MC-1 bacterium and the magnetosome size distribution histogram. MC-1 forms one single chain of around 8 magnetosomes. It can be observed that MC-1 shares equally the magnetosome chain between the two new bacterial cells when it divides. Magnetosomes present a size of 51 ± 12 nm and a pseudo-hexagonal prismatic crystal habit [157]. However, the results shown must be considered as preliminary because the number of bacteria in the analyzed sample was low as they only grow forming a band in the oxic/anoxic interface in tubes with semisolid medium.

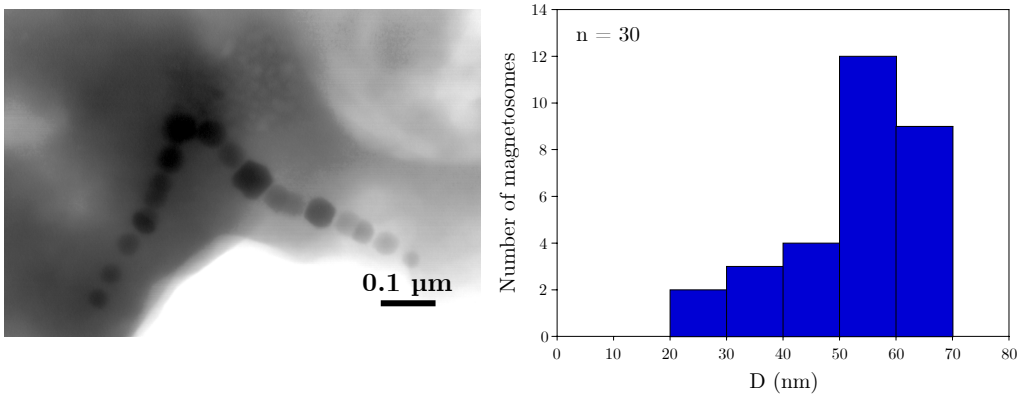


Figure 5.11: Left: TEM image of MC-1. Right: MC-1 magnetosome size distribution histogram.

Figure 5.12 shows the ZFC/FC curve of MC-1. Although the signal is noisy due to the low bacterial concentration, the Verwey transition is visible. Comparison with MSR-1 shows that the Verwey temperature is significantly higher, ∼120 K, closer to that of bulk magnetite.

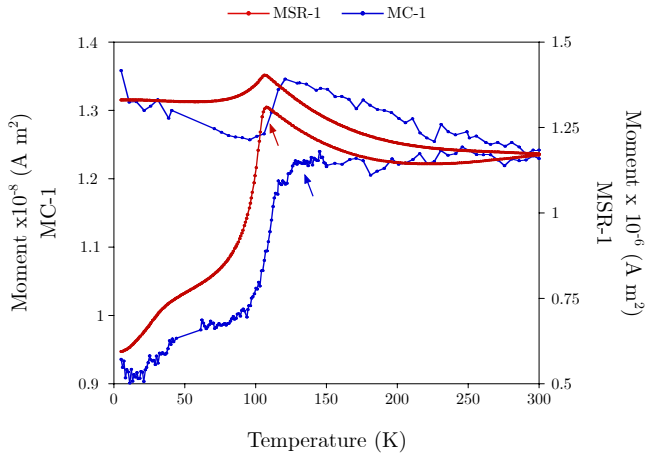


Figure 5.12: ZFC/FC curves measured at 5 mT of MC-1 and MSR-1. The Verwey transition is pointed with an arrow corresponding to ∼120 K for MC-1 and ∼108 K for MSR-1.

## 5.2 Genetic modification of MTB

Genetic modification can be used to induce a permanent change in MTB and/or magnetosomes. As there was no previous experience in genetic engineering in the research group, this work was performed in BIAM/Molecular and Environmental Microbiology (MEM), CEA Cadarache (France) in collaboration with Dr. Sandra Prévéral and Dr. Damien Faivre.

The experiment was designed to modify the characteristics of the magnetosome membrane of MSR-1 and AMB-1 by fusing the membrane protein MamC with Venus fluorescent protein linked to the small peptide RGD. A representation of the modified magnetosome is observed in Figure 5.13.

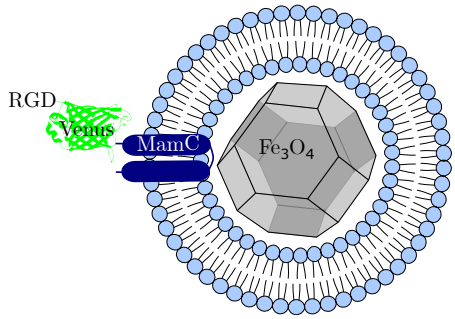


Figure 5.13: Representation of Venus-RGD modified magnetosome.

MamC is the most abundant magnetosome-associated protein [158,159]. It is a highly conserved 12.4 kDa protein existing in most magnetotactic $\alpha$-proteobacteria [160]. The gene sequence of *mamC* varies slightly between species of MTB. *mamC* from MSR-1 and AMB-1 has an 80% of genetic identity.

Venus protein (a.k.a. SEYFP-F46L) is a yellow fluorescent protein derived from *Aequorea victoria* [161]. Venus fluorescence spectra are represented in Figure 5.14. It presents a maximum of excitation at 515 nm and a maximum of emission at 528 nm.

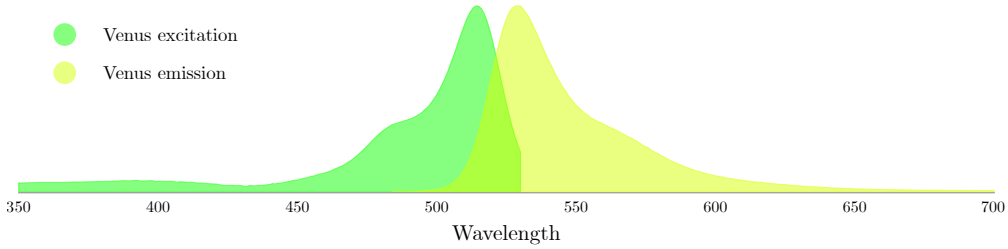


Figure 5.14: Venus excitation and emission spectra. Data obtained from Fluorescent Protein Database (www.fpbase.org/protein/venus/).

RGD (Arginine, Glycine, Aspartic acid) is a peptide that binds with high affinity to $\alpha_v\beta_3$ integrin receptors overexpressed by tumor cells. Therefore, magnetosomes functionalized with RGD peptide may interact with cancer cells more efficiently than native magnetosomes [52].

The genetic modification was performed by introducing the plasmid *pBBR-mamC-Venus-RGD* in *M. gryphiswaldense* MSR-1 and *M. magneticum* AMB-1.

The plasmid used (*pBBR-mamC-Venus-RGD*) contained *mamC*, *Venus*, and *RGD* genetic sequences inserted in the broad host range plasmid pBBR1MCS-2, which replicates in many Gram-negative bacteria. The sequence of *mamC* used in this experiment was that of AMB-1. A scheme of *pBBR-mamC-Venus-RGD* plasmid is represented in Figure 5.15.

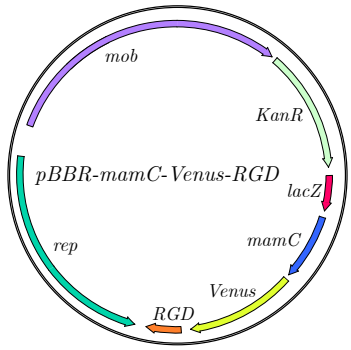


Figure 5.15: Scheme of *pBBR-mamC-Venus-RGD* plasmid used for the modification of *Magnetospirillum* spp.

A scheme of the experimental procedure is described in Figure 5.16 (for more detailed information see Materials and Methods).

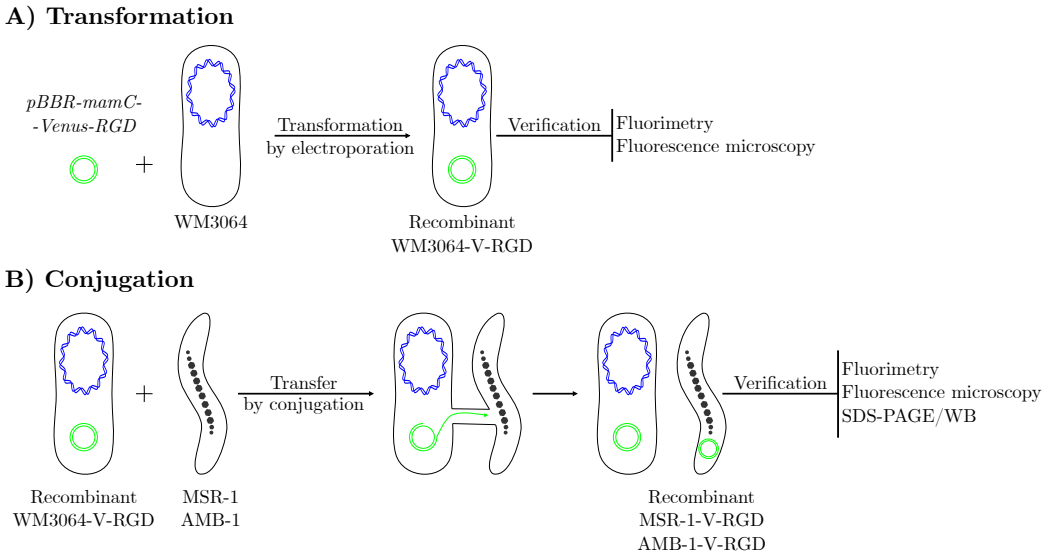


Figure 5.16: Experimental design used to genetically modify *Magnetospirillum* spp.

*pBBR-mamC-Venus-RGD* was inserted in *E. coli* strain WM3064 by electroporation (Figure 5.16A). Using Venus as a fluorescent reporter of the recombinant bacteria, the verification of the plasmid expression in recombinant WM3064 was performed by fluorimetry and fluorescence microscopy.

*Magnetospirillum* spp. were modified by conjugation using recombinant WM3064 as a donor (Figure 5.16B). For selection of recombinant MSR-1 and AMB-1 after conjugation, they were cultured in medium without diaminopimelic acid (DAP) and supplemented with kanamycin. As WM3064 is auxotrophic for DAP, the absence of this compound in the culture medium prevented WM3064 from growing. Adding kanamycin to the culture medium blocked non-recombinant *Magnetospirillum* spp. growth because they are sensitive to kanamycin.

The fluorescence of MSR-1-Venus-RGD and AMB-1-Venus-RGD and their magnetosomes was verified by fluorimetry measurements (Figure 5.17). Both bacteria and magnetosomes show a maximum of fluorescence at ∼530 nm, coincident with the maximum emission peak of Venus protein.

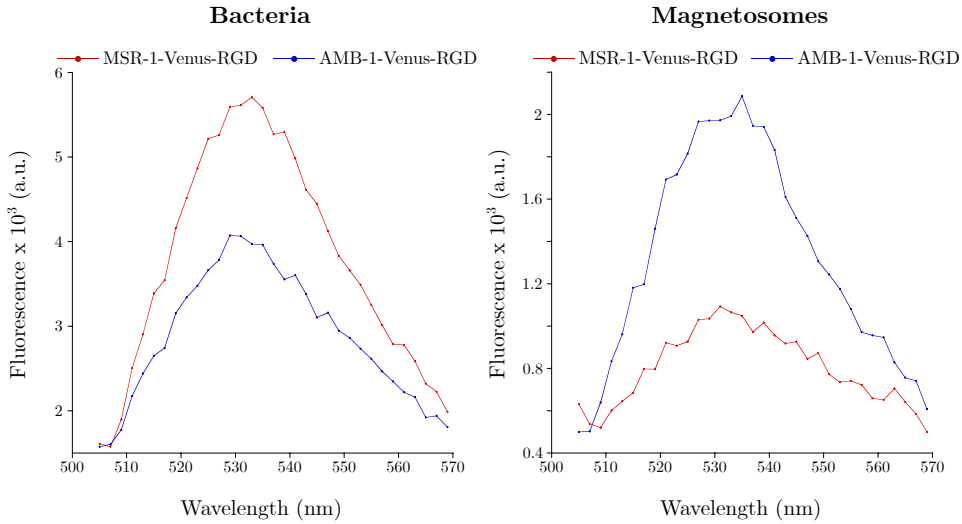


Figure 5.17: Fluorescence spectra of MSR-Venus-RGD and AMB-1-Venus-RGD and isolated magnetosomes obtained with an excitation wavelength of 470 nm.

The fluorescent MSR-1-Venus-RGD and AMB-1-Venus-RGD were observed by fluorescence microscopy (Figure 5.18). From the images it can be inferred

that fluorescence is not uniformly distributed throughout the bacteria, presumably because Venus is only attached to the magnetosome membrane, so the fluorescence is concentrated where magnetosomes are.

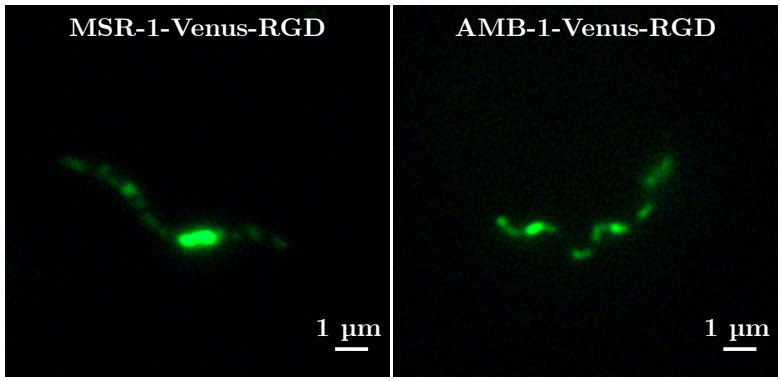


Figure 5.18: Fluorescence images of MSR-1-Venus-RGD and AMB-1-Venus-RGD excited with an excitation filter of $\lambda_{ex} = 480/20$ nm, and a long pass emission filter $\lambda_{em} \geq 520$ nm.

To verify the expression of Venus protein in magnetosome membrane of recombinant *Magnetospirillum* spp., SDS-PAGE and Western blot on the isolated magnetosomes were performed. In order to compare the results of the two species the same amount of magnetosomes were charged in the gel. The results are displayed in Figure 5.19. Knowing that the expected weight of the chimeric MamC-Venus-RGD protein was of ∼42 kDa, the corresponding band can be identified and is marked in yellow on Figure 5.19.

To confirm the selected band, the Western blot was proved with an anti-Venus antibody making the visualization of the band of interest possible. The results indicate that Venus was expressed in the membrane of both bacterial strain magnetosomes, even though the *mamC* sequence used was that of AMB-1. The Western blot allows for a semi-quantitative comparison of Venus expression level based on the contrast of the obtained bands. In this case, there was no significant difference in the effectiveness of either strain to express Venus as both presented similar levels of this protein.

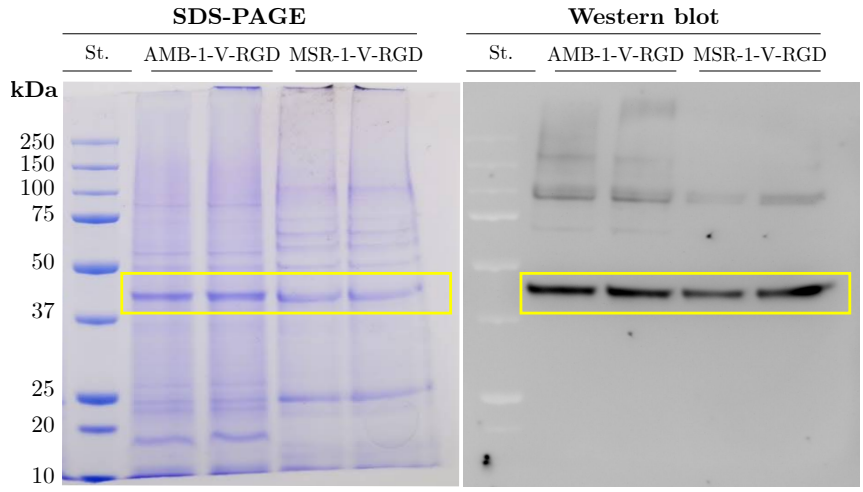


Figure 5.19: Left: SDS-PAGE showing the protein profile of magnetosome membrane of AMB-1-Venus-RGD and MSR-1-Venus-RGD. Right: Western blot probed with anti-Venus antibody. The chimeric protein MamC-Venus-RGD is marked with the yellow box.

In view of the obtained results it can be concluded that the plasmid of interest was successfully inserted in *Magnetospirillum* spp. and the correspondent proteins were expressed. Therefore, this procedure could be used to functionalize magnetosomes with other fluorescent markers, enzymes, or new peptides that bind with high affinity to cancer cells of a specific type increasing the efficiency of the considered treatment.

## 5.3 Summary

If MTB or magnetosomes are to be used in biomedical applications it is essential to choose the most suitable species taking into account not only their own characteristics but their requirements for growing and synthesizing magnetosomes.

Table 5.3 displays the main characteristics of the MTB species used in this thesis, including MSR-1 and the species presented in this chapter.

| Characteristic | MSR-1 | AMB-1 | MV-1 | MC-1 |
|---|---|---|---|---|
| Cell morphology | Spirillum | Spirillum | Vibroid-helicoid | Coccoid |
| Cell length (µm) | 3 - 10 | 3 - 10 | 2 - 3 | 1 |
| Flagella | 2 polar | 2 polar | 1 polar | 2 bundles of 7 |
| Magnetosome morphology | Cuboctahedral | Cuboctahedral | Truncated hexaoctahedral | Pseudo-hexagonal prismatic |
| Magnetosome size (nm) | 42 ± 10 | 49 ± 14 | 44 ± 10 (length)<br>31.5 ± 6 (width) | 51 ± 12 |
| Magnetosomes/chain | 25 ± 8 | 23 ± 6 | 18 ± 8 | 8 ± 2 |
| *Tv* (K) | ∼ 108 K | ∼ 105 K | ND | ∼ 120 K |

Table 5.3: Summary of the main morphological and magnetic characteristics of the MTB species presented in this thesis.

*M. gryphiswaldense* and *M. magneticum* and their magnetosomes have been thoroughly studied for cancer treatment using magnetic hyperthermia [37, 45, 49, 64, 66, 99, 162] and photothermia [61] as well as contrast agents for magnetic resonance imaging [52–54] and magnetic particle imaging [55]. The main advantage of both species is that their culture can be easily and cheaply scaled up as they grow in a culture medium with no special requirements. They grow microaerobically and no fine control of the gas atmosphere is required for their successful magnetosome production. Moreover, several genetic procedures have been established to functionalize their magnetosomes with fluorescent proteins [52, 60–62], enzymes [163, 164] and other peptides and proteins [63, 165, 166].

*M. blakemorei* forms elongated prismatic magnetosomes. This elongated morphology yields a strong uniaxial magnetic shape anisotropy along the long direction of the magnetosome, stronger than in the case of cuboctahedral magnetosomes synthesized by *Magnetospirillum* spp. [155, 167]. Magnetic anisotropy plays an important role in increasing the heating efficiency in magnetic hyperthermia [168, 169]. Thus, magnetosomes from *M. blakemorei* may be more suitable for magnetic hyperthermia treatments than those of *Magnetospirillum* spp. However, *M. blakemorei* is tedious to culture as it needs an anaerobic atmosphere with $N_2O$ to synthesize magnetosomes making the process more difficult and expensive.

Lastly, compared with the other presented species, *M. marinus* stands out as the best microswimmer as it presents two bundles of flagella. Moreover, it is smaller compared to the other species which could make it more suitable

to be injected and navigate inside the human body. Therefore, *M. marinus* has a big potential as drug delivery carrier that could swim along the blood vessels towards the target area [56, 170]. Apart from delivering compounds it could also be used like other species as a hyperthermia agent. However, production yield of *M. marinus* is low as it is currently cultured in semi-solid medium where it grows within a band in the oxic/anoxic zone. Thus, the culture conditions of *M. marinus* should be improved significantly if it is to be used for biomedical applications.

# Materials and Methods

In this section the materials and methods used during this thesis are explained in detail:

# Bacterial and eukaryotic cell culture

## Bacterial strains and cell lines

The bacterial strains and eukaryotic cell lines used for this thesis are listed below with the respective reference numbers.

*Magnetospirillum gryphiswaldense* MSR-1 ····· DSMZ: DSM 6361
*Magnetospirillum magneticum* AMB-1 ····· ATCC: 700264
*Magnetovibrio blakemorei* MV-1 ····· DSMZ: DSM 18854
*Magnetococcus marinus* MC-1 ···· Courtesy of Dr. Christopher Lefèvre
*Escherichia coli* WM3064 ····· Courtesy of Dr. Sandra Prévéral
Human lung carcinoma cell line A549 ····· DSMZ: ACC 107
Murine macrophage line RAW 264.7 ····· ATCC: TIB-71

## Bacterial culture media and reagents

### Flask standard medium (FSM) [171]

Flask standard medium (FSM) was used for the culture of *Magnetospirillum* spp. It contained per liter of distilled water:

$KH_2PO_4$ ····· 0.1 g
$MgSO_4 \cdot 7H_2O$ ····· 0.15 g
HEPES ····· 2.38 g
$NaNO_3$ ····· 0.34 g
Yeast extract ····· 0.1 g
Peptone from soybean ····· 3 g
Sodium pyruvate ····· 3 g
Agar (for solid medium) ····· 15 g

The pH was adjusted to 6.9. The medium was sterilized by autoclave at 121 °C for 20 minutes and the following ingredient was added:

Fe(III)-citrate (10 mM) ····· 10 mL

### Modified *Magnetospirillum* growth medium (MSGM) [172]

Modified *Magnetospirillum* growth medium (MSGM) was used for the culture of *M. magneticum* in the genetic modification experiments presented in *Chapter 5*. It contained per liter of distilled water:

| | |
|---|---|
| L-Ascorbic acid | 0.035 g |
| Sodium acetate | 0.07 g |
| Sodium thiosulfate | 0.1 g |
| $NaNO_3$ | 0.12 g |
| Succinic acid | 0.37 g |
| L-Tartaric acid | 0.37 g |
| $KH_2PO_4$ | 0.68 g |
| Modified Wolfe's mineral solution | 5 mL |
| Agar (for solid medium) | 15 g |

The pH was adjusted to 6.9. After autoclaving the medium at 121 °C for 20 minutes, the following ingredients were added:

| | |
|---|---|
| Wolfe's vitamin solution | 10 mL |
| Fe(III)-citrate (10 mM) | 10 mL |

### MV-1 medium [152]

MV-1 medium was used to grow *M. blakemorei*. Following the indications of Dr. Pedro Leão the medium contained per liter of ASW:

| | |
|---|---|
| Sodium succinate · $6H_2O$ | 18.84 g |
| Sodium acetate | 0.2 g |
| Acid-hydrolized casein | 3.3 g |
| Modified Wolfe's mineral solution | 33.4 mL |

The pH was adjusted to 7. The medium was distributed into Hungate tubes and fluxed with $N_2O$ for 20 minutes. After autoclaving at 121 °C for 20 minutes, and once the media was cooled down to room temperature, the following reagents were added per tube (12 mL of medium):

| | |
|---|---|
| Freshly made cysteine solution (4% (w/v)) | 30 µL |
| Fe(III)-quinate (10 mM) | 120 µL |

**MC-1 medium [157]**

MC-1 medium was used to culture *M. marinus*. Following the indications of Dr. Cristopher Lefèvre, the medium contained per liter of ASW:

| | |
|---|---|
| Sodium resazurin solution (1% (w/v)) | 0.1 mL |
| Modified Wolfe's mineral solution | 5 mL |
| $NH_4Cl$ | 0.3 g |
| HEPES | 2.4 g |
| $NaHCO_3$ | 1.26 g |
| Agar | 1.6 g |

The pH of the media was adjusted to 6 prior to autoclaving at 121 °C for 20 minutes. After the medium cooled down to 45 °C the following components were added per liter:

| | |
|---|---|
| Wolfe's vitamin solution | 0.5 mL |
| Phosphate buffer (0.5 M, pH 7) | 1.8 mL |
| Sodium thiosulfate solution (40% (w/v)) | 3 mL |
| Freshly made cysteine solution (4% (w/v)) | 10 mL |
| Fe(II)-sulfate (10 mM) | 3 mL |

The pH was adjusted to 7 in sterility. The medium was distributed into tubes that were left at room temperature for the oxygen gradient to form.

The inoculation was made in the oxic/anoxic zone of the tubes coincident with the zone of color change from transparent to pink due to resazurin.

### Modified Wolfe's mineral solution

The modified Wolfe's mineral solution was used to enrich culture media. It contained per liter of distilled water:

| | |
|---|---|
| $MgSO_4 \cdot 7H_2O$ | 3 g |
| $MnSO_4 \cdot H_2O$ | 0.5 g |
| NaCl | 0.1 g |
| $CoCl_2 \cdot 6H_2O$ | 0.1 g |
| $CaCl_2 \cdot 2H_2O$ | 0.13 g |
| $ZnSO_4 \cdot 7H_2O$ | 0.1 g |
| $CuSO_4 \cdot 5H_2O$ | 0.01 g |
| $AlK(SO)_4 \cdot 12H_2O$ | 0.01 g |
| $H_3BO_3$ | 0.01 g |
| $Na_2MoO_4 \cdot 2H_2O$ | 0.01 g |

The pH was adjusted to 6.5. The solution was sterilized by filtration and stored at 4 °C.

### Wolfe's vitamin solution

Wolfe's vitamin solution was added to MSGM and MC-1 media. It contained per liter of distilled water:

| | |
|---|---|
| Biotin | 2 mg |
| Folic acid | 2 mg |
| Pyridoxine hydrochloride | 10 mg |
| Thiamine · HCl | 5 mg |
| Riboflavin | 5 mg |
| Nicotinic acid | 5 mg |
| Calcium D-(+)-pantothenate | 5 mg |
| Vitamin B12 | 0.1 mg |
| p-Aminobenzoic acid | 5 mg |
| Thioctic acid | 5 mg |

The solution was sterilized by filtration and stored at 4 °C.

**Artificial sea water (ASW)**

MV-1 and MC-1 culture media were made using artificial sea water (ASW) as the base. The ASW contained per liter of distilled water:

| | |
|---|---|
| NaCl | 16.4 g |
| $MgCl_2 \cdot 6\ H_2O$ | 3.5 g |
| $Na_2SO_4 \cdot 10H_2O$ | 6.3 g |
| KCl | 0.5 g |
| $CaCl_2 \cdot 2H_2O$ | 0.4 g |

**Fe(III)-quinate, Tb(III)-quinate and Gd(III)-quinate**

To obtain Fe(III)-quinate 10 mM the following reagents were mixed per 100 mL of distilled water:

| | |
|---|---|
| $FeCl_3$ | 0.27 g |
| D-(-)-Quinic acid | 0.19 g |

To obtain Tb(III)-quinate and Gd(III)- quinate 10 mM the following reagents were mixed per 100 mL of distilled water:

| | |
|---|---|
| $TbCl_3 \cdot 6H_2O / GdCl_3 \cdot 6H_2O$ | 0.62 g |
| D-(-)-Quinic acid | 0.19 g |

The solutions were sterilized by filtration.

**Phosphate buffer**

Phosphate buffer (0.5 M) used for MC-1 medium was made by mixing separately:

| | |
|---|---|
| Solution 1: | |
| $K_2HPO_4$ | 17.418 g |
| Distilled water | 200 mL |

Solution 2:
$KH_2PO_4$ ..... 6.805 g
Distilled water ..... 100 mL

While stirring, solution 2 was added into solution 1 until pH 7. The buffer was sterilized by autoclave at 121 °C for 20 minutes and stored at 4 °C.

**Luria-Bertani broth**

Luria-Bertani (LB) broth and agar were used to culture *E. coli* WM3064. It contained per liter of distilled water:

NaCl ..... 5 g
Tryptone ..... 10 g
Yeast extract ..... 5 g
Agar (for solid medium) ..... 15 g

pH was adjusted to 7 and the medium was autoclaved (121 °C, 20 minutes).

**SOC medium**

SOC medium (Invitrogen, 15544034) was purchased ready to use. It contained per liter of medium:

NaCl ..... 10 mM
Tryptone ..... 2%
Yeast extract ..... 0.5%
KCl ..... 2.5 mM
$MgCl_2$ ..... 10 mM
$MgSO_4$ ..... 10 mM
Glucose ..... 20 mM

### Eukaryotic cell culture

A549 and RAW 264.7 cells were cultured in RPMI-1640 medium (Sigma-Aldrich, R6504) supplemented with:

| | |
|---|---|
| L-glutamine | 2 mM |
| Fetal bovine serum (heat deactivated) | 10% |
| Penicillin | 100 U $mL^{-1}$ |
| Streptomycin | 100 µg $mL^{-1}$ |
| Amphotericin B | 0.25 µg $mL^{-1}$ |

Cells were cultured at 37 °C in an humidified atmosphere (95 % relative humidity) and 5% $CO_2$.

## Microscopy

### Bright field and fluorescence microscopy

Bright field and fluorescence microscopy were performed with an epifluorescence microscope Nikon Eclipse Ni-E. Images were taken by using a Nikon DS-Fi2 camera and NIS-Elements imaging software.

For bacterial fluorescence observations and counting, cells were stained with acridine orange (0.01 % w/v) for 2 minutes. For counting bacteria, a known volume was filtered using polycarbonate membranes with 0.2 µm pore size. Filters were mounted on microscopy slides for their observation. For eukaryotic cells, in order to distinguish the nuclei from other cellular structures, they were stained by using Hoechst 33342 for 15 minutes before observation.

For Tb-MSR-1 fluorescence observations, the images were recorded with an optical inverted microscope with epi configuration (Olympus BX51) equipped with a X-CITE series 120Q fluorescent light source and a DP72 color CCD camera. Samples were excited with UV light by respective Chroma band-pass (350/50) and dichroic (380DCLP) filters and emission was collected with a Chroma cut-off filter from 500 nm (E515LPv2).

## Scanning electron microscopy (SEM)

Scanning electron microscopy (SEM) images were taken with a Hitachi S-4800 microscope working at 15 kV in the Analytic and High Resolution Microscopy in Biomedicine Service (SGIker) of the University of the Basque Country (UPV/EHU).

For bacterial visualization, samples were fixed with 2% glutaraldehyde and washed three times with 0.01 M PBS and 2 times with MilliQ water filtered with 0.1 µm pore size filters. Samples were deposited in conductive Si substrate, dried under infrared radiation, and covered with gold under argon atmosphere.

In the case of eukaryotic cells, A549 cells were directly cultured on sterile microscopy coverslips inserted in culture plates. The coverslips with attached cells were fixed by immersion in 0.1 M Sorensen's phosphate buffer (pH 7.4) with 2% glutaraldehyde for 2 hours at room temperature. Next, three washings were performed with 0.1 M Sorensen's phosphate buffer (pH 7.4) and a subsequent series of dehydration steps by increasing ethanol concentrations (from 30% until 100%) were carried out. The last dehydration step was performed with hexamethyldisilazane and the coverslips were left to dry at room temperature. Before microscope observations, cells were covered with gold under argon atmosphere. In order to better distinguish MTB/magnetosomes from cellular membrane structures, the images were colored using GIMP software.

## Transmission electron microscopy (TEM)

Transmission electron microscopy (TEM) images were acquired with a JEOL JEM-1400 Plus electron microscope at an accelerating voltage of 120 kV in the Analytic and High Resolution Microscopy in Biomedicine Service (SGIker) of the University of the Basque Country (UPV/EHU).

For bacterial visualization, samples were fixed with 2% glutaraldehyde and washed three times with 0.01 M PBS and 2 times with MilliQ water filtered with 0.1 µm pore size filters. A concentration of $\sim 10^8$ bacteria $mL^{-1}$ was used. Samples were deposited onto 300 mesh carbon-coated grids for observation. Isolated magnetosomes were directly deposited onto the grids at a concentra-

tion of ∼40 µg $mL^{-1}$ suspended in MilliQ water. FIJI software was used for magnetosome and bacterial size determination.

For eukaryotic cell visualization, cells were pre-fixed with 0.5% glutaraldehyde in the culture media for 15 minutes. Then, they were detached from the culture flasks with cell scrapers and centrifuged to remove the culture media. Cells were further fixed in 0.1 M Sorensen's phosphate buffer (pH 7.4) with 2% glutaraldehyde for 2 hours at room temperature. Afterwards, cells were washed several times with isoosmolar phosphate/sucrose buffer, dehydrated through an increasing ethanol concentration series (from 30% until 100%) and embedded in Epon Polarbed resin in beam capsules that polymerized at 55 °C in 48 hours. A Leica UCT ultramicrotome with a Diatome diamond knife was used to obtain ultrathin sections of 70 nm that were finally deposited onto carbon-coated copper grids.

## Flow cytometry

Flow cytometry was used for bacterial and eukaryotic cell analysis and counting. The equipment used was a Beckman Coulter Gallios cytometer of the Analytic and High Resolution Microscopy in Biomedicine Service (SGIker) of the University of the Basque Country (UPV/EHU).

For bacterial counting, a commercial Bacterial Counting Kit (Invitrogen, B7277) containing SYTO BC bacteria stain and microspheres of a known concentration to calculate bacterial concentration was used following the manufacturer indications. SYTO BC is a green fluorescent dye and was excited with a blue laser of 488 nm and recorded in the FL1 channel (525/40 nm).

In eukaryotic cell analyses, in order to distinguish between living and dead cells, a viability kit containing Hoechst 33342 (Invitrogen, R37165) and propidium iodide (Invitrogen, R37169) was used following the manufacturer indications. Hoechst 33342 is a blue fluorescent membrane-permeable dye that links to DNA staining cell nuclei and allowing the differentiation of cells from other possible debris. It was excited with a violet laser of 405 nm and recorded in the FL9 channel (450/50 nm). Propidium iodide is a red fluorescent stain that also links to DNA but can only penetrate the cells when their membranes are damaged, therefore staining only dead cells. It was excited with a blue

laser (488 nm) and recorded in the FL3 channel (620/20 nm). To estimate cell concentration, commercial fluorescent beads from a known concentration were used (BD Trucount$^{TM}$ Tubes, 340334).

## Magnetosome isolation

For magnetosome extraction and purification, bacteria were harvested by centrifugation (8000 g, 15 minutes, 4 °C) after 72 hours of culture. The pellet was resuspended in 10 mL $g^{-1}$ of 20 mM HEPES - 4 mM EDTA (pH 7.4) buffer. Bacteria were disrupted by French Press (GlenMills) applying 1250 psig pressure. This step was repeated two times per sample to ensure cell disruption. Cell lysate was sonicated (40 W, 45 cycles of 15 s ON - 5 s OFF) at 4 °C to further segregate cell debris from magnetosomes. Magnetosomes were separated from other non-magnetic debris by a magnetic rack and resuspended in 10 mM HEPES - 200 mM NaCl (pH 7.4) buffer. Magnetosome suspension was further sonicated (40 W, 45 cycles of 15 s ON - 5 s OFF) at 4 °C and the magnetic rack washing was repeated. This step of sonicating and washing was performed three times. Finally, magnetosomes were collected in 1 mL MilliQ water and stored at 4 °C.

## Inductively coupled plasma (ICP)

To determine the concentration of iron and other elements, samples were digested with concentrated nitric acid and analyzed by inductively coupled plasma atomic emission spectroscopy (ICP-AES), mass spectrometry (ICP-MS), and optical emission spectroscopy (ICP-OES).

In *Chapter 3* and *Chapter 5* the samples were analyzed in the Spectrometry Central Analysis Service (SGIker) of the University of the Basque Country (UPV/EHU). The iron concentration was analyzed by ICP-AES (Agilent, 5110) and the other elements measured in *Chapter 5* were analyzed by ICP-MS (Agilent, 7700). ICP analyses presented in *Chapter 4* were performed by Dr. Sandra Prévéral in BIAM, CEA Cadarache (France) with ICP-OES (Agilent, 5100).

# Magnetic measurements

Magnetic measurements were performed on a superconducting quantum interference device magnetometer (SQUID, Quantum Design MPMS3) in DC mode and on a vibrating sample magnetometer (VSM) equipped with a conventional electromagnet producing a magnetic field of up to 1.8 T that belong to the Magnetic Measurements Service (SGIker) of the University of the Basque Country (UPV/EHU). MTB, magnetosomes and eukaryotic cells containing MTB/magnetosomes were measured either in pellets obtained by centrifugation or freeze-dried.

In *Chapter 1* and *Chapter 2*, the mass of magnetite of the samples was obtained from the saturation magnetic moment, $m_s$, of the hysteresis loops measured at room temperature and the saturation magnetization of magnetite ($M_s(Fe_3O_4)$ = 92 A $m^2$ $kg^{-1}$) by using Equation 1:

$$m_{Fe_3O_4} = \frac{m_s(\text{A m}^2)}{92 \text{ A m}^2 \text{ kg}^{-1}} \quad (1)$$

In Figure 1 an example hysteresis loop of a magnetosome-loaded A549 cell culture containing 8 × $10^5$ cells is displayed. The measured signal (black) corresponds to the whole sample that includes the strong ferrimagnetic signal of magnetite together with a weak linear contribution of the cells and the sample holder. To calculate the saturation magnetic moment, $m_s$, the linear contribution (blue line) was substracted (red line). In the example shown in Figure 1, the mass of magnetite is ≈ 30 µg which corresponds to ≈ 38 pg of magnetite per cell.

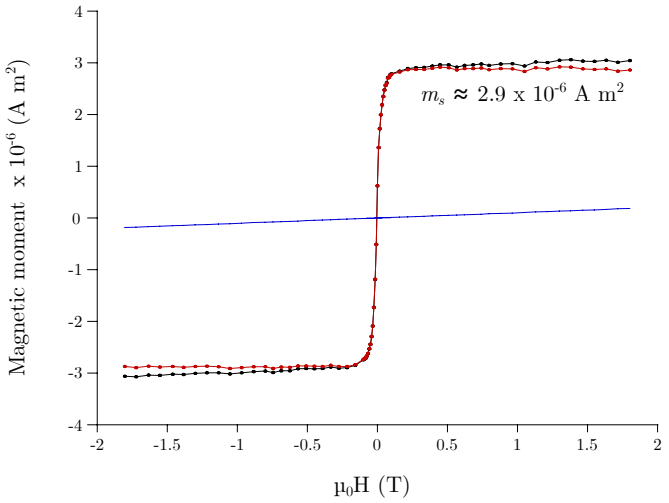


Figure 1: Hysteresis loop of a sample containing $8 \times 10^5$ magnetosome-loaded A549 cells (black). The red line represents the corrected signal (without the linear contribution of organic material of cells and the sample holder (blue)).

In *Chapter 4* and *Chapter 5*, zero field cooling/field cooling (ZFC/FC) magnetization curves were measured by SQUID magnetometry in freeze dried samples. Measurements were performed in DC mode, cooling the samples from 300 K to 5 K without an applied magnetic field. At 5 K, a magnetic field of 5 mT was applied and the magnetic moment was measured while temperature increased until 300 K (ZFC). Without removing the magnetic field, the sample was cooled again to 5 K and its magnetic moment was measured again upon warming to 300 K (FC).

## Magnetic hyperthermia

In *Chapter 2*, the alternating magnetic field (AMF) application during the *in vitro* hyperthermia experiments was performed by an UltraFlex Power Technologies (SH-2/350) apparatus. Cell culture wells were directly introduced inside the coil three by three (Figure 2) and their position was alternated every 15 minutes to avoid any differences due to heterogeneity of the AMF. The alternating magnetic field was applied for a total of 45 minutes with a frequency of 150 kHz and an amplitude of 31.8 kA $m^{-1}$ (400 Oe).

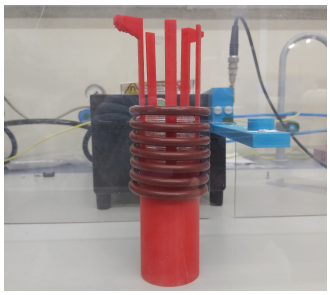

Figure 2: Cell culture wells inside magnetic coil used for AMF application in the *in vitro* magnetic hyperthermia study.

## *Ex cellulo* magnetosome degradation in citrate buffer

The *ex cellulo* magnetosome degradation experiments presented in *Chapter 3* were performed by maintaining 50 µg of magnetosomes in citrate buffer (0.1 M, pH 4.5) at 37 °C. The citrate buffer was obtained by mixing:

| | |
|---|---|
| Sodium citrate · $2H_2O$ | 2.703 g |
| Citric acid | 2.077 g |
| Distilled water | 200 mL |

The buffer was sterilized by filtration.

After certain days of incubation, samples were frozen at -80 °C to stop the degradation reaction and freeze dried. The obtained powder was mixed with boron nitride (Alfa Aesar, 11078) and compacted in 5 mm pills to be measured in the synchrotron.

## X-ray absorption near-edge structure (XANES)

For the XANES experiments presented in *Chapter 3*, cells were detached from culture plates with 0.01 M PBS - 4 mM EDTA and fixed with 2% glutaralde-

hyde. Pellets obtained by centrifugation were freeze dried and enclosed in kapton foil.

XANES experiments were performed on the Fe K-edge (7112 eV) at the BL22 - CLÆSS beamline of the ALBA synchrotron (Spain) and at the BM23 beamline of the ESRF synchrotron (France). Samples were measured in fluorescence yield mode at low temperatures (77 K in ALBA, 10 K in ESRF) to avoid radiation damage. The monochromator used in both experiments was a double Si crystal oriented in the (111) direction. XANES spectra were measured up to k = 9 $Å^{-1}$. Reference samples such as horse spleen ferritin (HoSF, (Sigma-Aldrich, F7879), control bacteria, maghemite) were measured in transmission configuration.

In the case of magnetosome degradation in citrate buffer, samples were freeze dried and mixed with boron nitride to make 5 mm pellets. Fe K-edge XANES spectra of the samples were measured in the XAFS beamline at Elettra synchrotron (Italy). Measurements were performed at room temperature and in transmission configuration up to k = 9 $Å^{-1}$ using a double Si crystal oriented in the (111) direction. Together with the usual Fe standards, the boron nitride was measured in fluorescence yield mode as it has a Fe content whose Fe K-edge XANES spectrum was included in the linear combination fits of the samples. The Fe atomic fraction of the boron nitride obtained from the linear combination fits ranged between 0.13 and 0.26.

In *Chapter 4* Tb-MSR-1 and Gd-MSR-1 and the isolated Tb-magnetosomes and Gd-magnetosomes were measured in the Fe K-edge and in Tb $L_3$ (7514 eV) and Gd $L_3$ (7243 eV) edges. Bacteria were collected by centrifugation (8000 g, 15 minutes, 4 °C) after 48 hours of culture. The obtained pellets were freeze dried and compacted in 5 mm pills containing $\sim 2 \times 10^9$ bacteria. Isolated magnetosomes were freeze dried and 2 mg of the obtained powder were mixed with 20 mg of boron nitride. The mixture was compacted into 5 mm pills.

The XANES spectra of the samples were collected at room temperature at the BL22-CLÆSS beamline of the ALBA syncrotron facility (Spain) using a double Si crystal oriented in the (111) direction as the monochromator. Measurements on the Fe K-edge and Tb $L_3$-edge were performed in transmission configuration whereas the Gd $L_3$-edge spectra were collected in fluorescence yield mode. Gd standards ($GdCl_3$ (Sigma-Aldrich, 203289) and $Gd_2O_3$ (Alpha-Aesar, 11289)) were measured in transmission configuration, and the

Tb standard $(TbNO_3)_3$ spectrum was kindly provided by Dr. Aida Serrano.

The experimental spectra were normalized using standard procedures for background subtraction and data normalization as implemented in the free software Athena of the IFEFFIT package [173, 174]. The linear combination fits to known standards were also implemented with the Athena software. The refinement was performed by minimizing the square residual in which the sum runs over the experimental points: $\chi^2 = \sum_i (\mu_i^{exp} - \mu_i^{theo})^2$ where $\mu^{\text{exp}}$ and $\mu^{\text{theo}}$ are the experimental and fitted data, respectively. The fits were considered to be reliable when they presented a $\chi^2 < 0.05$.

## Estimation of the mass of Fe by means of magnetometry and XANES

The mass of Fe in the magnetosome-loaded cells of *Chapter 3* was estimated by means of the combination of the atomic fraction of Fe in each phase obtained from XANES and the saturation magnetic moment, $m_s$, of the hysteresis loops.

Considering that there are three iron phases in the samples (magnetite, maghemite and ferrihydrite), the mass of Fe in the sample, $m_{Fe}$, is given by:

$$m_{Fe} = m_{Fe,magn} + m_{Fe,magh} + m_{Fe,fh} \tag{2}$$

From the linear combination fitting of XANES spectra, the atomic fraction of Fe in each phase is obtained: $\alpha_{magn}$, $\alpha_{magh}$ and $\alpha_{fh}$. Therefore, the Fe mass in each phase is given by:

$$\begin{aligned} m_{Fe,magn} &= \alpha_{magn} \times m_{Fe} \\ m_{Fe,magh} &= \alpha_{magh} \times m_{Fe} \\ m_{Fe,fh} &= \alpha_{fh} \times m_{Fe} \end{aligned} \tag{3}$$

$m_{Fe,magn}$ and $m_{Fe,magh}$ can be estimated from the combination of the atomic fractions obtained by XANES and the hysteresis loops because only magnetite

and maghemite contribute to the saturation magnetic moment, $m_s$. Magnetite contributes with 92 A $m^2$ $kg^{-1}$ and maghemite contributes with 76 A $m^2$ $kg^{-1}$. Since the mass fraction of Fe in magnetite and maghemite is 72% and 70%, respectively, the saturation magnetic moment per mass of Fe is 127.8 A $m^2$ $kg^{-1}$Fe for magnetite and 108.6 A $m^2$ $kg^{-1}$Fe for maghemite.

From XANES, the atomic fraction of Fe in the magnetic phases (magnetite and maghemite) is given by:

$$x_{magn} = \frac{\alpha_{magn}}{\alpha_{magn} + \alpha_{magh}} \quad \text{and} \quad x_{magh} = 1 - x_{magn} = \frac{\alpha_{magh}}{\alpha_{magn} + \alpha_{magh}} \tag{4}$$

Therefore, the mass of Fe in each magnetic phase can be calculated as:

$$\begin{aligned} m_{Fe,magn} &= \frac{x_{magn}}{x_{magn} \times 127.8 + x_{magh} \times 108.6} \times m_s \\ m_{Fe,magh} &= \frac{x_{magh}}{x_{magn} \times 127.8 + x_{magh} \times 108.6} \times m_s \end{aligned} \tag{5}$$

From Equations 3 the mass of iron in ferrihydrite can be calculated as:

$$m_{Fe,fh} = \frac{\alpha_{fh}}{\alpha_{magn}} \times m_{Fe,magn} \quad \text{or} \quad m_{Fe,fh} = \frac{\alpha_{fh}}{\alpha_{magh}} \times m_{Fe,magh} \tag{6}$$

The total mass of Fe in the sample, $m_{Fe}$, can be calculated using Equation 2.

The same reasoning applies when the sample contains goethite instead of ferrihydrite.

The error of $m_{Fe}$ has been estimated by error propagation considering a $\pm$ 0.1 indetermination in the obtained atomic fractions [33].

# Rare earth sensitivity curves

In *Chapter 4*, the sensitivity analysis of *M. gryphiswaldense* to terbium and gadolinium was performed in 96-well plates with serial dilutions of terbium(III)-quinate and gadolinium(III)-quinate (0 – 500 µM) made in FSM medium. Bacteria grown in FSM were harvested at the early stationary phase and inoculated in the well plate at a concentration of $10^6$ cell $mL^{-1}$. After 72 hours of incubation at 28 °C the bacterial growth was determined by optical density (600 nm).

# Fluorimetry

In *Chapter 4*, fluorescence measurements of Tb-MSR-1 and Tb-magnetosomes were performed in a spectrofluorimeter Edinburgh Instruments (FLSP 920 model) with a xenon flash lamp 450 W as the excitation source. The samples, in 1 cm optical path cuvettes in right-angle configuration, were excited with a $\lambda_{ex}$ = 285 nm and the spectra were recorded at a $\lambda_{em}$ = 520 - 570 nm. For the culture medium not to interfere in the fluorescence experiments, cells where washed prior to the experiments three times with 10 mM HEPES - 10 mM EDTA (to remove Tb precipitates) and two times with MilliQ water.

In *Chapter 5*, fluorescence of MSR-1-Venus-RGD and AMB-1-Venus-RGD bacteria and magnetosomes was measured in an Infinite®M200 (Tecan) well plate reader. Samples were washed to remove the culture media and resuspended in 0.01 mM PBS buffer. Samples were excited with a $\lambda_{ex}$ = 470 nm and the spectra were recorded at a $\lambda_{em}$ = 505 - 569 nm.

# Genetic modification procedure

## WM3064 transformation with *pBBR-mamC-Venus-RGD*

In *Chapter 5*, The transformation of *E. coli* WM3064 with the plasmid *pBBR-mamC-Venus-RGD* (kindly provided by Dr. Sandra Prévéral) [52] was performed by electroporation. For this, 100 mL of WM3064 culture in exponential growth phase ($OD_{600nm}$ = 0.6 - 0.8) were centrifuged (3000 rpm, 15 minutes).

A series of 5 washings with MilliQ water kept at 4 °C were performed and the final pellet was resuspended in 1 mL of MilliQ water.

An aliquot of 50 µL of the WM3064 suspension was mixed with 2 µL of the plasmid stored in nuclease-free water at a concentration between 5 - 50 ng DNA $mL^{-1}$. The mixture was transferred to an electroporation cuvette and one shock of 1700 V was applied. The transformed bacteria were incubated in SOC medium (Invitrogen, 15544034) for 1 hour at 37 °C and then in LB agar plates supplemented with 0.3 mM diaminopimelic acid (DAP) and 50 µg mL kanamycin overnight at 37 °C. The successful result of the transformation procedure was verified by fluorescence microscopy. The obtained colonies were transferred to LB broth (+ 0.3 mM DAP + 50 µg mL kanamycin).

## Mobilization of plasmid *pBBR-mamC-Venus-RGD* into *Magnetospirillum* spp.

*pBBR-mamC-Venus-RGD* plasmid was mobilized to *M. gryphiswaldense* and *M. magneticum* by conjugation. The cultures of *Magnetospirillum* spp. and WM3064 were collected in exponential growth phase ($OD_{600nm} \approx 0.2$) and mixed. For this, 500 µL of WM3064, 5 mL of *M. gryphiswaldense* and 30 mL of *M. magneticum* cultures were centrifuged and resuspended in 20 µL of FSM medium for WM3064 and *M. gryphiswaldense* conjugation and MSGM medium for WM3064 and *M. magneticum* conjugation. In both cases the media was supplemented with DAP (0.3 mM). The suspensions containing WM3064 + *M. gryphiswaldense* and WM3064 + *M. magneticum* were inoculated in agar plates with FSM or MSGM, respectively, supplemented with DAP (0.3 mM) and the plates were incubated in microaerobiosis (2% $O_2$) at 28 °C for 5 h.

For the selection of recombinant *Magnetospirillum* spp., the obtained colonies were transferred to agar plates without DAP and supplemented with kanamycin (10 µg $mL^{-1}$). They were incubated in microaerobiosis (2% $O_2$) at 28 °C for 7 days.

The colonies confirmed as recombinant were inoculated in FSM (*M. gryphiswaldense*) and MSGM (*M. magneticum*) liquid media supplemented with kanamycin (10 µg $mL^{-1}$) to make stocks.

## Electrophoresis (SDS-PAGE) and Western blot

In *Chapter 5*, the verification of the constructor expression by MSR-1-Venus-RGD and AMB-1-Venus-RGD was performed by electrophoresis in 10% polyacrylamide gel (NuPAGE™, Bis-Tris at 10%, Invitrogen, NP0301BOX) and a subsequent Western blot analysis. 22.5 µL containing ∼1.5 mg $mL^{-1}$ of magnetosomes (for the NuPAGE) and ∼0.15 mg $mL^{-1}$ of magnetosomes (for the Western blot) were treated with 7.5 µL LDS Sample Buffer (4×) (Invitrogen, B0008) at 95 °C for 15 minutes.

For NuPAGE, the gel was charged and run at 80 V for 30 minutes and at 100 V for 1 hour in MOPS SDS (1×) NuPAGE™Running Buffer (Invitrogen, NP0001). Precision Plus Protein™All Blue Prestained Protein Standards (Bio-Rad, 1610373) was used as a molecular weight marker. Previous to observation, the protein gel was incubated with Imperial™Protein Stain (Thermo Scientific, 24615) for 2 hours and washed overnight with distilled water.

For the Western blot, the transference from the polyacrylamide gel to a nitrocellulose membrane was performed at 4 °C and 100 V for 1.5 hours. The transfer buffer was MOPS SDS (1×) NuPAGE™Running Buffer (Invitrogen, NP0001) - 20% ethanol. The nitrocellulose membrane was incubated in a milk solution containing TBS (1×) - 0.01% Tween20® after what the primary anti-Venus antibody (Living Colors® A.v. Monoclonal Antibody JL-8, Clontech) was added and incubated overnight at 4 °C. The membrane was washed for 10 minutes with TBS (1×) - 0.01% Tween20® three times and incubated with the secondary antibody (anti-mouse HRP IgG-Peroxidase antibody, Sigma-Aldrich, A9044) diluted in milk with TBS (1×) - 0.01% Tween20®. After 3×10 minute washings of the membrane, it was revealed by adding 2 mL of Immobilion® Western Chemiluminiscent HRP Substrate (Millipore, WBKLS0100). The images were taken by the Western blot imaging system G:Box with the program SynGene.

## Statistical analysis

Statistical analyses was performed using Student's t test to compare mean values between groups. Differences were considered statistically significant at a probability value of $P < 0.05$.

# Bibliography


[1] D. A. Bazylinski and R. B. Frankel, "Magnetosome formation in prokaryotes," *Nature Reviews Microbiology*, vol. 2, no. 3, pp. 217–230, 2004.

[2] D. Faivre and D. Schüler, "Magnetotactic bacteria and magnetosomes," *Chemical Reviews*, vol. 108, no. 11, pp. 4875–4898, 2008.

[3] D. A. Bazylinski, C. Lefèvre, and D. Schüler, "Magnetotactic bacteria," in *The Prokaryotes* (E. Rosenberg, E. F. DeLong, S. Lory, E. Stackebrandt, and F. Thompson, eds.), pp. 453–494, Springer, Berlin, Heidelberg, 2013.

[4] D. A. Bazylinski, C. T. Lefèvre, and B. H. Lower, "Magnetotactic bacteria, magnetosomes, and nanotechnology," in *Nanomicrobiology* (L. L. Barton, D. A. Bazylinski, and H. Xu, eds.), pp. 39–74, Springer, New York, NY, 2014.

[5] S. Bellini, "Su di un particolare comportamento di batteri d'acqua dolce," *Istituto Di Microbiologia Dell'Università Di Pavia*, pp. 3–7, 1963.

[6] S. Bellini, "Ulteriori studi sui "batteri magnetosensibili"," *Istituto Di Microbiologia Dell'Università Di Pavia*, pp. 3–15, 1963.

[7] S. Bellini, "On a unique behavior of freshwater bacteria," *Chinese Journal of Oceanology and Limnology*, vol. 27, no. 1, pp. 3–5, 2009.

[8] S. Bellini, "Further studies on "magnetosensitive bacteria"," *Chinese Journal of Oceanology and Limnology*, vol. 27, no. 1, pp. 6–12, 2009.

[9] R. Blakemore, "Magnetotactic bacteria," *Science*, vol. 190, no. 4212, pp. 377–379, 1975.

[10] W. Lin, Y. Pan, and D. A. Bazylinski, "Diversity and ecology of and biomineralization by magnetotactic bacteria," *Environmental Microbiology Reports*, vol. 9, no. 4, pp. 345–356, 2017.

[11] C. T. Lefèvre and D. A. Bazylinski, "Ecology, diversity, and evolution of magnetotactic bacteria," *Microbiology and Molecular Biology Reviews*, vol. 77, no. 3, pp. 497–526, 2013.

[12] S. Kolinko, C. Jogler, E. Katzmann, G. Wanner, J. Peplies, and D. Schüler, "Single-cell analysis reveals a novel uncultivated magnetotactic bacterium within the candidate division OP3," *Environmental Microbiology*, vol. 14, no. 7, pp. 1709–1721, 2012.

[13] F. Abreu, J. L. Martins, T. Souza Silveira, C. Neumann Keim, H. G. P. Lins de Barros, F. J. Gueiros Filho, and U. Lins, "'*Candidatus* Magnetoglobus multicellularis', a multicellular, magnetotactic prokaryote from a hypersaline environment," *International Journal of Systematic and Evolutionary Microbiology*, vol. 57, no. Pt 6, pp. 1318–1322, 2007.

[14] C. T. Lefèvre, R. B. Frankel, M. Pósfai, T. Prozorov, and D. A. Bazylinski, "Isolation of obligately alkaliphilic magnetotactic bacteria from extremely alkaline environments," *Environmental Microbiology*, vol. 13, no. 8, pp. 2342–2350, 2011.

[15] C. T. Lefèvre, F. Abreu, M. L. Schmidt, U. Lins, R. B. Frankel, B. P. Hedlund, and D. A. Bazylinski, "Moderately thermophilic magnetotactic bacteria from hot springs in Nevada," *Applied and Environmental Microbiology*, vol. 76, no. 11, pp. 3740–3743, 2010.

[16] A. C. V. Araujo, F. Abreu, K. T. Silva, D. A. Bazylinski, and U. Lins, "Magnetotactic bacteria as potential sources of bioproducts," *Marine Drugs*, vol. 13, pp. 389–430, 2015.

[17] D. Schüler and R. B. Frankel, "Bacterial magnetosomes: microbiology, biomineralization and biotechnological applications," *Applied Microbiology and Biotechnology*, vol. 52, no. 4, pp. 464–473, 1999.

[18] R. Uebe and D. Schüler, "Magnetosome biogenesis in magnetotactic bacteria," *Nature Reviews Microbiology*, vol. 14, no. 10, pp. 621–637, 2016.

[19] R. B. Frankel, D. A. Bazylinski, M. S. Johnson, and B. L. Taylor, "Magneto-aerotaxis in marine coccoid bacteria," *Biophysical Journal*, vol. 73, no. 2, pp. 994–1000, 1997.

[20] R. B. Frankel, T. J. Williams, and D. A. Bazylinski, "Magneto-aerotaxis," in *Magnetoreception and Magnetosomes in Bacteria* (D. Schüler, ed.), vol. 3, pp. 1–24, Springer, Berlin, Heidelberg, 2006.

[21] R. B. Frankel and D. A. Bazylinski, "Magnetosomes and magneto-aerotaxis," *Contributions to Microbiology*, vol. 16, pp. 182–193, 2009.

[22] D. Muñoz, L. Marcano, R. Martín-Rodríguez, L. Simonelli, A. Serrano, A. García-Prieto, M. L. Fdez-Gubieda, and A. Muela, "Magnetosomes could be protective shields against metal stress in magnetotactic bacteria," *Scientific Reports*, vol. 10, p. 11430, 2020.

[23] F. F. Guo, W. Yang, W. Jiang, S. Geng, T. Peng, and J. L. Li, "Magnetosomes eliminate intracellular reactive oxygen species in *Magnetospirillum gryphiswaldense* MSR-1," *Environmental Microbiology*, vol. 14, no. 7, pp. 1722–1729, 2012.

[24] R. B. Frankel, "Magnetic guidance of organisms," *Annual Review of Biophysics and Bioengineering*, vol. 13, pp. 85–103, 1984.

[25] D. Schüler, "Genetics and cell biology of magnetosome formation in magnetotactic bacteria," *FEMS Microbiology Reviews*, vol. 32, no. 4, pp. 654–672, 2008.

[26] A. Komeili, "Molecular mechanisms of compartmentalization and biomineralization in magnetotactic bacteria," *FEMS Microbiology Reviews*, vol. 36, pp. 232–255, 2012.

[27] A. Komeili, Z. Li, D. K. Newman, and G. J. Jensen, "Magnetosomes are cell membrane invaginations organized by the actin-like protein MamK," *Science*, vol. 311, no. 5758, pp. 242–245, 2006.

[28] A. Komeili, H. Vali, T. J. Beveridge, and D. K. Newman, "Magnetosome vesicles are present before magnetite formation, and MamA is required for their activation," *Proceedings of the National Academy of Sciences of the United States of America*, vol. 101, no. 11, pp. 3839–3844, 2004.

[29] R. B. Frankel and R. P. Blakemore, "Navigational compass in magnetic bacteria," *Journal of Magnetism and Magnetic Materials*, vol. 15-18, no. Part 3, pp. 1562–1564, 1980.

[30] E. Katzmann, A. Scheffel, M. Gruska, J. M. Plitzko, and D. Schüler, "Loss of the actin-like protein MamK has pleiotropic effects on magnetosome formation and chain assembly in *Magnetospirillum gryphiswaldense*," *Molecular Microbiology*, vol. 77, no. 1, pp. 208–224, 2010.

[31] I. Orue, L. Marcano, P. Bender, A. García-Prieto, S. Valencia, M. A. Mawass, D. Gil-Cartón, D. Alba Venero, D. Honecker, A. García-Arribas, L. Fernández Barquín, A. Muela, and M. L. Fdez-Gubieda, "Configuration of the magnetosome chain: a natural magnetic nanoarchitecture," *Nanoscale*, vol. 10, no. 16, pp. 7407–7419, 2018.

[32] K. H. Schleifer, D. Schüler, S. Spring, M. Weizenegger, R. Amann, W. Ludwig, and M. Köhler, "The genus *Magnetospirillum* gen. nov. description of *Magnetospirillum gryphiswaldense* sp. nov. and transfer of *Aquaspirillum magnetotacticum* to *Magnetospirillum magnetotacticum* comb. nov.," *Systematic and Applied Microbiology*, vol. 14, no. 4, pp. 379–385, 1991.

[33] M. L. Fdez-Gubieda, A. Muela, J. Alonso, A. García-Prieto, L. Olivi, R. Fernández-Pacheco, and J. M. Barandiarán, "Magnetite biomineralization in *Magnetospirillum gryphiswaldense*: time-resolved magnetic and structural studies," *ACS Nano*, vol. 7, no. 4, pp. 3297–3305, 2013.

[34] L. Marcano, A. García-Prieto, D. Muñoz, L. Fernández Barquín, I. Orue, J. Alonso, A. Muela, and M. L. Fdez-Gubieda, "Influence of the bacterial growth phase on the magnetic properties of magnetosomes synthesized by *Magnetospirillum gryphiswaldense*," *Biochimica et Biophysica Acta - General Subjects*, vol. 1861, no. 6, pp. 1507–1514, 2017.

[35] L. Marcano, I. Orue, A. García-Prieto, R. Abrudan, J. Alonso, L. Fernández Barquín, S. Valencia, A. Muela, and M. L. Fdez-Gubieda, "Controlled magnetic anisotropy in single domain Mn-doped biosynthesized nanoparticles," *Journal of Physical Chemistry C*, vol. 124, no. 41, pp. 22827–22838, 2020.

[36] L. Marcano, D. Munoz, R. Martín-Rodríguez, I. Orue, J. Alonso, A. García-Prieto, A. Serrano, S. Valencia, R. Abrudan, L. Fernández Barquín, A. García-Arribas, A. Muela, and M. L. Fdez-Gubieda, "Magnetic study of Co-doped magnetosome chains," *Journal of Physical Chemistry C*, vol. 122, no. 13, pp. 7541–7550, 2018.

[37] A. Muela, D. Muñoz, R. Martín-Rodríguez, I. Orue, E. Garaio, A. Abad Díaz de Cerio, J. Alonso, J. Á. García, and M. L. Fdez-Gubieda, "Optimal parameters for hyperthermia treatment using biomineralized magnetite nanoparticles: theoretical and experimental approach," *The Journal of Physical Chemistry C*, vol. 120, no. 42, pp. 24437–24448, 2016.

[38] D. A. Bazylinski and S. Schübbe, "Controlled biomineralization by and applications of magnetotactic bacteria," *Advances in Applied Microbiology*, vol. 62, pp. 21–62, 2007.

[39] A. Arakaki, H. Nakazawa, M. Nemoto, T. Mori, and T. Matsunaga, "Formation of magnetite by bacteria and its application," *Journal of the Royal Society Interface*, vol. 5, no. 26, pp. 977–999, 2008.

[40] E. Alphandéry, "Applications of magnetosomes synthesized by magnetotactic bacteria in medicine," *Frontiers in Bioengineering and Biotechnology*, vol. 2, no. 5, 2014.

[41] G. Vargas, J. Cypriano, T. Correa, P. Leão, D. A. Bazylinski, and F. Abreu, "Applications of magnetotactic bacteria, magnetosomes and magnetosome crystals in biotechnology and nanotechnology: mini-review," *Molecules*, vol. 23, no. 10, p. 2438, 2018.

[42] D. Ortega and Q. A. Pankhurst, "Magnetic hyperthermia," in *Nanoscience* (P. O'Brien, ed.), vol. 1, pp. 60–88, The Royal Society of Chemistry, 2012.

[43] C. Binns, "Magnetic nanoparticle hyperthermia treatment of tumours," in *Nanostructured Materials for Magnetoelectronics* (B. Aktaş and F. Mikailzade, eds.), vol. 175, pp. 197–215, Springer, Berlin, Heidelberg, 2013.

[44] T. Orlando, S. Mannucci, E. Fantechi, G. Conti, S. Tambalo, A. Busato, C. Innocenti, L. Ghin, R. Bassi, P. Arosio, F. Orsini, C. Sangregorio, M. Corti, M. F. Casula, P. Marzola, A. Lascialfari, and A. Sbarbati, "Characterization of magnetic nanoparticles from *Magnetospirillum gryphiswaldense* as potential theranostics tools," *Contrast Media & Molecular Imaging*, vol. 11, no. 2, pp. 139–145, 2016.

[45] E. Alphandéry, I. Chebbi, F. Guyot, and M. Durand-Dubief, "Use of bacterial magnetosomes in the magnetic hyperthermia treatment of tumours: a review.," *International Journal of Hyperthermia*, vol. 29, no. 8, pp. 801–809, 2013.

[46] M. Timko, A. Dzarova, J. Kovac, A. Skumiel, A. Józefczak, T. Hornowski, H. Gojżewski, V. Zavisova, M. Koneracka, A. Sprincova, O. Strbak, P. Kopcansky, and N. Tomasovicova, "Magnetic properties and heating effect in bacterial magnetic nanoparticles," *Journal of Magnetism and Magnetic Materials*, vol. 321, no. 10, pp. 1521–1524, 2009.

[47] R. Hergt, R. Hiergeist, M. Zeisberger, D. Schüler, U. Heyen, I. Hilger, and W. A. Kaiser, "Magnetic properties of bacterial magnetosomes as potential diagnostic and therapeutic tools," *Journal of Magnetism and Magnetic Materials*, vol. 293, no. 1, pp. 80–86, 2005.

[48] S. Mannucci, S. Tambalo, G. Conti, L. Ghin, A. Milanese, A. Carboncino, E. Nicolato, M. R. Marinozzi, D. Benati, R. Bassi, P. Marzola, and A. Sbarbati, "Magnetosomes extracted from *Magnetospirillum gryphiswaldense* as theranostic agents in an experimental model of glioblastoma," *Contrast Media & Molecular Imaging*, vol. 2018, p. 2198703, 2018.

[49] E. Alphandéry, A. Idbaih, C. Adam, J. Y. Delattre, C. Schmitt, F. Guyot, and I. Chebbi, "Development of non-pyrogenic magnetosome minerals coated with poly-l-lysine leading to full disappearance of intracranial U87-Luc glioblastoma in 100% of treated mice using magnetic hyperthermia," *Biomaterials*, vol. 141, pp. 210–222, 2017.

[50] M. Colombo, S. Carregal-Romero, M. F. Casula, L. Gutiérrez, M. P. Morales, I. B. Böhm, J. T. Heverhagen, D. Prosperi, and W. J. Parak, "Biological applications of magnetic nanoparticles," *Chemical Society Reviews*, vol. 41, no. 11, pp. 4306–4334, 2012.

[51] S. Mériaux, M. Boucher, B. Marty, Y. Lalatonne, S. Prévéral, L. Motte, C. T. Lefèvre, F. Geffroy, F. Lethimonnier, M. Péan, D. Garcia, G. Adryanczyk-Perrier, D. Pignol, and N. Ginet, "Magnetosomes, biogenic magnetic nanomaterials for brain molecular imaging with 17.2 T MRI scanner," *Advanced Healthcare Materials*, vol. 4, no. 7, pp. 1076–1083, 2015.

[52] M. Boucher, F. Geffroy, S. Prévéral, L. Bellanger, E. Selingue, G. Adryanczyk-Perrier, M. Péan, C. T. Lefèvre, D. Pignol, N. Ginet, and S. Mériaux, "Genetically tailored magnetosomes used as MRI probe for molecular imaging of brain tumor," *Biomaterials*, vol. 121, pp. 167–178, 2017.

[53] Z. Xiang, X. Yang, J. Xu, W. Lai, Z. Wang, Z. Hu, J. Tian, L. Geng, and Q. Fang, "Tumor detection using magnetosome nanoparticles functionalized with a newly screened EGFR/HER2 targeting peptide," *Biomaterials*, vol. 115, pp. 53–64, 2017.

[54] X. Nan, W. Lai, D. Li, J. Tian, Z. Hu, and Q. Fang, "Biocompatibility of bacterial magnetosomes as MRI contrast agent: a long-term *in vivo* follow-up study," *Nanomaterials*, vol. 11, no. 5, p. 1235, 2021.

[55] A. Kraupner, D. Eberbeck, D. Heinke, R. Uebe, D. Schüler, and A. Briel, "Bacterial magnetosomes – nature's powerful contribution to MPI tracer research," *Nanoscale*, vol. 9, no. 18, pp. 5788–5793, 2017.

[56] O. Felfoul, M. Mohammadi, S. Taherkhani, D. De Lanauze, Y. Zhong Xu, D. Loghin, S. Essa, S. Jancik, D. Houle, M. Lafleur, L. Gaboury, M. Tabrizian, N. Kaou, M. Atkin, T. Vuong, G. Batist, N. Beauchemin, D. Radzioch, and S. Martel, "Magneto-aerotactic bacteria deliver drug-containing nanoliposomes to tumour hypoxic regions," *Nature Nanotechnology*, vol. 11, no. 11, pp. 941–947, 2016.

[57] Q. Deng, Y. Liu, S. Wang, M. Xie, S. Wu, A. Chen, and W. Wu, "Construction of a novel magnetic targeting anti-tumor drug delivery system: cytosine arabinoside-loaded bacterial magnetosome," *Materials*, vol. 6, no. 9, pp. 3755–3763, 2013.

[58] J. B. Sun, J. H. Duan, S. L. Dai, J. Ren, L. Guo, W. Jiang, and Y. Li, "Preparation and anti-tumor efficiency evaluation of doxorubicin-loaded bacterial magnetosomes: magnetic nanoparticles as drug carriers isolated from *Magnetospirillum gryphiswaldense*," *Biotechnology and Bioengineering*, vol. 101, no. 6, pp. 1313–1320, 2008.

[59] P. Ye, F. Li, J. Zou, Y. Luo, S. Wang, G. Lu, F. Zhang, C. Chen, J. Long, R. Jia, M. Shi, Y. Wang, X. Cheng, G. Ma, and W. Wei, "*In situ* generation of gold nanoparticles on bacteria-derived magnetosomes for imaging-guided starving/chemodynamic/photothermal synergistic therapy against cancer," *Advanced Functional Materials*, vol. 32, no. 17, p. 2110063, 2022.

[60] M. Hafsi, S. Prévéral, C. Hoog, J. Hérault, G. Adryanczyk-Perrier, C. T. Lefèvre, H. Michel, D. Pignol, J. Doyen, T. Pourcher, O. Humbert, J. Thariat, and B. Cambien, "RGD-functionalized magnetosomes are

efficient tumor radioenhancers for X-rays and protons," *Nanomedicine: Nanotechnology, Biology, and Medicine*, vol. 23, p. 102084, 2020.

[61] A. Plan Sangnier, S. Prévéral, A. Curcio, A. K. A. Silva, C. T. Lefèvre, D. Pignol, Y. Lalatonne, and C. Wilhelm, "Targeted thermal therapy with genetically engineered magnetite magnetosomes@RGD: photothermia is far more efficient than magnetic hyperthermia," *Journal of Controlled Release*, vol. 279, pp. 271–281, 2018.

[62] C. Lang and D. Schüler, "Expression of green fluorescent protein fused to magnetosome proteins in microaerophilic magnetotactic bacteria," *Applied and Environmental Microbiology*, vol. 74, no. 15, pp. 4944–4953, 2008.

[63] A. Pollithy, T. Romer, C. Lang, F. D. Müller, J. Helma, H. Leonhardt, U. Rothbauer, and D. Schüler, "Magnetosome expression of functional camelid antibody fragments (nanobodies) in *Magnetospirillum gryphiswaldense*," *Applied and Environmental Microbiology*, vol. 77, no. 17, pp. 6165–6171, 2011.

[64] D. Gandia, L. Gandarias, I. Rodrigo, J. Robles-García, R. Das, E. Garaio, J. Á. García, M. H. Phan, H. Srikanth, I. Orue, J. Alonso, A. Muela, and M. L. Fdez-Gubieda, "Unlocking the potential of magnetotactic bacteria as magnetic hyperthermia agents," *Small*, vol. 15, no. 41, p. 1902626, 2019.

[65] T. Zhang, H. Xu, J. Liu, Y. Pan, and C. Cao, "Determination of the heating efficiency of magnetotactic bacteria in alternating magnetic field," *Journal of Oceanology and Limnology*, vol. 39, no. 6, pp. 2116–2126, 2021.

[66] E. Alphandéry, S. Faure, O. Seksek, F. Guyot, and I. Chebbi, "Chains of magnetosomes extracted from AMB-1 magnetotactic bacteria for application in alternative magnetic field cancer therapy," *ACS Nano*, vol. 5, no. 8, pp. 6279–6296, 2011.

[67] C. Chen, L. Chen, Y. Yi, C. Chen, L. F. Wu, and T. Song, "Killing of *Staphylococcus aureus* via magnetic hyperthermia mediated by magnetotactic bacteria," *Applied and Environmental Microbiology*, vol. 82, no. 7, pp. 2219–2226, 2016.

[68] M. R. Benoit, D. Mayer, Y. Barak, I. Y. Chen, W. Hu, Z. Cheng, S. X. Wang, D. M. Spielman, S. S. Gambhir, and A. Matin, "Visualizing implanted tumors in mice with magnetic resonance imaging using magnetotactic bacteria," *Clinical Cancer Research*, vol. 15, no. 16, pp. 5170–5177, 2009.

[69] S. Wong and R. A. Slavcev, "Treating cancer with infection: a review on bacterial cancer therapy," *Letters in Applied Microbiology*, vol. 61, no. 2, pp. 107–112, 2015.

[70] W. B. Coley, "The treatment of inoperable sarcoma by bacterial toxins (the mixed toxins of the *Streptococcus erysipelas* and the *Bacillus prodigiosus*)," *Proceedings of the Royal Society of Medicine*, vol. 3, pp. 1–48, 1910.

[71] C. O. Starnes, "Coley's toxins in perspective," *Nature*, vol. 357, no. 6373, pp. 11–12, 1992.

[72] M. G. Kramer, M. Masner, F. A. Ferreira, and R. M. Hoffman, "Bacterial therapy of cancer: promises, limitations, and insights for future directions," *Frontiers in Microbiology*, vol. 9, no. 16, 2018.

[73] A. M. Kamat, T. W. Flaig, H. B. Grossman, B. Konety, D. Lamm, M. A. O'Donnell, E. Uchio, J. A. Efstathiou, and J. A. Taylor III, "Consensus statement on best practice management regarding the use of intravesical immunotherapy with BCG for bladder cancer," *Nature Reviews Urology*, vol. 12, no. 4, pp. 225–235, 2015.

[74] "ClinicalTrials.gov." https://clinicaltrials.gov/. Accesed: 2022-05-26.

[75] K. M. Tsoi, S. A. MacParland, X. Z. Ma, V. N. Spetzler, J. Echeverri, B. Ouyang, S. M. Fadel, E. A. Sykes, N. Goldaracena, J. M. Kaths, J. B. Conneely, B. A. Alman, M. Selzner, M. A. Ostrowski, O. A. Adeyi, A. Zilman, I. D. McGilvray, and W. C. W. Chan, "Mechanism of hard-nanomaterial clearance by the liver," *Nature Materials*, vol. 15, no. 11, pp. 1212–1221, 2016.

[76] J. J. Rennick, A. P. R. Johnston, and R. G. Parton, "Key principles and methods for studying the endocytosis of biological and nanoparticle therapeutics," *Nature Nanotechnology*, vol. 16, no. 3, pp. 266–276, 2021.

[77] G. Sahay, D. Y. Alakhova, and A. V. Kabanov, "Endocytosis of nanomedicines," *Journal of Controlled Release*, vol. 145, no. 3, pp. 182–195, 2010.

[78] J. J. Lim, S. Grinstein, and Z. Roth, "Diversity and versatility of phagocytosis: roles in innate immunity, tissue remodeling, and homeostasis," *Frontiers in Cellular and Infection Microbiology*, vol. 7, no. 191, 2017.

[79] D. Manzanares and V. Ceña, "Endocytosis: the nanoparticle and submicron nanocompounds gateway into the cell," *Pharmaceutics*, vol. 12, no. 4, p. 371, 2020.

[80] I. Khan and P. S. Steeg, "Endocytosis: a pivotal pathway for regulating metastasis," *British Journal of Cancer*, vol. 124, pp. 66–75, 2021.

[81] H. H. Li, J. Li, K. J. Wasserloos, C. Wallace, M. G. Sullivan, P. M. Bauer, D. B. Stolz, J. S. Lee, S. C. Watkins, C. M. St Croix, B. R. Pitt, and L. M. Zhang, "Caveolae-dependent and -independent uptake of albumin in cultured rodent pulmonary endothelial cells," *PLoS ONE*, vol. 8, no. 11, p. e81903, 2013.

[82] G. Sahay, E. V. Batrakova, and A. V. Kabanov, "Different internalization pathways of polymeric micelles and unimers and their effects on vesicular transport," *Bioconjugate Chemistry*, vol. 19, no. 10, pp. 2023–2029, 2008.

[83] J. A. Daniel, N. Chau, M. K. Abdel-Hamid, L. Hu, L. von Kleist, A. Whiting, S. Krishnan, P. Maamary, S. R. Joseph, F. Simpson, V. Haucke, A. McCluskey, and P. J. Robinson, "Phenothiazine-derived antipsychotic drugs inhibit dynamin and clathrin-mediated endocytosis," *Traffic*, vol. 16, no. 6, pp. 635–654, 2015.

[84] T. Li, K. Qin, N. Li, C. Han, and X. Cao, "An endosomal LAPF is required for macrophage endocytosis and elimination of bacteria," *Proceedings of the National Academy of Sciences of the United States of America*, vol. 116, no. 26, pp. 12958–12963, 2019.

[85] Y. Toduka, T. Toyooka, and Y. Ibuki, "Flow cytometric evaluation of nanoparticles using side-scattered light and reactive oxygen species-mediated fluorescence-correlation with genotoxicity," *Environmental Science and Technology*, vol. 46, no. 14, pp. 7629–7636, 2012.

[86] X. Duan and Y. Li, "Physicochemical characteristics of nanoparticles affect circulation, biodistribution, cellular internalization, and trafficking," *Small*, vol. 9, no. 9-10, pp. 1521–1532, 2013.

[87] P. Wang, C. Chen, C. Chen, Y. Li, W. Pan, and T. Song, "The interaction of bacterial magnetosomes and human liver cancer cells *in vitro*," *Journal of Magnetism and Magnetic Materials*, vol. 427, pp. 105–110, 2017.

[88] R. G. Parton, "Caveolae: structure, function, and relationship to disease," *Annual Review of Cell and Developmental Biology*, vol. 34, pp. 111–136, 2018.

[89] D. Egea-Benavente, J. G. Ovejero, M. P. Morales, and D. F. Barber, "Understanding MNPs behaviour in response to AMF in biological milieus and the effects at the cellular level: implications for a rational design that drives magnetic hyperthermia therapy toward clinical implementation," *Cancers*, vol. 13, no. 18, p. 4583, 2021.

[90] J. K. Kang, J. C. Kim, Y. Shin, S. M. Han, W. R. Won, J. Her, J. Y. Park, and K. T. Oh, "Principles and applications of nanomaterial-based hyperthermia in cancer therapy," *Archives of Pharmacal Research*, vol. 43, pp. 46–57, 2020.

[91] R. K. Gilchrist, R. Medal, W. D. Shorey, R. C. Hanselman, J. C. Parrott, and C. B. Taylor, "Selective inductive heating of lymph nodes," *Annals of Surgery*, vol. 146, no. 4, pp. 596–606, 1957.

[92] M. Johannsen, U. Gneveckow, L. Eckelt, A. Feussner, N. Waldöfner, R. Scholz, S. Deger, P. Wust, S. A. Loening, and A. Jordan, "Clinical hyperthermia of prostate cancer using magnetic nanoparticles: presentation of a new interstitial technique," *International Journal of Hyperthermia*, vol. 21, no. 7, pp. 637–647, 2005.

[93] K. Maier-Hauff, R. Rothe, R. Scholz, U. Gneveckow, P. Wust, B. Thiesen, A. Feussner, A. von Deimling, N. Waldoefner, R. Felix, and A. Jordan, "Intracranial thermotherapy using magnetic nanoparticles combined with external beam radiotherapy: results of a feasibility study on patients with glioblastoma multiforme," *Journal of Neuro-Oncology*, vol. 81, pp. 53–60, 2007.

[94] K. Maier-Hauff, F. Ulrich, D. Nestler, H. Niehoff, P. Wust, B. Thiesen, H. Orawa, V. Budach, and A. Jordan, "Efficacy and safety of intratumoral thermotherapy using magnetic iron-oxide nanoparticles combined with external beam radiotherapy on patients with recurrent glioblastoma multiforme," *Journal of Neuro-Oncology*, vol. 103, pp. 317–324, 2011.

[95] "Magforce: The Nanomedicine Company." https://www.magforce.com. Accesed: 2022-01-25.

[96] R. J. Wydra, C. E. Oliver, K. W. Anderson, T. D. Dziubla, and J. Z. Hilt, "Accelerated generation of free radicals by iron oxide nanoparticles in the presence of an alternating magnetic field," *RSC Advances*, vol. 5, no. 24, pp. 18888–18893, 2015.

[97] P. de Andrade Mello, S. Bian, L. E. Baggio Savio, H. Zhang, J. Zhang, W. Junger, M. R. Wink, G. Lenz, A. Buffon, Y. Wu, and S. C. Robson, "Hyperthermia and associated changes in membrane fluidity potentiate P2X7 activation to promote tumor cell death," *Oncotarget*, vol. 8, no. 40, pp. 67254–67268, 2017.

[98] A. L. Oei, L. E. M. Vriend, J. Crezee, N. A. P. Franken, and P. M. Krawczyk, "Effects of hyperthermia on DNA repair pathways: one treatment to inhibit them all," *Radiation Oncology*, vol. 10, p. 165, 2015.

[99] R. Le Fèvre, M. Durand-Dubief, I. Chebbi, C. Mandawala, F. Lagroix, J. P. Valet, A. Idbaih, C. Adam, J. Y. Delattre, C. Schmitt, C. Maake, F. Guyot, and E. Alphandéry, "Enhanced antitumor efficacy of biocompatible magnetosomes for the magnetic hyperthermia treatment of glioblastoma," *Theranostics*, vol. 7, no. 18, pp. 4618–4631, 2017.

[100] C. Chen, P. Wang, H. Chen, X. Wang, M. N. Halgamuge, C. Chen, and T. Song, "Smart magnetotactic bacteria enable the inhibition of neuroblastoma under an alternating magnetic field," *ACS Applied Materials & Interfaces*, vol. 14, no. 12, pp. 14049–14058, 2022.

[101] E. Alphandéry, S. Faure, L. Raison, E. Duguet, P. A. Howse, and D. A. Bazylinski, "Heat production by bacterial magnetosomes exposed to an oscillating magnetic field," *The Journal of Physical Chemistry C*, vol. 115, no. 1, pp. 18–22, 2011.

[102] C. Blanco-Andujar, F. J. Teran, and D. Ortega, "Current outlook and perspectives on nanoparticle-mediated magnetic hyperthermia," in *Iron*

*oxide nanoparticles for biomedical applications: synthesis, functionalization and application* (M. Mahmoudi and S. Laurent, eds.), pp. 197–245, Elsevier, 2018.

[103] R. Hergt and S. Dutz, "Magnetic particle hyperthermia—biophysical limitations of a visionary tumour therapy," *Journal of Magnetism and Magnetic Materials*, vol. 311, pp. 187–192, 2007.

[104] K. Lee, S. Choi, C. Yang, H. C. Wu, and J. Yu, "Autofluorescence generation and elimination: a lesson from glutaraldehyde," *Chemical Communications*, vol. 49, no. 29, pp. 3028–3030, 2013.

[105] A. Van de Walle, J. E. Perez, A. Abou-Hassan, M. Hémadi, N. Luciani, and C. Wilhelm, "Magnetic nanoparticles in regenerative medicine: what of their fate and impact in stem cells?," *Materials Today Nano*, vol. 11, p. 100084, 2020.

[106] S. Ashraf, A. Taylor, J. Sharkey, M. Barrow, P. Murray, B. Wilm, H. Poptani, M. J. Rosseinsky, D. J. Adams, and R. Lévy, "*In vivo* fate of free and encapsulated iron oxide nanoparticles after injection of labelled stem cells," *Nanoscale Advances*, vol. 1, pp. 367–377, 2019.

[107] R. Mejías, L. Gutiérrez, G. Salas, S. Pérez-Yagüe, T. M. Zotes, F. J. Lázaro, M. P. Morales, and D. F. Barber, "Long term biotransformation and toxicity of dimercaptosuccinic acid-coated magnetic nanoparticles support their use in biomedical applications," *Journal of Controlled Release*, vol. 171, no. 2, pp. 225–233, 2013.

[108] M. Levy, N. Luciani, D. Alloyeau, D. Elgrabli, V. Deveaux, C. Pechoux, S. Chat, G. Wang, N. Vats, F. Gendron, C. Factor, S. Lotersztajn, A. Luciani, C. Wilhelm, and F. Gazeau, "Long term *in vivo* biotransformation of iron oxide nanoparticles," *Biomaterials*, vol. 32, no. 16, pp. 3988–3999, 2011.

[109] A. S. Arbab, L. B. Wilson, P. Ashari, E. K. Jordan, B. K. Lewis, and J. A. Frank, "A model of lysosomal metabolism of dextran coated superparamagnetic iron oxide (SPIO) nanoparticles: implications for cellular magnetic resonance imaging," *NMR in Biomedicine*, vol. 18, no. 6, pp. 383–389, 2005.

[110] Y. Portilla, V. Mulens-Arias, A. Paradela, A. Ramos-Fernández, S. Pérez-Yagüe, M. P. Morales, and D. F. Barber, "The surface coating of iron oxide nanoparticles drives their intracellular trafficking and degradation in endolysosomes differently depending on the cell type," *Biomaterials*, vol. 281, p. 121365, 2022.

[111] J. M. Rojas, H. Gavilán, V. del Dedo, E. Lorente-Sorolla, L. Sanz-Ortega, G. B. da Silva, R. Costo, S. Perez-Yagüe, M. Talelli, M. Marciello, M. P. Morales, D. F. Barber, and L. Gutiérrez, "Time-course assessment of the aggregation and metabolization of magnetic nanoparticles," *Acta Biomaterialia*, vol. 58, pp. 181–195, 2017.

[112] F. Mazuel, A. Espinosa, N. Luciani, M. Reffay, R. Le Borgne, L. Motte, K. Desboeufs, A. Michel, T. Pellegrino, Y. Lalatonne, and C. Wilhelm, "Massive intracellular biodegradation of iron oxide nanoparticles evidenced magnetically at single-endosome and tissue levels," *ACS Nano*, vol. 10, no. 8, pp. 7627–7638, 2016.

[113] E. C. Theil, "Ferritin: the protein nanocage and iron biomineral in health and in disease," *Inorganic Chemistry*, vol. 52, no. 21, pp. 12223–12233, 2013.

[114] P. Arosio, R. Ingrassia, and P. Cavadini, "Ferritins: a family of molecules for iron storage, antioxidation and more," *Biochimica et Biophysica Acta - General Subjects*, vol. 1790, no. 7, pp. 589–599, 2009.

[115] G. Mesquita, T. Silva, A. C. Gomes, P. F. Oliveira, M. G. Alves, R. Fernandes, A. A. Almeida, A. C. Moreira, and M. S. Gomes, "H-Ferritin is essential for macrophages' capacity to store or detoxify exogenously added iron," *Scientific Reports*, vol. 10, p. 3061, 2020.

[116] M. P. Soares and I. Hamza, "Macrophages and iron metabolism," *Immunity*, vol. 44, no. 3, pp. 492–504, 2016.

[117] A. Curcio, A. Van De Walle, A. Serrano, S. Prévéral, C. Péchoux, D. Pignol, N. Menguy, C. T. Lefèvre, A. Espinosa, and C. Wilhelm, "Transformation cycle of magnetosomes in human stem cells: from degradation to biosynthesis of magnetic nanoparticles anew," *ACS Nano*, vol. 14, no. 2, pp. 1406–1417, 2020.

[118] A. Van de Walle, A. P. Plan Sangnier, A. Abou-Hassan, A. Curcio, M. Hémadi, N. Menguy, Y. Lalatonne, N. Luciani, and C. Wilhelm,

"Biosynthesis of magnetic nanoparticles from nanodegradation products revealed in human stem cells," *Proceedings of the National Academy of Sciences of the United States of America*, vol. 116, no. 10, pp. 4044–4053, 2019.

[119] M. L. Fdez-Gubieda, A. García-Prieto, J. Alonso, and C. Meneghini, "X-ray absorption fine structure spectroscopy in Fe oxides and oxyhydroxides," in *Iron Oxides: From Nature to Applications* (D. Faivre, ed.), pp. 397–422, John Wiley & Sons, Ltd, 2016.

[120] N. Feliu, D. Docter, M. Heine, P. Del Pino, S. Ashraf, J. Kolosnjaj-Tabi, P. Macchiarini, P. Nielsen, D. Alloyeau, F. Gazeau, R. H. Stauber, and W. J. Parak, "*In vivo* degeneration and the fate of inorganic nanoparticles," *Chemical Society Reviews*, vol. 45, no. 9, pp. 2440–2457, 2016.

[121] T. Kurz, A. Terman, B. Gustafsson, and U. T. Brunk, "Lysosomes in iron metabolism, ageing and apoptosis," *Histochemistry and Cell Biology*, vol. 129, no. 4, pp. 389–406, 2008.

[122] B. Garner, K. Roberg, and U. T. Brunk, "Endogenous ferritin protects cells with iron-laden lysosomes against oxidative stress," *Free Radical Research*, vol. 29, no. 2, pp. 103–114, 1998.

[123] T. Ganz, "Macrophages and systemic iron homeostasis," *Journal of Innate Immunity*, vol. 4, no. 5-6, pp. 446–453, 2012.

[124] J. F. Collingwood and N. D. Telling, "Iron oxides in the human brain," in *Iron Oxides: From Nature to Applications* (D. Faivre, ed.), pp. 143–176, John Wiley & Sons, Ltd, 2016.

[125] C. Quintana and L. Gutiérrez, "Could a dysfunction of ferritin be a determinant factor in the aetiology of some neurodegenerative diseases?," *Biochimica et Biophysica Acta - General Subjects*, vol. 1800, no. 8, pp. 770–782, 2010.

[126] P. Aisen, C. Enns, and M. Wessling-Resnick, "Chemistry and biology of eukaryotic iron metabolism," *The International Journal of Biochemistry & Cell Biology*, vol. 33, no. 10, pp. 940–959, 2001.

[127] A. García-Prieto, J. Alonso, D. Muñoz, L. Marcano, A. Abad Díaz de Cerio, R. Fernández de Luis, I. Orue, O. Mathon, A. Muela, and M. L. Fdez-Gubieda, "On the mineral core of ferritin-like proteins: structural

and magnetic characterization," *Nanoscale*, vol. 8, no. 2, pp. 1088–1099, 2016.

[128] P. C. Trivedi, J. J. Bartlett, and T. Pulinilkunnil, "Lysosomal biology and function: modern view of cellular debris bin," *Cells*, vol. 9, no. 5, p. 1131, 2020.

[129] S. Staniland, W. Williams, N. Telling, G. Van Der Laan, A. Harrison, and B. Ward, "Controlled cobalt doping of magnetosomes *in vivo*," *Nature Nanotechnology*, vol. 3, pp. 158–162, 2008.

[130] J. Li, N. Menguy, M. A. Arrio, P. Sainctavit, A. Juhin, Y. Wang, H. Chen, O. Bunau, E. Otero, P. Ohresser, and Y. Pan, "Controlled cobalt doping in the spinel structure of magnetosome magnetite: new evidences from element- and site-specific X-ray magnetic circular dichroism analyses," *Journal of The Royal Society Interface*, vol. 13, no. 121, p. 20160355, 2016.

[131] T. Prozorov, T. Perez-Gonzalez, C. Valverde-Tercedor, C. Jimenez-Lopez, A. Yebra-Rodriguez, A. Körnig, D. Faivre, S. K. Mallapragada, P. A. Howse, D. A. Bazylinski, and R. Prozorov, "Manganese incorporation into the magnetosome magnetite: magnetic signature of doping," *European Journal of Mineralogy*, vol. 26, no. 4, pp. 457–471, 2014.

[132] M. Tanaka, R. Brown, N. Hondow, A. Arakaki, T. Matsunaga, and S. Staniland, "Highest levels of Cu, Mn and Co doped into nanomagnetic magnetosomes through optimized biomineralisation," *Journal of Materials Chemistry*, vol. 22, no. 24, pp. 11919–11921, 2012.

[133] E. Alphandéry, C. Carvallo, N. Menguy, and I. Chebbi, "Chains of cobalt doped magnetosomes extracted from AMB-1 magnetotactic bacteria for application in alternative magnetic field cancer therapy," *Journal of Physical Chemistry C*, vol. 115, no. 24, pp. 11920–11924, 2011.

[134] C. N. Keim, U. Lins, and M. Farina, "Manganese in biogenic magnetite crystals from magnetotactic bacteria," *FEMS Microbiology Letters*, vol. 292, no. 2, pp. 250–253, 2009.

[135] R. M. Kershi, F. M. Ali, and M. A. Sayed, "Influence of rare earth ion substitutions on the structural, optical, transport, dielectric, and magnetic properties of superparamagnetic iron oxide nanoparticles," *Journal of Advanced Ceramics*, vol. 7, no. 3, pp. 218–228, 2018.

[136] G. Wang, Q. Peng, and Y. Li, "Lanthanide-doped nanocrystals: synthesis, optical-magnetic properties, and applications," *Accounts of Chemical Research*, vol. 44, no. 5, pp. 322–332, 2011.

[137] K. P. Rice, S. E. Russek, R. H. Geiss, J. M. Shaw, R. J. Usselman, E. R. Evarts, T. J. Silva, H. T. Nembach, E. Arenholz, and Y. U. Idzerda, "Temperature-dependent structure of Tb-doped magnetite nanoparticles," *Applied Physics Letters*, vol. 106, no. 6, p. 062409, 2015.

[138] B. Song, Q. Liu, H. Ma, Z. Tang, C. Liu, J. Zou, M. Tan, and J. Yuan, "Tumor-targetable magnetoluminescent silica nanoparticles for bimodal time-gated luminescence/magnetic resonance imaging of cancer cells *in vitro* and *in vivo*," *Talanta*, vol. 220, p. 121378, 2020.

[139] A. Rękorajska, G. Cichowicz, M. K. Cyranski, M. Pękała, and P. Krysinski, "Synthesis and characterization of $Gd^{3+}$- and $Tb^{3+}$-doped iron oxide nanoparticles for possible endoradiotherapy and hyperthermia," *Journal of Magnetism and Magnetic Materials*, vol. 479, pp. 50–58, 2019.

[140] G. Zhang, R. Du, L. Zhang, D. Cai, X. Sun, Y. Zhou, J. Zhou, J. Qian, K. Zhong, K. Zheng, D. Kaigler, W. Liu, X. Zhang, D. Zou, and Z. Wu, "Gadolinium-doped iron oxide nanoprobe as multifunctional bioimaging agent and drug delivery system," *Advanced Functional Materials*, vol. 25, no. 38, pp. 6101–6111, 2015.

[141] R. Aragón, D. J. Buttrey, J. P. Shepherd, and J. M. Honig, "Influence of nonstoichiometry on the Verwey transition," *Physical Review B*, vol. 31, no. 1, pp. 430–436, 1985.

[142] J. P. Shepherd, R. Aragón, J. W. Koenitzer, and J. M. Honig, "Changes in the nature of the Verwey transition in nonstoichiometric magnetite ($Fe_3O_4$)," *Physical Review B*, vol. 32, no. 3, pp. 1818–1819, 1985.

[143] J. P. Shepherd, J. W. Koenitzer, R. Aragón, J. Spałek, and J. M. Honig, "Heat capacity and entropy of nonstoichiometric magnetite $Fe_{3(1-\delta)}O_4$: the thermodynamic nature of the Verwey transition," *Physical Review B*, vol. 43, no. 10, pp. 8461–8471, 1991.

[144] F. Walz, "The Verwey transition - a topical review," *Journal of Physics: Condensed Matter*, vol. 14, no. 12, pp. R285–R340, 2002.

[145] R. Prozorov, T. Prozorov, S. K. Mallapragada, B. Narasimhan, T. J. Williams, and D. A. Bazylinski, "Magnetic irreversibility and the Verwey transition in nanocrystalline bacterial magnetite," *Physical Review B*, vol. 76, no. 5, p. 054406, 2007.

[146] E. M. Jefremovas, L. Gandarias, L. Marcano, A. Gacía-Prieto, I. Orue, A. Muela, M. L. Fdez-Gubieda, L. Fernández Barquín, and J. Alonso, "Modifying the magnetic response of magnetotactic bacteria: incorporation of Gd and Tb ions into the magnetosome structure," *Nanoscale Advances*, 2022. In press. DOI: 10.1039/D2NA00094F.

[147] H. G. Brittain, F. S. Richardson, and R. B. Martin, "Terbium(III) emission as a probe of calcium(II) binding sites in proteins," *Journal of the American Chemical Society*, vol. 98, no. 25, pp. 8255–8260, 1976.

[148] M. H. Simonian and J. A. Smith, "Spectrophotometric and colorimetric determination of protein concentration," *Current Protocols in Molecular Biology*, vol. 76, pp. 10.1.1–10.1A.9, 2006.

[149] U. Cho and J. K. Chen, "Lanthanide-based optical probes of biological systems," *Cell Chemical Biology*, vol. 27, no. 8, pp. 921–936, 2020.

[150] T. Matsunaga, T. Sakaguchi, and F. Tadakoro, "Magnetite formation by a magnetic bacterium capable of growing aerobically," *Applied Microbiology and Biotechnology*, vol. 35, pp. 651–655, 1991.

[151] D. A. Bazylinski, R. B. Frankel, and H. W. Jannasch, "Anaerobic magnetite production by a marine, magnetotactic bacterium," *Nature*, vol. 334, pp. 518–519, 1988.

[152] K. T. Silva, P. E. Leão, F. Abreu, J. A. López, M. L. Gutarra, M. Farina, D. A. Bazylinski, D. M. G. Freire, and U. Lins, "Optimization of magnetosome production and growth by the magnetotactic vibrio *Magnetovibrio blakemorei* strain MV-1 through a statistics-based experimental design," *Applied and Environmental Microbiology*, vol. 79, no. 8, pp. 2823–2827, 2013.

[153] D. A. Bazylinski, T. J. Williams, C. T. Lefèvre, D. Trubitsyn, J. Fang, T. J. Beveridge, B. M. Moskowitz, B. Ward, S. Schübbe, B. L. Dubbels, and B. Simpson, "*Magnetovibrio blakemorei* gen. nov., sp. nov., a magnetotactic bacterium (*Alphaproteobacteria: Rhodospirillaceae*) isolated

from a salt marsh," *International Journal of Systematic and Evolutionary Microbiology*, vol. 63, no. Pt 5, pp. 1824–1833, 2013.

[154] K. L. Thomas-Keprta, S. J. Clemett, D. A. Bazylinski, J. L. Kirschvink, D. S. McKay, S. J. Wentworth, H. Vali, E. K. Gibson, and C. S. Romanek, "Magnetofossils from ancient Mars: a robust biosignature in the martian meteorite ALH84001," *Applied and Environmental Microbiology*, vol. 68, no. 8, pp. 3663–3672, 2002.

[155] D. Gandia Aguado, *Magnetotactic bacteria: sources of model magnetic nanoparticles and biorobots for localized therapies*. PhD thesis, Universidad del País Vasco (UPV/EHU), 2022.

[156] F. C. Meldrum, S. Mann, B. R. Heywood, R. B. Frankel, and D. A. Bazylinski, "Electron microscopy study of magnetosomes in a cultured coccoid magnetotactic bacterium," *Proceedings of the Royal Society of London B*, vol. 251, no. 1332, pp. 231–236, 1993.

[157] D. A. Bazylinski, T. J. Williams, C. T. Lefèvre, R. J. Berg, C. L. Zhang, S. S. Bowser, A. J. Dean, and T. J. Beveridge, "*Magnetococcus marinus* gen. nov., sp. nov., a marine, magnetotactic bacterium that represents a novel lineage (*Magnetococcaceae* fam. nov., *Magnetococcales* ord. nov.) at the base of the *Alphaproteobacteria*," *International Journal of Systematic and Evolutionary Microbiology*, vol. 63, no. Pt 3, pp. 801–808, 2013.

[158] H. Nudelman, C. Valverde-Tercedor, S. Kolusheva, T. Perez Gonzalez, M. Widdrat, N. Grimberg, H. Levi, O. Nelkenbaum, G. Davidov, D. Faivre, C. Jimenez-Lopez, and R. Zarivach, "Structure–function studies of the magnetite-biomineralizing magnetosome-associated protein MamC," *Journal of Structural Biology*, vol. 194, no. 3, pp. 244–252, 2016.

[159] C. Valverde-Tercedor, F. Abadía-Molina, M. Martinez-Bueno, E. Pineda-Molina, L. Chen, Z. Oestreicher, B. H. Lower, S. K. Lower, D. A. Bazylinski, and C. Jimenez-Lopez, "Subcellular localization of the magnetosome protein MamC in the marine magnetotactic bacterium *Magnetococcus marinus* strain MC-1 using immunoelectron microscopy," *Archives of Microbiology*, vol. 196, pp. 481–488, 2014.

[160] F. Abreu, M. E. Cantão, M. F. Nicolás, F. G. Barcellos, V. Morillo, L. G. Almeida, F. F. do Nascimento, C. T. Lefèvre, D. A. Bazylinski,

A. T. R. de Vasconcelos, and U. Lins, "Common ancestry of iron oxide- and iron-sulfide-based biomineralization in magnetotactic bacteria," *The ISME Journal*, vol. 5, no. 10, pp. 1634–1640, 2011.

[161] T. Nagai, K. Ibata, E. S. Park, M. Kubota, K. Mikoshiba, and A. Miyawaki, "A variant of yellow fluorescent protein with fast and efficient maturation for cell-biological applications," *Nature Biotechnology*, vol. 20, no. 1, pp. 87–90, 2002.

[162] R. Liu, J. Liu, J. Tong, T. Tang, W. C. Kong, X. Wang, Y. Li, and J. Tang, "Heating effect and biocompatibility of bacterial magnetosomes as potential materials used in magnetic fluid hyperthermia," *Progress in Natural Science: Materials International*, vol. 22, no. 1, pp. 31–39, 2012.

[163] N. Ginet, R. Pardoux, G. Adryanczyk, D. Garcia, C. Brutesco, and D. Pignol, "Single-step production of a recyclable nanobiocatalyst for organophosphate pesticides biodegradation using functionalized bacterial magnetosomes," *PLoS One*, vol. 6, no. 6, p. e21442, 2011.

[164] S. Ohuchi and D. Schüler, "*In vivo* display of a multisubunit enzyme complex on biogenic magnetic nanoparticles," *Applied and Environmental Microbiology*, vol. 75, no. 24, pp. 7734–7738, 2009.

[165] F. Mickoleit, C. B. Borkner, M. Toro-Nahuelpan, H. M. Herold, D. S. Maier, J. M. Plitzko, T. Scheibel, and D. Schüler, "*In vivo* coating of bacterial magnetic nanoparticles by magnetosome expression of spider silk-inspired peptides," *Biomacromolecules*, vol. 19, no. 3, pp. 962–972, 2018.

[166] S. Borg, F. Popp, J. Hofmann, H. Leonhardt, U. Rothbauer, and D. Schüler, "An intracellular nanotrap redirects proteins and organelles in live bacteria," *mBio*, vol. 6, no. 1, pp. e02117–14, 2015.

[167] L. Marcano, I. Orue, D. Gandia, L. Gandarias, M. Weigand, R. M. Abrudan, A. García-Prieto, A. García-Arribas, A. Muela, M. L. Fdez-Gubieda, and S. Valencia, "Magnetic anisotropy of individual nanomagnets embedded in biological systems determined by axi-asymmetric X-ray transmission microscopy," *ACS Nano*, vol. 16, no. 5, pp. 7398–7408, 2022.

[168] Z. Nemati, J. Alonso, L. M. Martinez, H. Khurshid, E. Garaio, J. Á. García, M. H. Phan, and H. Srikanth, "Enhanced magnetic hyperthermia

in iron oxide nano-octopods: size and anisotropy effects," *Journal of Physical Chemistry C*, vol. 120, no. 15, pp. 8370–8379, 2016.

[169] J. Carrey, B. Mehdaoui, and M. Respaud, "Simple models for dynamic hysteresis loop calculations of magnetic single-domain nanoparticles: application to magnetic hyperthermia optimization," *Journal of Applied Physics*, vol. 109, no. 8, p. 083921, 2011.

[170] S. Martel, M. Mohammadi, O. Felfoul, Z. Lu, and P. Pouponneau, "Flagellated magnetotactic bacteria as controlled MRI-trackable propulsion and steering systems for medical nanorobots operating in the human microvasculature," *The International Journal of Robotics Research*, vol. 28, no. 4, pp. 571–582, 2009.

[171] U. Heyen and D. Schüler, "Growth and magnetosome formation by microaerophilic *Magnetospirillum* strains in an oxygen-controlled fermentor," *Applied Microbiology and Biotechnology*, vol. 61, no. 5-6, pp. 536–544, 2003.

[172] R. P. Blakemore, D. Maratea, and R. S. Wolfe, "Isolation and pure culture of a freshwater magnetic spirillum in chemically defined medium," *Journal of Bacteriology*, vol. 140, no. 2, pp. 720–729, 1979.

[173] B. Ravel and M. Newville, "ATHENA, ARTEMIS, HEPHAESTUS: data analysis for X-ray absorption spectroscopy using IFEFFIT," *Journal of Synchrotron Radiation*, vol. 12, no. Pt 4, pp. 537–541, 2005.

[174] M. Newville, "IFEFFIT: interactive XAFS analysis and FEFF fitting," *Journal of Synchrotron Radiation*, vol. 8, no. Pt 2, pp. 322–324, 2001.

# List of Publications

Several scientific papers have been published during the period of this thesis:

1. D. Gandia*, L. Gandarias*, I. Rodrigo, J. Robles-García, R. Das, E. Garaio, J.A. García, M.H. Phan, H. Srikanth, I. Orue, J. Alonso, A. Muela, M.L. Fdez-Gubieda, "Unlocking the potential of magnetotactic bacteria as magnetic hyperthermia agents," *Small*, vol. 15, no. 41, pp. 1902626, 2019. *Co-first authors.

2. D. Gandia, L. Gandarias, L. Marcano, I. Orue, D. Gil-Cartón, J. Alonso, A. García-Arribas, A. Muela, M.L. Fdez-Gubieda, "Elucidating the role of shape anisotropy in faceted magnetic nanoparticles using biogenic magnetosomes as a model," *Nanoscale*, vol. 12, no. 30, pp. 16081–16090, 2020.

3. E.M. Jefremovas, L. Gandarias, I. Rodrigo, L. Marcano, C. Grütner, J.A. García, E. Garayo, I. Orue, A. García-Prieto, A. Muela, M.L. Fernández-Gubieda, J. Alonso, L. Fernández Barquín, "Nanoflowers versus magnetosomes: comparison between two promising candidates for magnetic hyperthermia therapy," *IEEE Access*, vol. 9, pp. 99552-99561, 2021.

4. E.M. Jefremovas, L. Gandarias, L. Marcano, A. García-Prieto, I. Orue, A. Muela, M.L. Fdez-Gubieda, L. Fernández Barquín, J. Alonso, "Modifying the magnetic response of magnetotactic bacteria: incorporation of Gd and Tb ions into the magnetosome structure," *Nanoscale Advances*, 2022. In press (DOI: 10.1039/d2na00094f)

5. L. Marcano, I. Orue, D. Gandia, L. Gandarias, M. Weigand, R. Marius Abrudan, A. García-Prieto, A. García-Arribas, A. Muela, M.L. Fdez-Gubieda, S. Valencia, "Magnetic anisotropy of individual nanomagnets

embedded in biological systems determined by axi-asymmetric X-ray transmission microscopy," *ACS Nano*, vol. 16, no. 5, pp. 7398-7408, 2022.

Other publications have derived from this thesis and are under preparation to be published:

1. L. Gandarias, L. Arana, A. García Prieto, I. Alkorta, M.L. Fdez-Gubieda, A. Muela, "Interaction of magnetotactic bacteria and magnetosomes with cancer cells: elucidating the endocytic pathways".

2. L. Gandarias, A. Gascón Gubieda, D. Gandia, L. Marcano, A. Abad, L. Olivi, G. Aquilanti, T. Buslaps, O. Mathon, G. Gorni, M.L. Fdez-Gubieda, A. Muela, A. García Prieto, "Long-term tracking of magnetosomes in eukaryotic cells".

3. L. Gandarias, E.M. Jefremovas, D.Y. Villanueva Alvaro, L. Marcano, I. Orue, V. Martinez, P. Ramos-Cabrer, S. Valencia, G. Gorni, L. Fernández Barquín, A. García Prieto, A. Muela, M.L. Fdez-Gubieda, J. Alonso, "Multifunctional magnetotactic bacteria obtained by the incorporation of terbium and gadolinium".

# List of Figures

# List of Tables